The Structure and Evolution of Massive Star and Cluster Forming Regions

by

Cara Battersby

B.S., University of Massachusetts, Amherst 2006

M.A., Boston University, 2008

A thesis submitted to the

Faculty of the Graduate School of the

University of Colorado in partial fulfillment

of the requirements for the degree of

Doctor of Philosophy

Department of Astrophysical & Planetary Sciences

2013

This thesis entitled:
The Structure and Evolution of Massive Star and Cluster Forming Regions
written by Cara Battersby
has been approved for the Department of Astrophysical & Planetary Sciences

Prof. John Bally

Prof. Jeremy Darling

Prof. Neal J. Evans II

Prof. James M. Jackson

Prof. J. Michael Shull

Date

The final copy of this thesis has been examined by the signatories, and we find that both the content and the form meet acceptable presentation standards of scholarly work in the above mentioned discipline.

Battersby, Cara (Ph.D., Astrophysics)

The Structure and Evolution of Massive Star and Cluster Forming Regions

Thesis directed by Prof. John Bally

The formation of massive stars and stellar clusters is important in understanding the light we receive from other galaxies, the life cycle of matter in the Galaxy, and the global process of star formation. However, this problem has remained elusive as the relative rarity, large distances, confusion, and obscured nature of massive star forming regions has made a global and high-resolution understanding of their formation intractable for decades. The advent of large Galactic Plane Surveys and high-resolution observing facilities have allowed us to make large strides in this field by constraining the physical properties at the onset of massive star formation in clustered environments, identifying the stages of massive star formation, and estimating the lifetimes of these phases.

We present a detailed analysis of two young massive star forming regions in different evolutionary stages embedded within a single Infrared Dark Cloud using NH_3 on the Karl G. Jansky Very Large Array. In this analysis, we characterize the physical structure (column density, temperature, and virial parameter) just prior to the onset of massive star formation and infer evolution in this structure by measuring it at different evolutionary stages. We expand this analysis to a global scale using Herschel and Spitzer surveys of the Galactic Plane from mid-to far-IR, devising a method to identify precursors to stellar clusters throughout the Galaxy for the first time. By separating the diffuse Galactic cirrus emission from the dense molecular clumps, we derive the dust temperatures and column densities characteristic of cluster-forming clumps. We compare these physical properties with star formation tracers in a systematic way to distinguish and characterize their evolutionary phases. We compare the physical properties derived from gas with those derived using dust. We estimate lifetimes for these evolutionary phases and speculate on the large-scale dynamics in the formation of stellar clusters.

We constrain the conditions at the onset of massive star formation, measure how these conditions change with evolutionary phase, and estimate the duration of each phase. This thesis places global and high-resolution constraints on the physical properties, evolution, and lifetimes of massive star and cluster forming regions.

Dedication

To all the atoms of Oxygen, Carbon, Hydrogen,

and Nitrogen[1] *, who, in their various arrangements and manifestations,*

have inspired and encouraged me, guided and aided me,

taught and supported me.

From the molecules of carbon monoxide

and ammonia in interstellar space

lending insights through their lines

to the teachers, friends, family, and colleagues

who have helped

in No. Small. Way.

to complete this thesis,

I thank you.

For these moments, in which our atoms have shared

time and space, words and ideas, laughter and learning,

I am ever grateful and ever humbled.

Thank you.

[1] the top four elements that compose a human body by mass, which I learned on Wikipedia. In grad school I learned that most things can be found on Wikipedia... except for your research, which of course is up to you to figure out, but may someday be on Wikipedia too if you do a good enough job.

Firstly, a giant thank you to my advisor, Prof. John Bally, for his limitless enthusiasm, encouragement, and support and for countless fruitful and interesting scientific discussions. John, you have always treated me as an equal, and through that you have helped me to grow into the independent, creative, and thoughtful scientist that I am today. Thank you for always believing in me, for always supporting me, and for always listening to my crazy ideas. It has been a pleasure working with you. I really admire you and hope we can continue to work together.

I would also like to thank my thesis committee, Prof. Jeremy Darling, Prof. Neal Evans, Prof. Jim Jackson, and Prof. Mike Shull. Other than the obvious task of reading this 150 page document, you all have contributed to my graduate career in a positive and inspiring way. *Jeremy*, thank you for your patience, support, inspiration, and guidance. Thank you for sharing your perspective with me so many times and helping me to understand where I was at and where I want to be. I do not think you will ever really know how meaningful our little talks have been for me. I hope that we can continue to work together on projects, perhaps soon it will be time to dust off one of those 'crazy ideas' we have discussed. *Neal*, I want to thank you for your support and encouragement, especially in this last year of my graduate career. Working with you on our NSF proposal was an immensely gratifying process, and I cannot tell you quite how much I appreciate your kindly agreeing to write recommendation letters for me. I really respect your vision of our field and truly hope that we will get the opportunity to work together more closely in the future. *Jim*, I have you to thank for the ideas and perspectives that have helped to guide most of this work. It is you who got me working in this field in the first place and you that I have to thank for holding my hand through my first two challenging years of research and inspiring me through thought-provoking discussions, interesting ideas, and, let's be honest, pretty pictures! Thank you and I hope we can continue to work together in the future. And finally, *Mike* who has always treated me as an equal and had faith in me (sometimes more faith than I had in myself!). You have taught me so much, and not just in your classes or on my Comps II committee but through your guiding words about the field, the politics, and the people of astronomy. Thank you for always believing in me, for taking me under your wing, for helping to provide opportunities for me, and for rooting for my success. *Thank you*

all.

In addition, I owe a great thanks to my many colleagues, especially Adam Ginsburg. Adam and I fought through graduate school together, and I am glad to say that I think we won. Adam was absolutely instrumental in so many ways for my learning the ins and outs of research. We learned a lot from each other. Our discussions, arguments, and resolutions about topics in the star forming field helped me to work out so many questions and helped to build my perspective on the big picture of star formation. Thank you. I hope we will always be colleagues.

Of course, there are countless others in my personal and professional life to thank. My friends who studied with me, worked hard with me, and helped me to get out and play too. My friends who have supported me through this time, cooked with me, hiked with me, listened to me gripe over drinks, and just generally had fun with me and helped to make my world complete. My friends who have shown me kindness, wisdom, acceptance and love. My frisbee team for providing fun and adventure outside of Duane and many fond memories. I thank my family for their endless kindness, wisdom, and understanding. For embracing my career choice with me, always finding ways to show their love across a thousand miles (thanks for all the beautiful cards, mom!), and for never flinching in their support and belief in me. You all know who you are. I love you and thank you.

Oh, and of course, where would I be without the amazing office staff in APS and CASA! From getting me signed up for classes this semester last minute so I can actually graduate (whoops!) to answering the thousand questions and helping with the thousand tasks I have been stuck on over the years. Thank you!

Contents

Chapter

Chapter 1

Introduction

1.1 Overview

Massive stars have shaped the universe around us throughout cosmic time. Since their reionization of the universe after the Cosmic Dark Ages, massive stars have molded their galactic environment and shaped the life cycle of gas and stars around them. The formation mechanism of massive stars and stellar clusters remains a long-standing problem in astrophysics, whose implications are wide ranging. Understanding where and how stellar clusters form impacts our understanding of the global process of star formation, the origin of the Initial Mass Function (IMF), processes in the Interstellar Medium (ISM), and star formation rates in nearby galaxies. Massive stars and stellar clusters dominate galactic ecology, through their immense radiation, powerful winds and outflows, and the injection of energy, turbulence, and metals in their explosive stellar death. An understanding of this process is a cornerstone in modern astrophysics.

The predominant (and perhaps only) mode of massive star formation is in clusters (Lada & Lada, 2003; de Wit et al., 2005), and a definitive understanding of star cluster formation has been a long-sought goal in astrophysics. A global picture of star formation must include the process that turns Giant Molecular Clouds (GMCs) into young stellar clusters and associations. Fundamental questions concerning the formation mechanism, environment, and early evolution of stellar clusters have remained unanswered due to the inherent complexity of the problem. Forming star clusters are embedded (A_V ~10-100), short-lived, and often distant ($\sim$ 5 kpc). The problem is hierarchical, and by its very nature spans many physical scales, from parsec-scale molecular clumps spread

throughout the Galaxy, down to cores on <0.1 pc scales.

In this thesis, we seek to overcome these challenges by combining Galactic-scale observations with targeted high-resolution observations to form a cohesive picture of the structure and evolution of massive star and cluster-forming regions. We measure the column density and temperature structure in a massive star-forming cloud at high-resolution ($\sim$ 0.1 pc) and compare with the literature to uncover common conditions at the onset of massive star formation. Observing a variety of evolutionary phases allows us to measure how the column density and temperature structure changes with time. We utilize large-scale Galactic Plane surveys to measure the global properties of massive star and cluster forming regions and compare these with star formation tracers in a systematic way to characterize the precursors to stellar clusters and their evolutionary stages. Using the relative fractions in each evolutionary stage, we estimate relative lifetimes for the evolutionary phases of massive star and cluster forming regions. With this thesis, we constrain the conditions at the onset of massive star formation, present an evolutionary sequence for massive star-forming regions, and estimate the duration of each of these phases.

1.2 Introduction

The formation of low-mass stars has been explored in detail in nearby low-mass star-forming regions and is understood to proceed through some well-constrained phases (Shu et al., 1987). Cores condense within molecular clouds and lose magnetic and turbulent support through ambipolar diffusion. A protostar forms in the center of the collapsing core, which is surrounded by a nebular accretion disk. The angular momentum loss in this disk is counteracted by the formation of bipolar outflows emanating from the protostar poles. As the protostar turns on, heats up, and evaporates the remaining core envelope, the system reveals a newly formed star surrounded by a circumstellar disk.

While the paradigm of low-mass star formation is generally accepted, the formation mechanism of massive stars remains a topic of debate. A simplistic, spherically symmetric, scaled-up massive core cannot collapse to form a massive star ($M > 8\ M_{\odot}$) akin to low-mass star formation,

as the energy released through gravitational contraction quickly exceeds the Eddington luminosity and prevents further collapse (e.g. Shu et al., 1987). Krumholz et al. (2009) suggested that this problem can be circumvented by allowing material to flow onto the massive core through dense filaments, while energy escapes in radiatively driven bubbles.

While some argue that the formation of massive stars may be a scaled-up version of low mass star formation, with a hydrostatic massive core supported by turbulent pressure (the turbulent core accretion model; McKee & Tan, 2003; McLaughlin & Pudritz, 1996), others argue that the formation mechanism of stars in clusters is a unique and competitive process (competitive accretion; Bonnell et al., 2001; Wang et al., 2010). The turbulent core accretion model of McKee & Tan (2003) suggests that massive stars form from massive hydrostatic cores supported by the non-thermal pressure provided by turbulence and magnetic fields. This high level of non-thermal pressure support naturally arises in massive, gravitationally bound gas clumps[1] , many of which may form clusters of stars. The theory of competitive accretion, developed from the simulations of Bonnell et al. (2001), suggests instead that massive stars form from small sub-virial seeds which compete for material in a massive gas clump. Those seeds at advantageous locations within the clump will accrete more material, forming massive stars. While the turbulent core accretion model requires slow global collapse of the massive gas clump of the order several free-fall times (e.g. Tan et al., 2006), some suggest fast star formation in massive gas clumps, of the order of a free-fall time (e.g. Elmegreen, 2000, 2007; Hartmann & Burkert, 2007).

Differentiating between competing theories of massive star formation has been hampered by the inherent complexity of the problem. Star formation is hierarchical and spans many orders of magnitude in size scale ($<$ 0.1 pc scale cores enveloped within 1 pc scale clumps distributed on kpc scales throughout the Galaxy), density ($n_{clump} \sim 10^3$ cm^{-3} - $n_{core} \sim 10^7$ cm^{-3}), and mass ($\sim$10 M$_\odot$ cores to 10^4 M$_\odot$ clumps). Physical properties that span orders of magnitude complicate

[1] In this work, we use the terminology wherein clouds are roughly 10^3 - 10^4 M$_\odot$with sizes of 2-15 pc, clumps are roughly 10^2-10^3 M$_\odot$with sizes of 0.3-3 pc, and cores are roughly 1-100 M$_\odot$with sizes of about 0.03-0.2 pc as in Bergin & Tafalla (2007). We use the term 'core complexes' to refer to clumps that are resolved into their sub-structured cores.

simulations of massive star-forming regions, as do the many, varied physical properties important in their formation, including, but not limited to, stellar feedback, turbulence, gravity, radiative transfer, and magnetohydrodynamics. Observationally, the problem is complicated by the embedded nature and relative rarity of massive star-forming regions, necessitating large samples, high resolution long-wavelength observations toward distant, embedded sources. Through a combination of only forming a small fraction of massive stars in a standard initial mass function and the short lifetimes of massive stars, massive star-forming regions are relatively rare, meaning that they are further away on average and require high resolution facilities. The short-lived evolutionary phases also require large samples to determine an evolutionary sequence and timescale. Additionally, the earliest phases of massive star formation are highly embedded ($A_V \sim$ 10-100), necessitating long-wavelength observations of re-processed light from dust grains. Furthermore, once a massive star forms, it evolves rapidly, quickly heating, ionizing, and eventually destroying the natal environment from which it formed.

Much like their low-mass counterparts, massive stars are thought to form in cold, dense molecular clouds; however, these natal clumps are necessarily of higher mass if they are to form massive stars. The discovery of Infrared Dark Clouds (IRDCs) as dark extinction features against the bright mid-infrared Galactic background with the *Midcourse Space Experiment (MSX)* and the *Infrared Space Observatory* satellites (Egan et al., 1998; Perault et al., 1996; Omont et al., 2003) provided candidate massive star birthplaces. We will call these massive, dense gas clumps from which massive stars and clusters form Pre-Cluster Clumps (PCCs). By definition, IRDCs are cold and dense enough to obscure the Galactic mid-IR background at 8 μm, typically with temperatures T$<$ 25 K (Carey et al., 1998; Pillai et al., 2006) and densities $n_H > 10^4$ cm^{-3} (Egan et al., 1998; Carey et al., 1998; Rathborne et al., 2006). The most massive of these are about 10^3 - 10^4 $M_\odot$(Rathborne et al., 2006; Battersby et al., 2010) and are substructures within larger Giant Molecular Clouds (GMCs).

In the past decade, IRDCs have emerged as the most likely sites for the birthplaces of massive stars, as many have been shown to host the earliest phases of massive star formation (e.g. Rathborne

et al., 2006; Battersby et al., 2010; Ragan et al., 2006; Peretto & Fuller, 2009). While the most massive IRDCs are likely PCC (Pre-Cluster Clump) candidates, the majority of IRDCs (Simon et al., 2006; Peretto & Fuller, 2009; Kauffmann & Pillai, 2010; Wilcock et al., 2012) fall short of this threshold and are not capable of forming massive stars. Additionally, the identification of IRDCs suffers from a severe selection bias. Their identification against the bright mid-IR Galactic background precludes their identification in the outer Galaxy, at high Galactic latitudes, and on the far side of the Galaxy. IRDCs capable of forming massive stars (of which there are many) provide an excellent starting place for studies of massive star and cluster formation. Galactic-scale analyses of this process, however, will require another way to identify PCCs.

As the earliest phases of massive star and cluster formation occur in heavily embedded PCCs, it is necessary to observe at long-wavelengths to probe deep within the clump and measure the structure and properties of the star-forming cores. Recent long-wavelength surveys of the Galactic Plane allow us to peer into cluster-forming clumps across the Galaxy. Galactic Plane surveys in the sub-mm to far-IR, in particular, provide an optically thin tracer of the dust emission from these cold, dense clouds. These surveys include the Bolocam Galactic Plane Survey at 1.1 mm (BGPS Aguirre et al., 2011; Rosolowsky et al., 2010), the APEX Telescope Large Area Survey of the Galaxy at 870 μm (ATLASGAL Schuller et al., 2009), and the Herschel Infrared Galactic Plane Survey from 70 to 500 μm (Hi-GAL Molinari et al., 2010). These surveys have confirmed that the most massive IRDCs are, in fact, cold, dense gas clumps seen in dust emission in the sub-mm (Battersby et al., 2010; Parsons et al., 2009; Wilcock et al., 2012). These long-wavelength surveys allow us to identify PCCs throughout the Galaxy in a systematic way, independent of their location with respect to the mid-IR background.

Investigations toward clumps identified through these long-wavelength surveys have found a range of temperatures, average densities, and star-forming activity (e.g. Dunham et al., 2011a,b; Battersby et al., 2011; Wienen et al., 2012; Peretto et al., 2010). While many of these dense gas clumps are cold and pre-star-forming, others are actively star-forming and have begun to heat up their natal molecular clump. Even IRDCs, thought to host the earliest stages of massive star

formation, have been shown to exhibit a range of evolutionary states from pre- to actively star-forming (e.g. Chambers et al., 2009; Battersby et al., 2010).

In this thesis, we investigate the temperature and column density structure of massive star and cluster forming regions as a function of evolutionary state. We do this on a global scale using Galactic Plane surveys and at high-resolution with targeted observations. Using the global sample, we estimate the relative fraction of each of the evolutionary stages and estimate a lifetime for each phase. The relationship between IRDCs and long-wavelength identified dust clumps is also explored, and we present a method for identifying PCCs throughout the Galaxy. This thesis contributes to our understanding of the physical properties and early evolutionary stages of massive star and cluster formation. Additionally, we lay the groundwork for future studies with the methods and tools presented.

In Chapter 2, we present the high-resolution temperature and column density structure of two PCCs in different evolutionary stages embedded within a single massive star-forming IRDC. In Chapter 3, we expand this analysis to a global scale using Herschel and Spitzer surveys of the Galactic Plane, measure the temperature and column density structure of PCCs, and correlate these directly with star formation tracers. In doing so, we devise a method to identify PCCs in a systematic way throughout the Galaxy based on their physical properties. In Chapter 4 we summarize how we have derived physical properties from gas and dust emission and absorption measurements and compare their results. In Chapter 5 we estimate the relative fraction of starless and star-forming regions using our global analysis and derive lifetimes for these phases. We conclude this thesis in Chapter 6.

Chapter 2

The Evolution of Temperature and Density Structure in Infrared Dark Clouds

Massive stars illuminate and shape our view of the universe, yet an understanding of the conditions under which they form remains tenuous. A measurement of the physical structure at the onset of massive star formation and how this structure evolves is crucial for distinguishing between models of massive star formation. We compile new NH_3 (1,1), (2,2), and (4,4) observations from the Karl G. Jansky Very Large Array (VLA) with recent work in the literature to explore the range of conditions observed in young, massive star-forming regions. To disentangle the effects of evolution from those of distance/resolution, abundance, and large-scale environment, we compare clumps in different evolutionary stages embedded within a single Infrared Dark Cloud (IRDC), G32.02+0.06. We find that the early stages of clustered star formation are characterized by dense, parsec-scale filamentary structures interspersed with complexes of dense cores (<0.1 cores clustered in complexes separated by ∼1 pc). We find that the youngest core is the most extended while the more evolved cores are denser and more compact, showing very similar column density structure before and shortly after the onset of massive star formation, with peak surface densities just above $\Sigma = 1$ g cm^{-2}. Pre-star-forming cores and filaments show smooth temperature structure from 10-20 K, rising to over 40 K in star-forming cores.

2.1 Introduction

The light from massive stars ($M \geq 8$ $M_\odot$) and stellar clusters dominates our picture of the universe. Through their ionizing radiation, powerful winds and outflows, and explosive deaths,

they have molded their galactic environment and defined the life cycles of gas and stars around them. However, much remains to be understood concerning the formation processes of stars in a clustered environment. Are there required initial conditions for the onset of massive star formation in our Galaxy or can they form in a range of environments?

One first step to addressing these questions observationally is to identify locations where massive stars are forming. It is thought that most, if not all, massive stars form in clusters (Lada & Lada, 2003; de Wit et al., 2005). Infrared Dark Clouds (IRDCs) are a popular starting place, as their cold (< 20 K), high column density ($N(H_2) > 10^{22}$ cm^{-2}) and high-mass (10^2 - 10^4 M$_\odot$) nature are ideally suited for forming massive stars and stellar clusters (Carey et al., 2000; Rathborne et al., 2006; Battersby et al., 2010), however, the identification of an IRDC requires that it be located on the near-side of a bright mid-IR background. Galactic Plane Surveys (e.g., Bolocam Galactic Plane Survey - BGPS, APEX Telescope Large Area Survey of the GALaxy - ATLASGAL, and the Herschel Infrared Galactic Plane Survey - Hi-GAL, Aguirre et al., 2011; Schuller et al., 2009; Molinari et al., 2010) of dust continuum trace cold, optically thin dust throughout the Galaxy and corroborate the picture of massive stars and clusters forming in cold, high-density clouds. However, ammonia observations of BGPS and ATLASGAL clumps have shown that they sample a range of evolutionary stages, from pre- to actively star-forming (e.g., Dunham et al., 2011b; Wienen et al., 2012). These groups have worked to isolate starless clumps[1] (e.g., Tackenberg et al., 2012; Wilcock et al., 2011). Battersby et al. (2011) (Chapter 3) showed that physical properties derived from Hi-GAL can be used to identify the cold, dense precursors to massive stars and stellar clusters, pre-cluster clumps (PCCs), physically similar to IRDCs but that can be identified independent of their location with respect to the mid-IR background.

Ammonia has been shown to be a robust tracer of physical properties (particularly temperature) in star-forming regions (e.g. Ho & Townes, 1983; Mangum et al., 1992; Longmore et al.,

[1] In this work, we use the terminology wherein clouds are roughly 10^3 - 10^4 M$_\odot$with sizes of 2-15 pc, clumps are roughly 10^2-10^3 M$_\odot$with sizes of 0.3-3 pc, and cores are roughly 1-100 M$_\odot$with sizes of about 0.03-0.2 pc as in Bergin & Tafalla (2007). We use the term 'core complexes' to refer to clumps that are resolved into their sub-structured cores.

2007; Juvela et al., 2012; Pillai et al., 2006, 2011) and an excellent way to address the physical conditions associated with the onset of massive star formation. Due to the hierarchical clustered nature of star formation (e.g., Lada & Lada, 2003; Gouliermis et al., 2012), an understanding of the conditions of massive star formation requires both large-scale and high-resolution analyses of their physical properties. In Chapter 3, we measure the physical conditions (dust temperatures and column densities) of massive star forming regions on about 1 pc scales, and in this work we compare this global picture with high-resolution observations. Various high-resolution observations toward young clustered star-forming regions (e.g., Brogan et al., 2009; Fontani et al., 2012; Li et al., 2013; Rathborne et al., 2008) begin to reveal the nature of star-forming protoclusters, hot molecular cores, and chemical variation. High-resolution ammonia observations (e.g., Wang et al., 2008; Zhang & Wang, 2011; Liu et al., 2012; Devine et al., 2011) have revealed a strong correlation between the emission of NH_3 and dust emission and given some insight into the properties of young massive star forming regions. In this paper, we probe varying evolutionary states within a single massive star-forming region (G32.02+0.06) and compare the results of the gas properties with those derived from dust.

In this work, the first of a group of papers, we present high-resolution ($\sim$ 0.1 pc) Karl G. Jansky Very Large Array (VLA) observations of 3 para inversion transitions of NH_3 toward an IRDC with varying evolutionary states. We eliminate common observational biases by observing different evolutionary phases within a single IRDC. Therefore, the observed clumps share a common distance, cloud properties, and large-scale environment. We perform radiative transfer modeling on the NH_3 lines to produce maps of the temperature, column density, velocity, and velocity dispersion. We present these observations and compare with previous results to summarize our understanding of the structure of massive star forming regions and how they evolve. In Chapter 4, we compare the gas properties (temperatures and column densities) with those derived from dust and derive an abundance of NH_3 in this IRDC. In the following paper (Battersby et al., 2013), we review the large-scale environment of this IRDC, core and filament kinematics, and virial parameters to assess the gravitational stability of the cores.

In §2.2 we present the observations, data reduction, and source selection and in §2.3 discuss the radiative transfer model. In §2.4 we present the temperature and column density maps derived for this IRDC and identify a young HII region. In §2.5, we compare the structure we observe with previous observations to explore the range of properties observed in massive star-forming regions. We discuss fragmentation and evolutionary stages in §2.4.3 and §2.4.5. We summarize our conclusions in §2.6.

2.2 Data

2.2.1 Source Selection

We observed two clump locations within IRDC G32.02+0.06, an active clump ([ℓ, b] = [32.032^o, +0.059^o]) and a quiescent clump ([ℓ, b] = [31.947^o, +0.076^o]) at a distance of $\sim$ 5.5 kpc (see next paragraph). The two clumps are embedded within a filamentary IRDC which is part of a much larger Massive Molecular Filament (MMF; Battersby & Bally, 2012), G32.02+0.06, see Figure 2.1. The MMF is about 80 pc long (as measured in ^{13}CO with the Galactic Ring Survey, Jackson et al., 2006) in the Galactic mid-plane with a total mass of about 2×10^5 M$_\odot$. The velocity gradient across G32.02+0.06 is less than 4 km s^{-1}, and it appears to have been formed at the intersection of two UV-driven bubbles from previous generations of massive stars. The large-scale properties of this cloud and its environment will be discussed in more detail in the companion paper, Battersby et al. (2013).

The IRDC has V$_{LSR}$ = 95 km s^{-1} (Dunham et al., 2011b). As IRDCs are seen in absorption against the bright mid-IR background, we assume the near kinematic distance for this cloud of $\sim$ 5.5 kpc (assuming the rotation curve of Reid et al., 2009). At that distance, the beam size of the observations is approximately 0.08 pc (beam dimensions given in §2.2.2), and the field of view for each clump is about 3 $\times$ 3 pc. The active clump has a mass of $\sim 5000 - 10000$ M$_\odot$(total mass calculated by summing the Hi-GAL column density map derived in Chapter 4), and displays signs of active star formation; a 6.7 GHz methanol maser (Pestalozzi et al., 2005), 8 and 24 μm emission

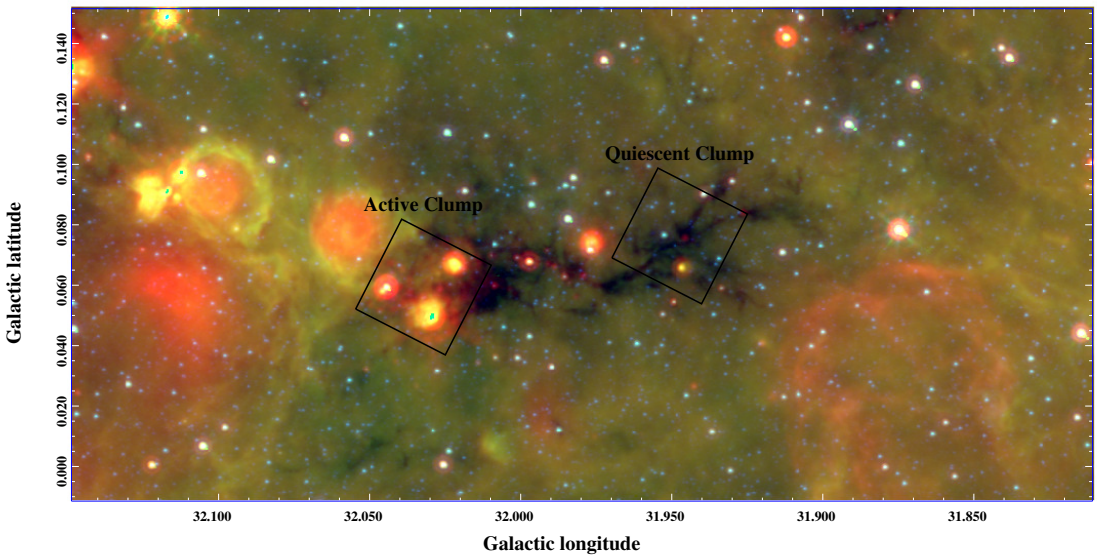

Figure 2.1: The IRDC observed, G32.02+0.06, embedded within a massive molecular filament. This particular IRDC shows many different stages of massive star formation, from extended HII regions to Infrared Dark cold gas. The two boxes delineate the active and quiescent clump VLA field-of-view's shown later in the paper. The background is a Spitzer 3 color image, Red: MIPSGAL 24 μm, Green and Blue: GLIMPSE 8 μm and 4.5 μm.

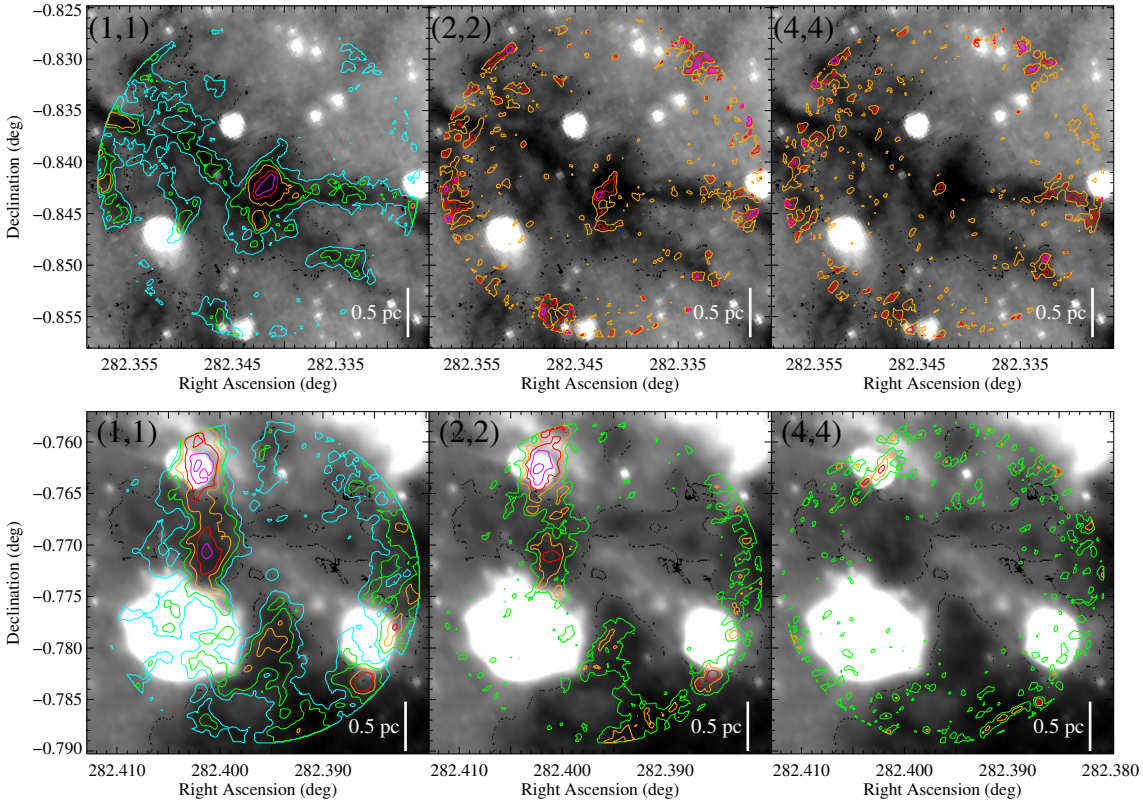

Figure 2.2: G32.02+0.06: GLIMPSE 8 μm grayscale image of the quiescent clump (*top*) and the active clump (*bottom*) with NH_3 contours. Note the excellent morphological agreement between the 8 μm extinction and the NH_3 emission. The quiescent clump shows no signs of massive star formation, while the active clump contains a range of star formation activity, from a young UCHII region that has blown out much of the dense gas and dust (the 8 μm bubble in the lower left of the image), to a cluster of cores showing 8 and 24 μm emission (in the top left) and an 8 μm dark complex in between. The lowest contour plotted in each panel corresponds to about 1 σ. *In the quiescent clump in the top panel: Left:* NH_3 (1,1) integrated intensity contours [10,20,30,50,70 mJy/beam km s^{-1}]. *Middle:* NH_3 (2,2) integrated intensity contours [30,50,70 mJy/beam km s^{-1}]. *Right:* NH_3 (4,4) integrated intensity contours [30,50,70 mJy/beam km s^{-1}]. *In the active clump in the bottom panel: Left:* NH_3 (1,1) integrated intensity contours [20,40,70,100,150,200 mJy/beam km s^{-1}]. *Middle:* NH_3 (2,2) integrated intensity contours [30,50,70 mJy/beam km s^{-1}]. *Right:* NH_3 (4,4) integrated intensity contours [40,70,100,150,200 mJy/beam km s^{-1}].

indicative of a handful of Ultra-Compact HII Regions ("Diffuse Red Clump" and 24 μm emission $\gtrsim$ 1 Jy Battersby et al., 2010), and radio continuum emission (White et al., 2005; Helfand et al., 2006). The active clump contains cores in Stages 2, 3, and 4 (see Figure 2.3). The quiescent clump has a mass of about 3000 $M_{\odot}$and shows very little to no signs of active star formation (the dense gas may be associated with a faint 24 μmpoint source near the clump center), and is seen in absorption at 8 μm, and contains only Stage 1 cores (see Figure 2.3).

2.2.2 Observations

We completed K-band observations of the (J,K) = (1,1), (2,2), and (4,4) inversion transitions of NH_3 over two tracks in the D configuration on 1 and 6 July, 2010 at the National Radio Astronomy Observatory[1] Karl G. Jansky Very Large Array (VLA) under project AG830. We observed two clump locations within IRDC G32.02+0.06, an active clump and a quiescent clump (with the presence/lack of star formation tracers as described in §2.2.1). Pointing, bandpass and flux calibrations were performed on observations of J1331+3030 (3C286) at the beginning of the shift. Pointing was performed twice more during each 3.5 hour observing shift on J1851+005. Phase calibration was done on J1851+005, a 1.1 Jy K-band calibrator 1.5^o from the IRDC, every 10 minutes, between quiescent and active clump observations.

The (1,1) inversion transition at 23694.4955 MHz was observed in the WIDAR OSRO2 mode with 1 subband/dual polarization mode with 8 MHz bandwidth and 256 channels for a resolution of 0.4 km s^{-1}. The (2,2) and (4,4) inversion transitions at 23722.599 MHz and 24139.352 MHz, respectively, were observed simultaneously in the WIDAR OSRO1 mode with 2 subbands/dual polarization mode with 4 MHz bandwidth and 64 channels each for a resolution of 0.8 km s^{-1}. The synthesized beam diameters for the (1,1), (2,2), and (4,4) observations, respectively, were $\sim 3.6'' \times 2.7''$, $\sim 3.5'' \times 3.0''$, $\sim 3.5'' \times 2.8''$. The beam position angle was about -40^o. The field of view for each clump was about $1.9' \times 1.9'$. The final RMS noise in each image was approximately 6

[1] The National Radio Astronomy Observatory is a facility of the National Science Foundation operated under cooperative agreement by Associated Universities, Inc.

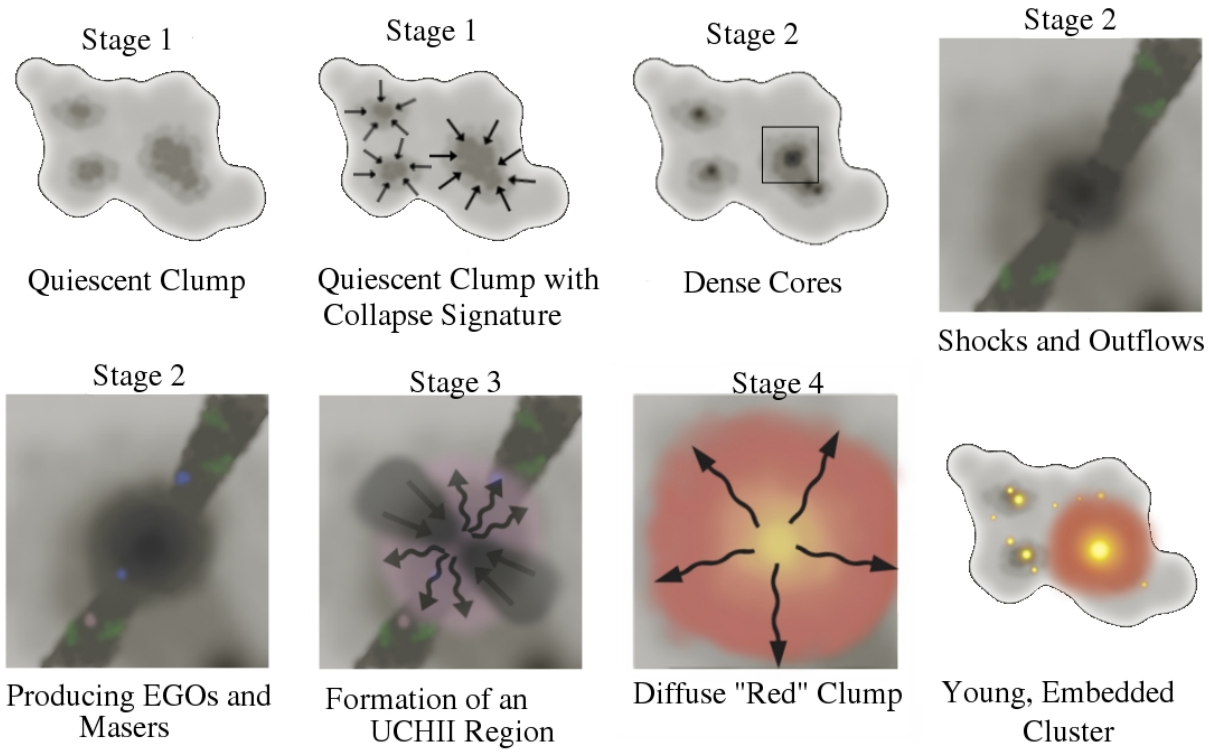

Figure 2.3: The proposed observational evolutionary sequence for massive star and cluster forming regions visible in dust continuum (sub-mm to far-IR) surveys, adapted from Battersby et al. (2010). The first stage is cold and dense, showing no signs of active massive star formation. This phase should appear as an IRDC if the viewing angle allows. Stage 2 sources show the beginning of massive star formation, in particular evidence of shocks and outflows, such as Extended Green Objects (EGOs, extended emission at 4.5 μm, indicative of shocks and outflows, Cyganowski et al., 2008) and Class II CH_3OH masers. Stage 3 is the beginning phases of an ultra-compact (UC) HII region, as indicated by free-free emission or radio recombination lines. Stage 4 is when the UCHII region UV-excites PAH emission at 8 μm, revealing itself as a diffuse 'red' clump in GLIMPSE (Benjamin et al., 2003) 8 μm images. The final observable stage in the dust continuum at long wavelengths is a young, embedded cluster (Lada & Lada, 2003).

mJy/beam (see §2.2.3 for details).

2.2.3 Data Reduction and Masking

The reduced NH_3 (1,1), (2,2), and (4,4) images are shown in Figure 2.2[2] . The VLA data were reduced using CASA, the Common Astronomy Software Applications package, version 3.3.0. We used standard CASA routines for the flux, bandpass, gain, and phase calibration. The UV continuum subtraction was done in the standard method (using the routine uvcontsub) for the quiescent clump and for the (1,1) transition of the active clump. The quiescent clump showed no continuum emission, and the active clump had one strong continuum emitter (see §2.4.6 for details). However, the (2,2) observations toward the active clump showed an instance of the (2,2) hyperfine transition toward one core complex. This prevented a traditional continuum subtraction, as the number of line-free channels was too few. Therefore, we subtracted the continuum derived from the (1,1) active clump observation from the (2,2) and (4,4) cubes.

The continuum subtracted cubes were then cleaned using a standard setup with the CASA clean command. We performed iterative masking while cleaning on all lines and both clumps except the (4,4) images whose signal was too low, so we cleaned without a mask and increased the cleaning threshold from one to three sigma (sigma as determined from the dirty maps). All of the images were primary beam corrected. All the images are weighted using "briggs" mode in CASA (Briggs et al., 1999). Two example spectra are shown in Figure 2.4.

The final RMS noise was calculated using the immoments routine in CASA on the line-free channels of the fully reduced, flux-corrected data cube. We give the approximate RMS noise values at two points in the map; the map center and the 50% power point of the primary beam. The RMS noise for the (1,1) observations were approximately 5 mJy/beam per 0.4 km s^{-1} channel in the center and 6 mJy/beam per 0.4 km s^{-1} channel at the 50% flux point.The (2,2) and (4,4) observations had the same RMS noise with values of approximately 6 mJy/beam per 0.8 km s^{-1} channel in the center and 9 mJy/beam per 0.8 km s^{-1} channel at the 50% flux point. A more sophisticated

[2] Fully reduced data cubes are available upon request.

calculation of the noise parameters was done with the line fitting and temperature modelling, as discussed in §2.3. Our continuum sensitivity in the (1,1) band is about 0.2 mJy.

Lastly, we applied a mask to each of the images in order to avoid image artifacts, low signal to noise, and unrelated regions. The first version of the mask was created on each of the hot and cold clump (1,1) data cubes. Using the integrated intensity, RMS, velocity, and velocity dispersion images calculated from immoments, we mmade a signal to noise cut of one on the (1,1) integrated intensity map. The next cut was that the velocity dispersion must be less than 5 km s^{-1} and that the velocity must be between 90 and 100 km s^{-1}, criteria which were easily met by the source signal. Finally, the application of the primary beam corrections lead to extremely noisy regions at the edges of the maps, as well as enhancing image artifacts in these regions. We exclude these regions by making a primary beam power point cutoff of 50%. These cutoffs were all performed on the (1,1) images, and constitute the final mask for the (1,1) images. These masks were then applied to each of the (2,2) and (4,4) images with the added cutoff that the signal to noise, in the (2,2) and (4,4) maps respectively, must be greater than one. These masks are then applied to the data and used throughout the remainder of this paper in the modeling, figures, and analyses.

2.2.4 Archival Data

To help understand the context and to determine some physical properties of this region, we utilize extant survey and literature data. We use mid-IR data taken with Spitzer as part of the Galactic Legacy Infrared Mid-Plane Survey Extraordinaire (GLIMPSE; Benjamin et al., 2003) and 24 μm data taken as part of the MIPS Galactic Plane survey (MIPSGAL Carey et al., 2009). We also use millimeter continuum data taken as part of the Bolocam Galactic Plane Survey[2] (BGPS; Aguirre et al., 2011; Rosolowsky et al., 2010) of the Galaxy at 1.1 mm as well as dust continuum data from the Herschel Infrared Galactic Plane Survey (Hi-GAL, Molinari et al., 2010). The Boston University-Five College Radio Astronomy Galactic Ring Survey (BU-FCRAO GRS; Jackson et al., 2006) provides spectral line data of ^{13}CO J=1-0. Complementary radio continuum data (from the

[2] http://irsa.ipac.caltech.edu/data/BOLOCAM_GPS/

VLA) is provided by the Multi-Array Galactic Plane Imaging Survey (MAGPIS; White et al., 2005; Helfand et al., 2006) at 6 and 20 cm and the HII Region Discorvery Survey (Anderson et al., 2011). Additionally, we used the single dish NH_3 data taken on the Green Bank Telescope as part of a survey of BGPS sources by Dunham et al. (2011b) in our original source selection.

2.3 Radiative Transfer NH_3 Modeling

The NH_3 inversion transitions are a sensitive probe of temperatures in cold molecular gas (Ho & Townes, 1983). The critical density of the (1,1) and (2,2) inversion transitions are similar at around $n_{crit} \approx 10^{4.5}$ cm^{-3}, implying that NH_3 emission will only be detected in the densest part of GMCs most likely to form stars. Throughout the text, we assume an abundance ($\frac{N(NH_3)}{N(H_2)}$), χ_{NH_3} = 4.6 $\times 10^{-8}$ derived using these data from Chapter 4.

The ammonia lines were fitted with a Gaussian line profile to each hyperfine component simultaneously with frequency offsets fixed. The fitting was performed in a python routine translated from Erik Rosolowsky's IDL fitting routines (Section 3 of Rosolowsky et al., 2008), which forward models all of the spectral lines given input physical properties derived assuming a homogeneous slab of uniform temperature, intrinsic velocity dispersion, and uniform excitation conditions for all the lines. The model was used within the framework of the `pyspeckit` spectral analysis code package (Ginsburg & Mirocha, 2011, `http://pyspeckit.bitbucket.org`). As in Rosolowsky et al. (2008), the emission is assumed to arise from a homogeneous slab with uniform gas temperature, intrinsic velocity dispersion, and uniform excitation conditions for all hyperfine transitions of the NH_3 lines. The model simultaneously fits the (1,1), (2,2), and (4,4) inversion transitions of para-NH_3 with 5 parameters: line excitation temperature T_{ex}, gas kinetic temperature T_{kin}, column density N(NH_3), velocity dispersion σ, and offset velocity v. The models are fit using a Levenberg-Marquardt fitting code using `scipy` (`http://scipy.org`, `https://github.com/newville/lmfit-py`).

Each pixel in the spectral data cubes was fitted independently. The fits require an input guess as a starting point for the fitting algorithm. The guess for each pixel was set to the nearest pixel with a valid fit to ensure continuity across the cube. The first fit was performed by hand on a bright pixel,

which was selected as the starting point for the loop. The Levenberg-Marquardt algorithm computes a covariance matrix for the fitted parameters, but we report only the independent component of the errors on each parameter. For optically thin lines, the column density and excitation temperature are degenerate, but they are fit independently so the data are treated consistently. Systematic offsets due to calibration errors could asymmetrically affect the temperature measurements, but because all three lines are observed simultaneously with the same calibration, such errors are expected to be small.

The fitted (1,1) total optical depths ranged from $\tau \sim 1$ (which is equivalent to $\tau \approx 0.5$ for the central hyperfine line) to $\tau \approx 80$ in some regions within the active clump (but see below) and $\tau \sim 40$ in one small region within the quiescent clump. For total (1,1) optical depths $\tau > 9$, the hyperfine lines have optical depths $\tau > 1$. Simulations show that the (1,1) line can be used to accurately measure the observed properties (to within the reported error) up to $\tau \approx 20$, and the combination of (1,1) and (2,2) are accurate up to the highest reported optical depths for kinetic temperatures above about 10 K because, for most combinations of optical depth and column density at which NH_3 is detectable, either the (1,1) hyperfine or the (2,2) main line are optically thin. As noted in Rosolowsky et al. (2008), T_{ex} and column density are degenerate in the optically thin limit (i.e., where even the core (1,1) line has $\tau \ll 1$), but this limit is essentially never reached at the sensitivity of our observations.

Typical statistical errors are in the range $\sigma(\mathrm{T}_K) \sim$ 1-3 K for the kinetic temperature, and $\sigma\left(\log[N(NH_3)]\right) \lesssim 0.05$ (or about 10%) for the column density of ammonia. The statistical errors are representative if the gas within a beam is at a single temperature. If there is gas at different temperatures within a single beam, the fitted temperature represents an average, but the errors do not reflect the underlying temperature distribution. This caveat affects any line-of-sight temperature measurement, but should be less severe for NH_3 than for dust temperatures because the NH_3 temperatures typically select a single dense cloud, while dust temperatures average all clouds along a line of sight.

The fitting algorithm will return spurious or unreliable results when there are multiple velocity

components along a line of sight. We therefore re-fit parts of the data where multiple components were observed by restricting the velocities and fitting each component separately (See §2.4.2). However, there are some 'transition regions' where the two components are blended, and a single fit misrepresents both. For additional information about caveats and uncertainties in NH_3 line fitting, refer to Rosolowsky et al. (2008) Section 3.

An additional mask (see §2.2.3) is applied to the model fit images as applied throughout the remainder of the paper. The only pixels that were excluded are obvious spurious bad model fits (e.g., a hot pixel) which were isolated spatially and therefore not physically reasonable. These exclusions do not affect the peak map values reported in §2.4. For the quiescent clump, these excluded pixels had a temperature less than 5 K or greater than 50 K or an H_2 column density of less than 10^{20} cm^{-2} or greater than 2×10^{23} cm^{-2} or with a (1,1) integrated flux of less than 0.01 Jy/beam km s^{-1}. For the active clump, these excluded pixels had a temperature less than 5 K or greater than 50 K or a column density of less than 10^{20} cm^{-2} or greater than 10^{24} cm^{-2} or with a (1,1) integrated flux of less than 0.02 Jy/beam km s^{-1}.

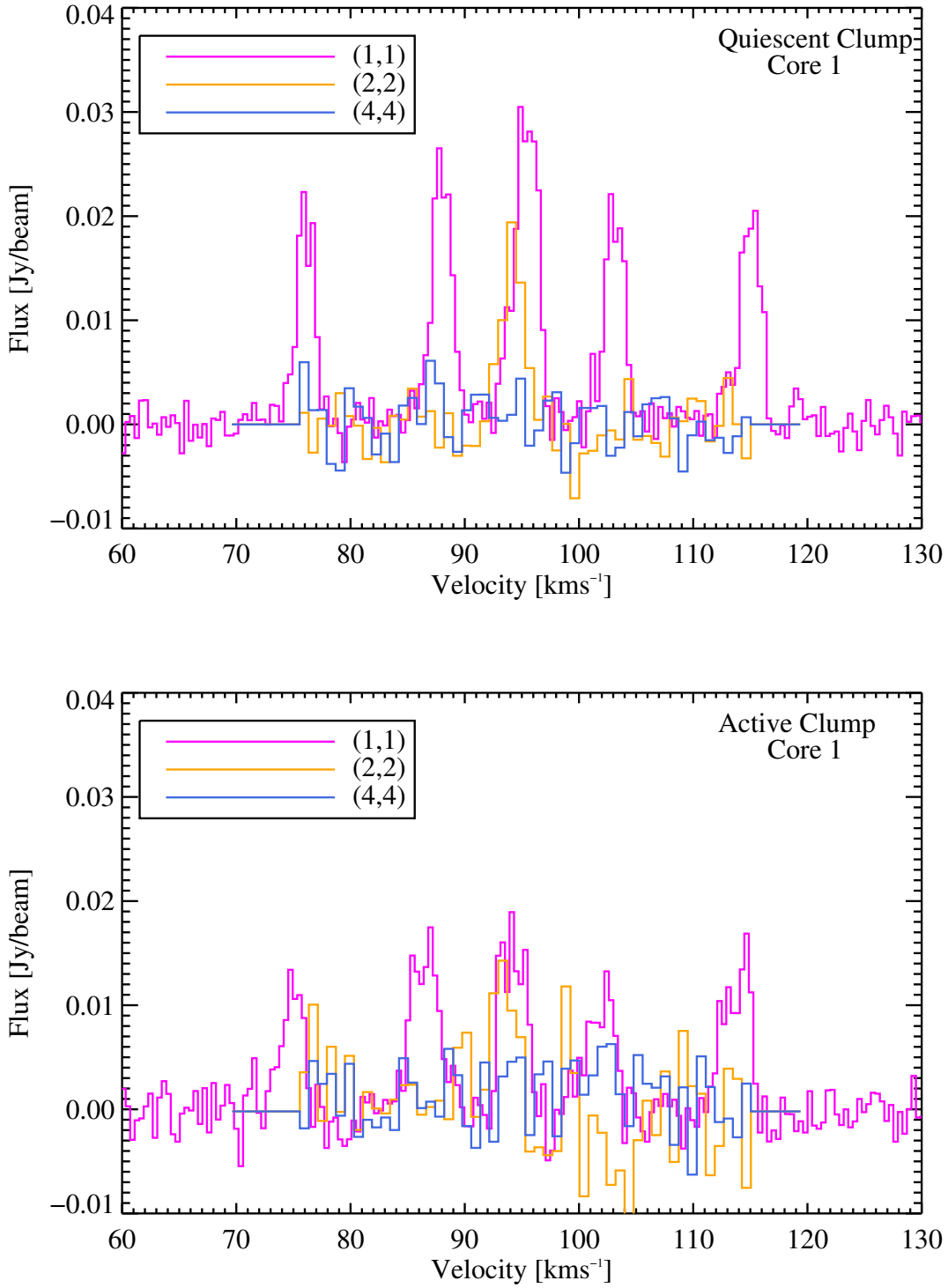

Figure 2.4: Example NH_3 (1,1), (2,2), and (4,4) spectra (in magenta, orange, and blue, respectively) averaged over Core 1 of the Quiescent clump at *top* and Core 1 of the Active clump at *bottom* (see §2.4.2.1 for details on core identification).

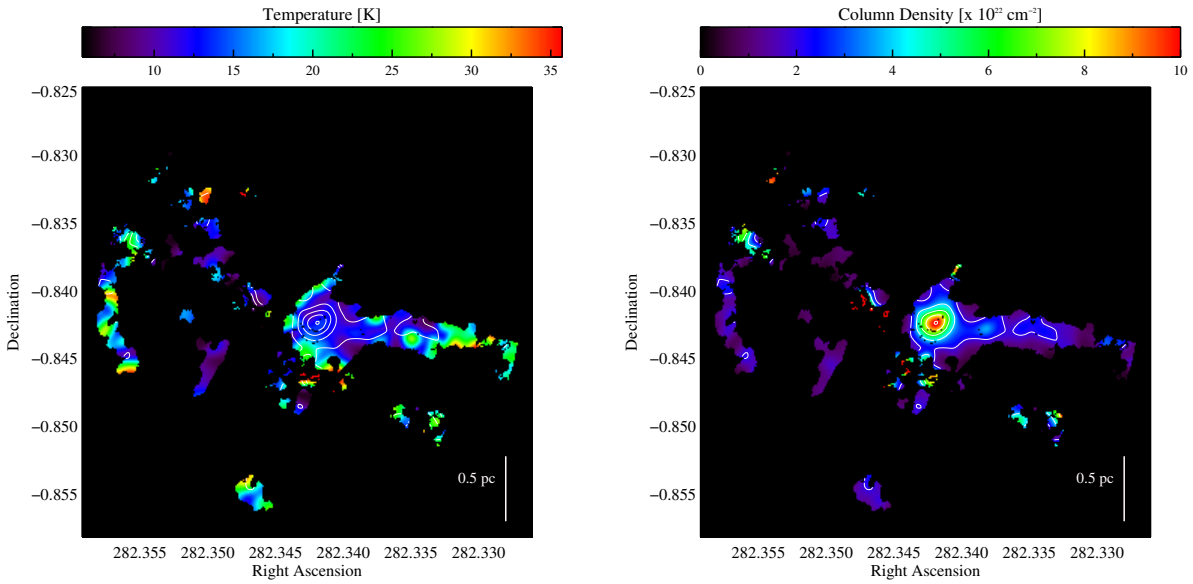

Figure 2.5: Quiescent clump: Temperature and column density maps as derived from the radiative transfer model fits (see §2.3). The contours are $N(H_2) = [2,4,6,8,10] \times 10^{22}$ cm^{-2} assuming an abundance of 4.6×10^{-8} from Chapter 4. Pictured here is the "low velocity" component of the quiescent clump, pixels with peak velocities from 93 to 97.3 km s^{-1}. The column densities of the two components are superposed in Figure 2.8.

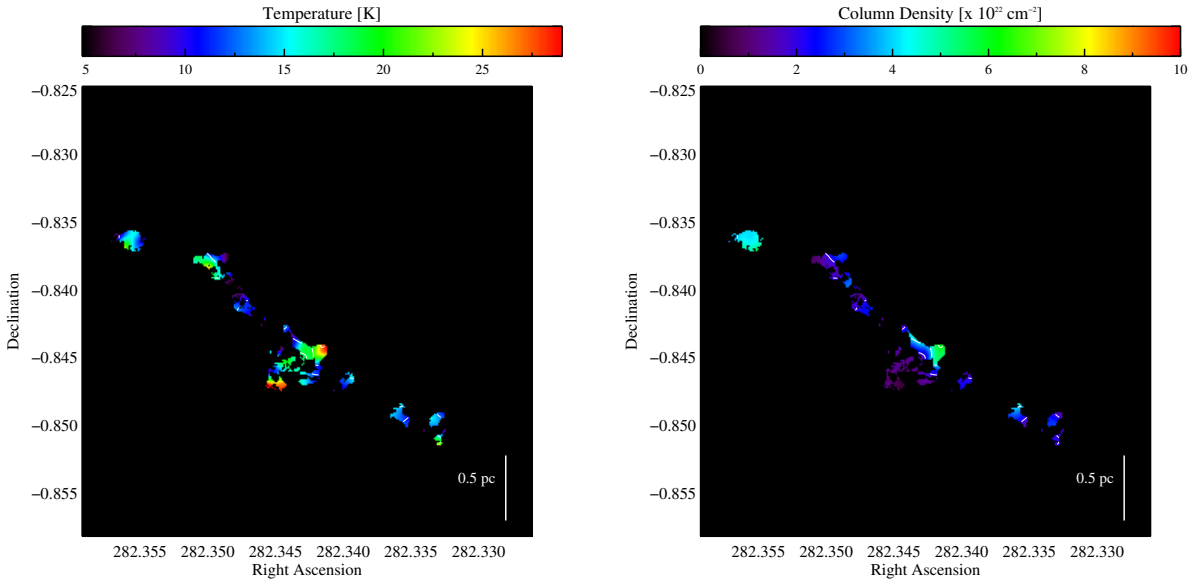

Figure 2.6: Quiescent clump: Temperature and column density maps as derived from the radiative transfer model fits (see §2.3). The contours are $N(H_2) = [2,4,6,8,10] \times 10^{22}$ cm^{-2} assuming an abundance of 4.6×10^{-8} from Chapter 4. Pictured here is the "high velocity" component of the quiescent clump, pixels with peak velocities from 97.3 to 101 km s^{-1}. The column densities of the two components are superposed in Figure 2.8.

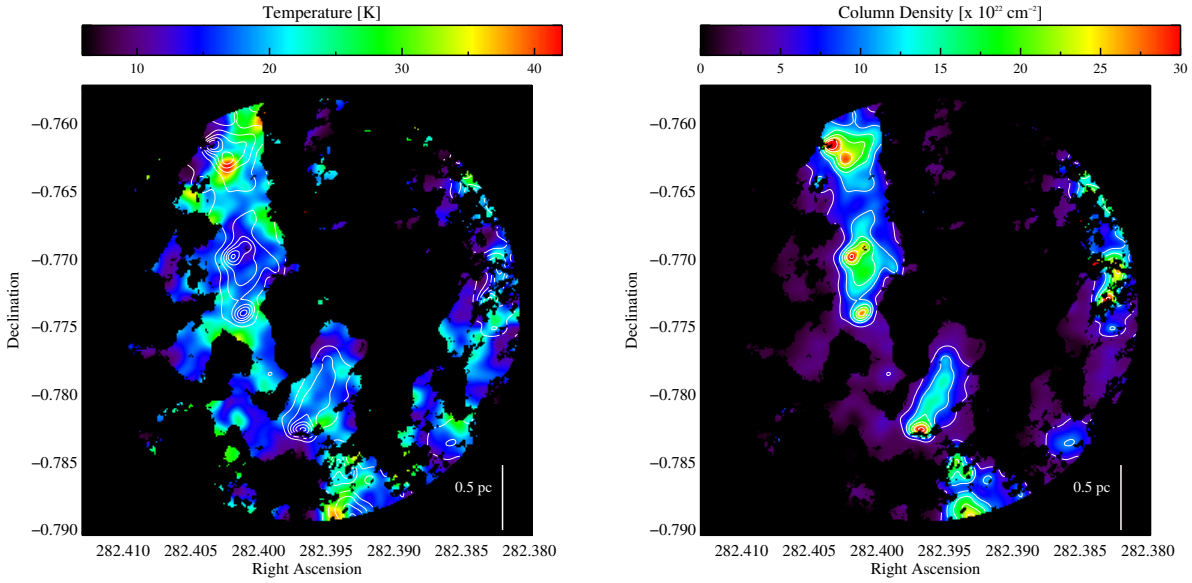

Figure 2.7: Active clump: Temperature and column density maps as derived from the radiative transfer model fits (see §2.3). The contours are $N(H_2) = [5,10,15,20,25,30] \times 10^{22}$ cm^{-2} assuming an abundance of 4.6×10^{-8} from Chapter 4.

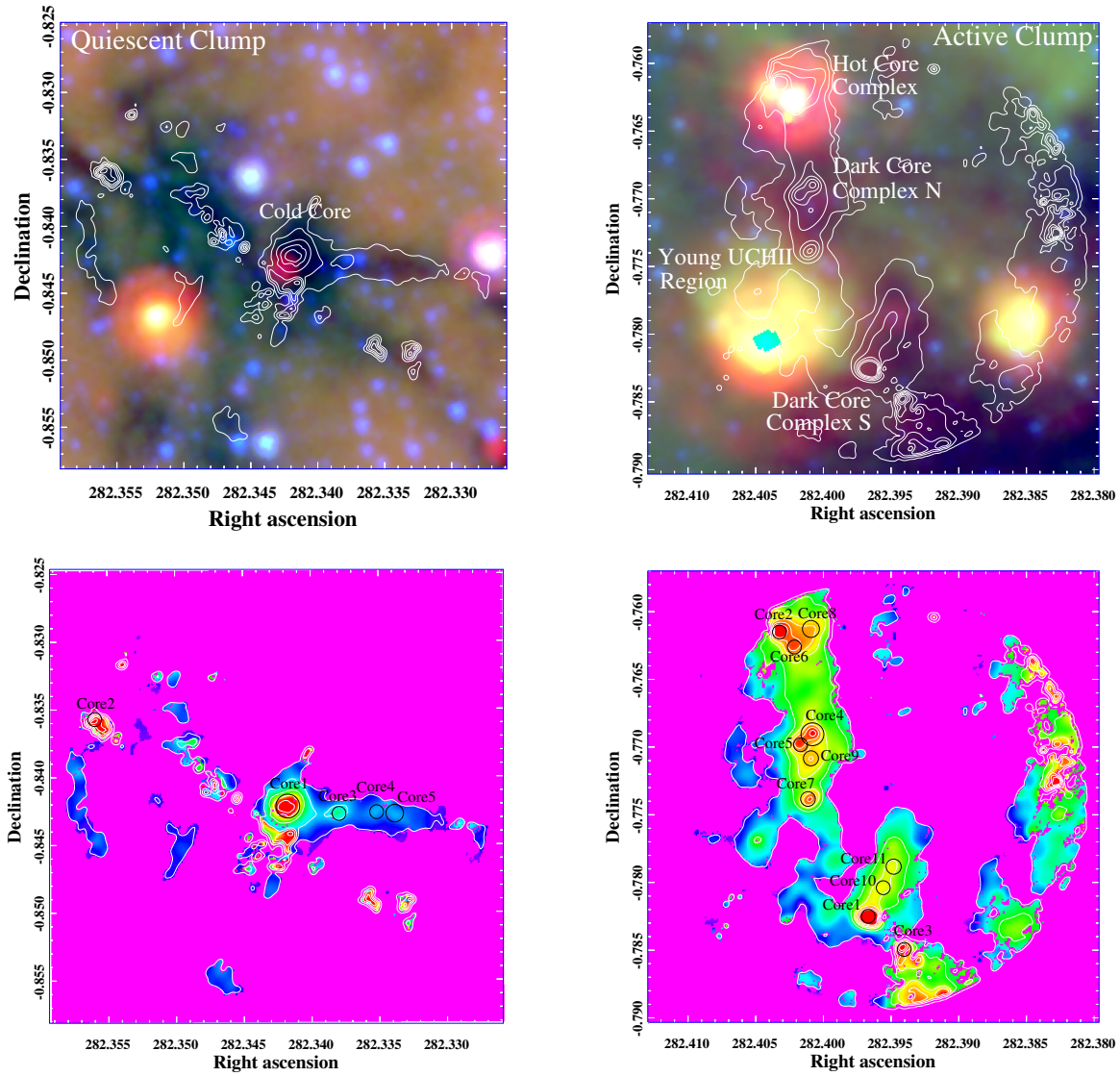

Figure 2.8: The various cores and complexes discussed throughout the text are labeled here. *Top:* Three color mid-IR image of each clump (MIPSGAL, GLIMPSE, Red: 24 μm, Green: 8 μm, Blue: 4.5 μm) with column density contours derived from NH_3 (six linearly spaced contours, in the quiescent clump from 8×10^{21} cm^{-2} to 10^{23} cm^{-2} and from 10^{22} cm^{-2} to 3×10^{23} cm^{-2} in the active clump). *Bottom:* The column density map derived from NH_3 (with contours as above) with core sizes and locations plotted. The cores are plotted as circles with the effective radii of the 2-D Gaussian fits.

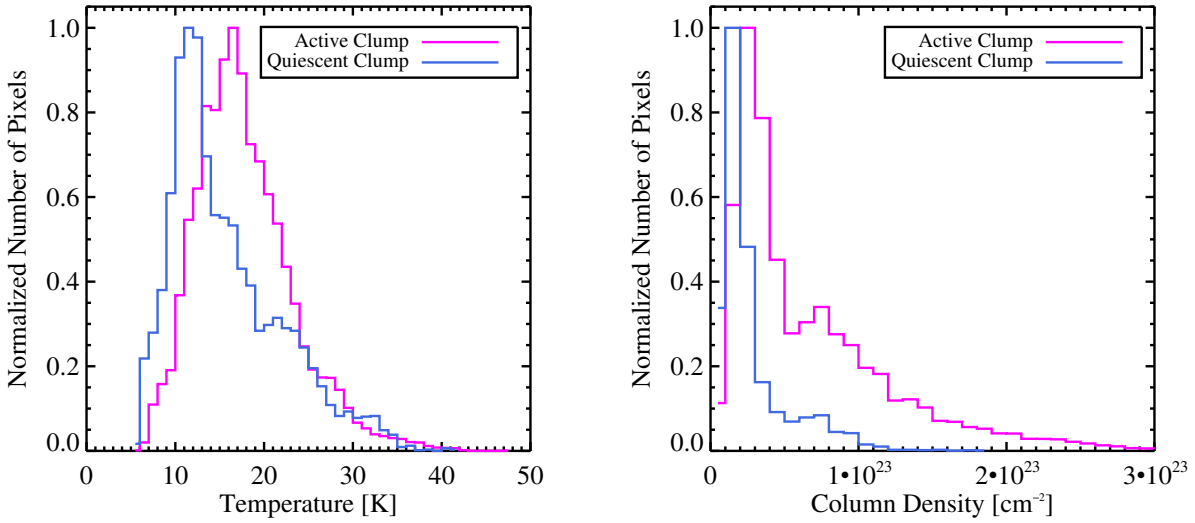

Figure 2.9: Histograms of the kinetic temperatures (*left*) and column densities (*right*) in the active and quiescent clumps. Both distributions have a wide spread (standard deviation is ∼6 K in temperature for both clumps and $\sim 2\times10^{22}$ cm^{-2} in column density for the quiescent clump and $\sim 6\times10^{22}$ cm^{-2} for the active clump) but the median pixel value in the quiescent clump is colder (14 K vs. 17 K) and lower column density (2×10^{22} cm^{-2} vs. 5×10^{22} cm^{-2}) than the active clump.

Table 2.1: Core Complex and Filament Coordinates

Name	(α, δ) J2000
Quiescent Clump	
Core1	(18:49:22.0,-0:50:31.8)
Core2	(18:49:25.4,-0:50:08.6)
Core3	(18:49:21.1,-0:50:33.8)
Core4	(18:49:20.4,-0:50:33.4)
Core5	(18:49:20.1,-0:50:33.8)
Active Clump	
Hot Complex	
Core2	(18:49:36.8,-0:45:41.4)
Core6	(18:49:36.5,-0:45:45.4)
Core8	(18:49:36.2,-0:45:40.6)
Dark Complex N	
Core4	(18:49:36.2,-0:46:08.6)
Core5	(18:49:36.4,-0:46:11.4)
Core7	(18:49:36.3,-0:46:25.8)
Core9	(18:49:36.2,-0:46:15.0)
Dark Complex S	
Core1	(18:49:35.2,-0:46:57.0)
Core3	(18:49:34.6,-0:47:05.8)
Core10	(18:49:34.9,-0:46:49.4)
Core11	(18:49:34.7,-0:46:43.8)

Table 2.2: Core Complex and Filament Properties

Name	Radius[a] [pc]	Mass[b] [$M_\odot$]	$M_{MSF}(r)$[c] [$M_\odot$]	Peak $N(H_2)$ [cm^{-2}]	Peak $n(H_2)$[d] [cm^{-3}]	Peak Σ_{H_2} [g cm^{-2}]	T_{mean} [K]
Quiescent Clump							
Core1	< 0.12	65	52	1.0×10^{23}	$> 1.4 \times 10^5$	0.47	13
Core2	< 0.07	23	25	1.2×10^{23}	$> 2.8 \times 10^5$	0.56	20
Core3	< 0.07	10	25	4×10^{22}	$> 9 \times 10^4$	0.19	13
Core4	< 0.07	7	25	2×10^{22}	$> 5 \times 10^4$	0.09	15
Core5	< 0.09	11	35	2×10^{22}	$> 4 \times 10^4$	0.09	12
Filament	< 0.08	2500		Avg$\sim 2 \times 10^{22}$	$> 4 \times 10^4$	0.09	10-15
Active Clump							
Hot Complex							
Core2	< 0.07	110	25	5.0×10^{23}	$> 1.2 \times 10^6$	2.3	14
Core6	< 0.07	82	25	2.8×10^{23}	$> 6.5 \times 10^5$	1.3	34
Core8	< 0.08	88	30	2.2×10^{23}	$> 4.5 \times 10^5$	1.0	25
Dark Complex N							
Core4	< 0.11	180	46	3.5×10^{23}	$> 5.2 \times 10^5$	1.6	14
Core5	< 0.07	80	25	3.1×10^{23}	$> 7.2 \times 10^5$	1.4	15
Core7	< 0.07	65	25	2.7×10^{23}	$> 6.3 \times 10^5$	1.3	17
Core9	< 0.08	66	30	1.9×10^{23}	$> 3.8 \times 10^5$	0.89	16
Dark Complex S							
Core1	< 0.07	145	25	7.1×10^{23}	$> 1.6 \times 10^6$	3.3	14
Core3	< 0.07	71	25	3.9×10^{23}	$> 9.0 \times 10^5$	1.8	23
Core10	< 0.07	47	25	1.5×10^{23}	$> 3.5 \times 10^5$	0.70	18
Core11	< 0.08	50	30	1.5×10^{23}	$> 3.0 \times 10^5$	0.70	17
Filament	< 0.14		4800	Avg$\sim 5 \times 10^{22}$	$> 6 \times 10^4$	0.23	15-20

[a]The effective radius of the 2-D Gaussian Fit (a circle with this radius has the same area as the area under the Gaussian, $r_{eff} = \sqrt{2}\sigma$). The resolution limit is $\sim$0.07 pc so many of these are unresolved. The source sizes are not de-convolved and are therefore upper limits, the de-convolved source sizes are presented in §2.4.2.1. For the filament, the value reported is approximately the radius of the cylindrical filament.
[b]The mass from the NH_3 column density map within the effective radius.
[c]Mass threshold for forming massive stars within the given radius, from Kauffmann & Pillai (2010).
[d]The peak $N(H_2)$ divided by 2$\times$ the radius. These densities are all lower limits since the radii are all upper limits.

2.4 Results

2.4.1 Errors

We summarize here the statistical and model errors, as well as estimated systematic errors on derived quantities. As discussed in §2.2.2 and 2.2.3, typical statistical errors on the NH_3 fluxes are about 6 mJy/beam. This translates to typical model fit errors in the temperatures of 1-3 K and about 10% ($\sigma(\log[N(NH_3)]) \lesssim 0.05$) in $N(NH_3)$. Given typical distance (20%), opacity (100%), and flux density (10%) uncertainties, Battersby et al. (2010), using Monte Carlo simulations, found that typical systematic mass uncertainties are roughly a factor of two. This does not include the unknown uncertainties associated with depletion, abundance variations, line blending, and varying excitation conditions in different NH_3 lines. The systematic uncertainties in the temperature are also due to those unknown uncertainties which we are unable to quantify. In summary, the masses are uncertain by about a factor of two and the column densities are slightly better (no uncertainty in distance). The temperatures are at best good to 1-3 K.

The uncertainties in the radii are due to distance uncertainties and resolution effects. The distance uncertainty gives about a 20% uncertainty in the radius, while the resolution effect simply means that we are only sensitive to source sizes larger than our beam (about 0.07 pc radius) and true source sizes measured to be 0.07 pc are certainly smaller.

2.4.2 The Model Fits

The radiative transfer model fits are presented in Figures 2.5, 2.6 (quiescent clump), and 2.7 (active clump). There are two distinct kinematic components (referred to as the "low", from 93 to 97.3 km s^{-1}, and "high", from 97.3 to 101 km s^{-1}, velocity components) in the quiescent clump which were fit separately. The "low" and "high" velocity components are clearly associated (spatial overlap and very close in velocity space) with the strongest overlap region being in the Northeast end of the filament (near α = 282.355, δ = -0.837, Core 2). The column densities of the two components are superposed in Figure 2.8. Throughout the text, we assume an abundance ($\frac{N(NH_3)}{N(H_2)}$),

Table 2.3: Core Complex and Filament Star-Forming Activity

Complex Name[a]	8 μm	24 μm source?	Free-Free?[b]	Maser?[c]	Evolutionary Stage[d]
Quiescent Clump					
Core 1	Dark	No	No	No	1
Cores 2,3, and 4	Dark	No	No	No	1
Filament	Dark	No	No	No	1
Active Clump					
Hot Core Complex	Bright	Yes	No	No	3
Dark Core Complex N	Dark	No	No	Yes	2
Dark Core Complex S	Dark	No	No	Yes	2
UCHII Region	Bright	Yes	Yes	No	4
Filament	Dark	No	No	No	1

[a]Complexes are shown in Figure 2.8.
[b]See §2.4.6.
[c]6.7 GHz CH_3OH Maser Pestalozzi et al. (2005); Szymczak et al. (2002). The positional accuracy of this detection is about 30" and the position overlaps both dark core complexes.
[d]Battersby et al. (2010) and Figure 2.3.

χ_{NH_3} = 4.6 $\times 10^{-8}$ from Chapter 4. The hypothesis that the low- and high-velocity filament components represent different components (shock accelerated and 'stationary') of material from UV-driven compression will be discussed in the companion paper (Battersby et al., 2013). These kinematically distinct interacting filaments bear morphological similarity to W33A as presented by Galván-Madrid et al. (2010).

The active clump also consists of multiple components. However, these were heavily blended and therefore were unable to be fit separately. Sharp gradients in the fits were created by the model switching between two components. To create a smooth, averaged gradient across the maps, the model fits were convolved with the observed beam ($\sim 3''$). This reduces the effective resolution slightly and overestimates the size scale of the different cores along the line of sight.

2.4.2.1 Core Identification

Cores were identified in the column density maps by fitting a 2-D Gaussian to the brightest point in the map, subtracting it off, and re-iterating (similar to Brogan et al., 2009; Rathborne et al., 2006). All the core fits were inspected by eye. The cores are plotted in Figure 2.8 with their effective radii (a circle with this radius has the same area as the area under the Gaussian, $r_{eff} = \sqrt{2}\sigma$). The core parameters reported in Table 2.2 are derived within this effective radius. This method of identifying cores does not provide a complete sample and is meant to be representative of the brightest cores. The core sizes reported in Table 2.2 and throughout are not de-convolved. The sizes of cores with reported radii of 0.07 pc are unresolved and their sizes are only constrained to be smaller than the 0.07 pc resolution limit. The de-convolved source radii of 0.08 pc, 0.09 pc, 0.11 pc, and 0.12 pc sources are 0.04 pc, 0.06 pc, 0.08 pc, and 0.10 pc, respectively.

2.4.2.2 The Temperature Structure of the Clumps

The kinetic temperature histogram is shown in Figure 2.9, and the region properties are summarized in Tables 2.2 and 2.3, while the sub-regions discussed are labeled in Figure 2.8. Both clumps range from about 8 to 35 K. The quiescent clump exhibits a smooth spatial distribution

in temperature in the interior of the filament from about 8 to 15 K. The temperature decreases towards the interior of the filament from about 20 K to 12 K. Interestingly, the main core (Core 1) of the quiescent clump shows no gradient in temperature and is approximately 13 K. The high velocity kinematic component of the quiescent clump shows a clumpier and slightly warmer ($\sim$ 15 K) temperature structure. Core 2 is approximately the overlap region of the two velocity components making the parameter estimation more difficult, but the derived kinetic temperature is about 20 K. Cores 3, 4, and 5 are all colder at about 12-15 K, but their column density structures do not seem to be well approximated by a simple 2-D Gaussian.

The temperature structure of the active clump is more varied than the quiescent clump. The temperature ranges from about 10 K in the coldest portions to over 40 K in the warmest core (Core 6). The temperature structure appears to be fairly smooth and cold (10 to 20 K) over the majority of the active filament which is only disrupted by the warm pockets (30-40 K) of star formation. The active clump has both warm (40 K) and cold (12-15 K) cores. The hot core complex in the north of the filament has a smooth, warm temperature of about 20 K with gradual increases to about 40 K toward Core 2, but not directly peaking at the core center, perhaps indicating a newly formed star providing an internal heating source (at the temperature peak) and a pre-stellar dense core (at the column density peak). Both of the dark core complexes (N and S) have smooth, cold temperature fields of about 12-15 K. Most of the cores in the dark core complexes show no gradient in temperature and are roughly the same temperature as the filament at about 15 K. However, the southernmost core (Core 7) in the dark core complex N shows a decrease in temperature toward its center, from $\sim$ 20 K to 15 K.

2.4.2.3 The Column Density Structure of the Clumps

The column density histogram for both clumps is shown in Figure 2.9 and region properties are summarized in Tables 2.2 and 2.3, while the sub-regions discussed are labeled in Figure 2.8. The azimuthally averaged N(H_2) radial profiles are shown in Figure 2.10. The active clump has an overall higher column density, with a peak column density of about 3.3×10^{23} cm^{-2} and a median

column density of about 5×10^{22} cm^{-2}. The peak of the quiescent clump is about 1.1×10^{23} cm^{-2} while the median is about 2×10^{22} cm^{-2}.

The Active Clump: There are three main clusters of cores in the active filament, a northern hot core complex (IR-bright, about 35-40 K) and two dark core complexes, North and South (IR-dark and cold, about 15 K) in the middle and bottom of the filament. The young UCHII region (see §2.4.6) seen as a bubble in NH_3 could indicate a previous core complex or a more massive core complex at the same age. In the active clump, the cores are characterized by column densities of 2-3 $\times 10^{23}$ cm^{-2} or surface density of 1 g cm^{-2} ($\sim 2.1 \times 10^{23}$ cm^{-2}), just above the theoretical limit for forming massive stars (Krumholz & McKee, 2008). The filament in the active clump ranges from about 3×10^{22} cm^{-2} to 1×10^{23} cm^{-2}.

The young UCHII Region and the three core complexes in the active clump along the filament are separated by about 30″ (0.8 ± 0.1 pc). The cores themselves remain nearly unresolved (at 0.1 pc) but their separations (average separation to nearest neighbor within each complex) are about 6″ (0.16 ± 0.04 pc) with two larger (11″ and 13″, ∼0.3 pc) separations.

The Quiescent Clump: The quiescent clump has one large (Core 1, about 9″ or 0.24 pc diameter) core at the center with a few more small, low significance cores throughout. The central core has a column density of about 1.1×10^{23} cm^{-2}. This core at present is just below the predicted 1 g cm^{-2} threshold column density for forming massive stars (2.1×10^{23} cm^{-2} Krumholz & McKee, 2008), but is still very extended (see Figure 2.10), and we estimate our column densities only to be good to about a factor of two (§2.4.1). If this core condensed by a factor of $\sqrt{2}$ in radius to 6″ it could reach this predicted threshold. Additionally, a significant amount of large scale structure is missed in the interferometer observations, and as seen Table 2.2, Core 1 is above the observational cutoff for massive star formation determined in Kauffmann & Pillai (2010), so it is likely that the quiescent clump will also form massive stars. Presumably, the cold core may condense further through gravitational contraction and fragment to produce a core complex similar to that seen in the active clump, a scenario we will test using the gas kinematics in the companion paper (Battersby et al., 2013). The overall mass (about 3000 $M_\odot$) of the entire quiescent clump is about 2 to 3 times

less than the active clump, and so would need to accrete significant mass were it to mirror the active clump, a scenario suggested to occur in massive star forming regions (e.g., Longmore et al., 2011). The secondary, low significance cores have column densities of about 2-4 $\times$ 10^{22} cm^{-2} and sizes near the resolution limit at $4''$ (0.1 pc, see Table 2.2) and do not seem well characterized by a simple 2-D Gaussian. The core separations range from $5''$ to about $10''$ to about $1'$ (0.1 pc to 0.3 pc to 1.5 pc).

2.4.3 Fragmentation

The young UCHII Region and the three core complexes in the active clump along the filament are separated by about 0.8 ($\pm$ 0.1) pc. The cores themselves remain nearly unresolved but their separations (average separation to nearest neighbor within each complex) are about 0.16 ($\pm$ 0.04) pc. The Jeans length in the active clump given typical conditions (n = 6×10^5 cm^{-3}, T = 40 K and T = 15 K, respectively) is 0.03 pc (for 40 K, 0.02 pc for 15 K). The cores in the quiescent clump are separated by 0.1 to 1.5 pc, while a typical Jeans length is about 0.04 pc (n = 9×10^4 cm^{-3}, T = 10 K). The thermal Jeans length is well below our resolution limit. The fragmentation scale we observe in the active clump is more likely indicative of the turbulent fragmentation length scale (as in e.g., Zhang & Wang, 2011; Li et al., 2013).

2.4.4 Virial Parameter

We calculate a virial mass and virial parameter for each core using the average NH_3 (1,1) line width in each core. The calculation for the virial mass assumes that the core is bound and in virial equilibrium. If the derived virial mass is less than the measured cores mass ($\alpha_{\rm vir} < 1$), the core is sub-virial and may be collapsing. For a core with a density profile of $\rho(\mathrm{r}) \propto \mathrm{r}^{-p}$, the virial mass is given by

$$\mathrm{M_{vir}} = 3\left[\frac{5-2p}{3-p}\right]\frac{\mathrm{R}\sigma^2}{\mathrm{G}} \tag{2.1}$$

where σ is the average line-of-sight velocity dispersion, R is the core radius, and G is the gravitational constant. We adopt a value of p = 1.8 for the spectral index, which was the mean in a

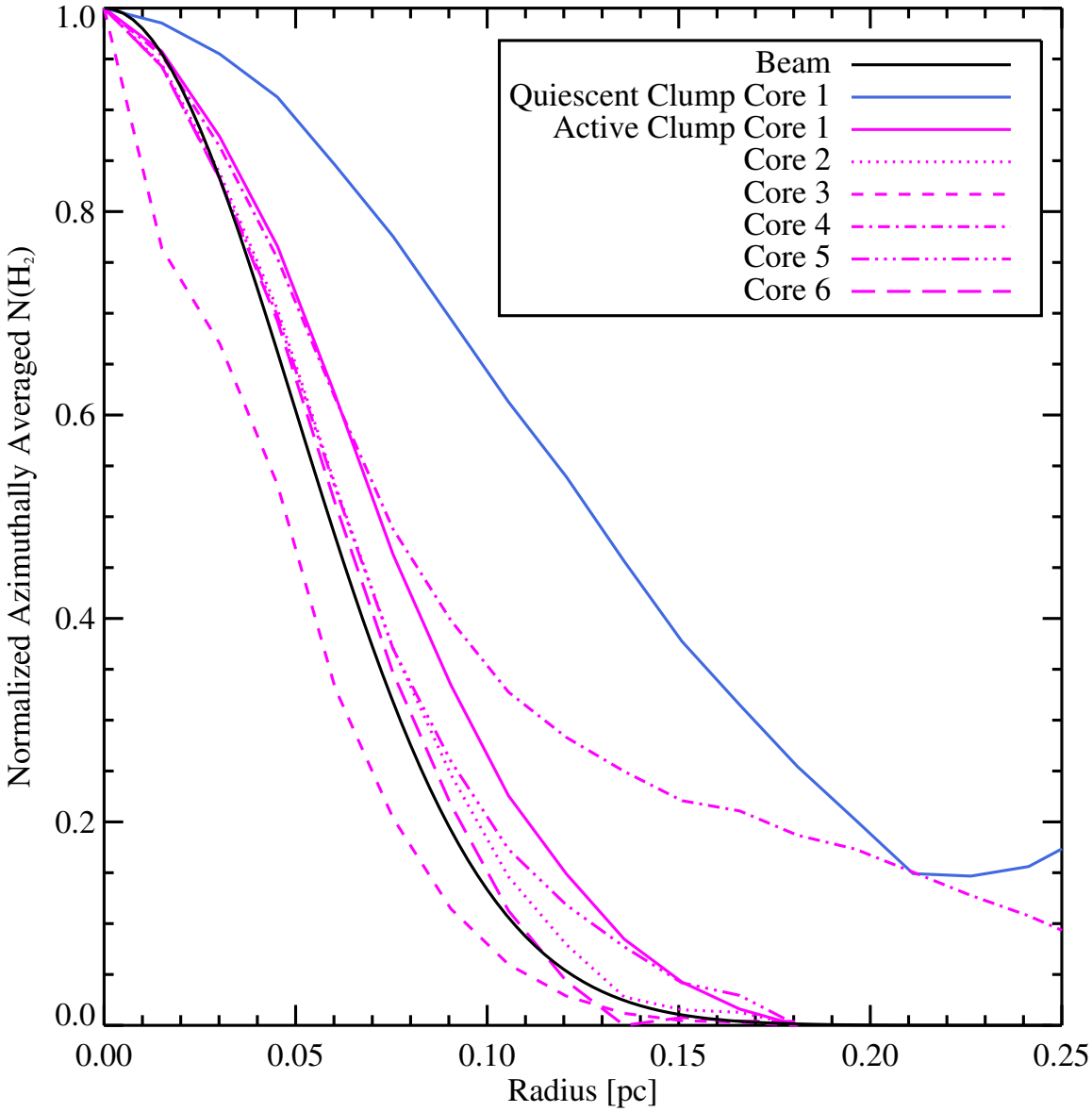

Figure 2.10: The normalized azimuthally averaged $N(H_2)$ radial profiles of some of the brightest cores as a function of radius in pc. Most are just barely resolved and mimic the beam profile (shown in black), while Quiescent Core 1 (blue solid line) is clearly much more extended. Core 3 has unsampled points around it, hence its having a lower azimuthally averaged profile than the beam.

sample of 31 massive star forming regions by Mueller et al. (2002). We do not make any correction for ellipticity as the cores were all well approximated by circular 2-D Gaussians. The expression for the virial mass reduces to

$$M_{vir} = 147\left(\frac{R}{1pc}\right)\left(\frac{\Delta v_{fwhm}}{1\ km\ s^{-1}}\right)^2 M_{\odot}. \quad (2.2)$$

The virial masses and parameters are reported in Table 2.4. With the exception of Active Clump Cores 6 and 9, all the cores are sub-virial, implying that they are unstable against collapse. In other words, the thermal plus non-thermal pressure support as indicated by the NH_3 linewidths is insufficient to support most of the cores against collapse. Given the true systematic uncertainties of the mass estimates (see §2.4.1, about a factor of two) the virial parameters are in some cases not strongly constrained to be less than one.

2.4.5 Evolutionary Stages

The quiescent and active clumps observed in this IRDC show the full range of evolutionary stages from cold, dark, and quiescent (Stage 1) up to a young UCHII Region (Stage 4, see Table 2.3). We characterize the evolutionary stage of the core complexes in each clump according to the sequence presented in Battersby et al. (2010), and updated in Figure 2.3 (see also, e.g., Chambers et al., 2009; Purcell et al., 2009). In doing this analysis we make the pivotal assumption that each core complex has a similar eventual fate and that differences between the complexes can be attributed to evolutionary stage alone. While this crucial assumption has plausible reasoning (similar typical core masses, sizes, and separations, and the overall clump column density and temperature structure and very similar), it is inherently uncertain and it is important to take the analysis which follows with some degree of skepticism. The quiescent clump shows little to no signs of active star formation (see §2.2.1, no 6.7 GHz CH_3OH maser, no significant 8 μm emission or free-free emission, but there is a possible association with a faint 24 μm point source). The active clump, however, shows a range of star formation activity consistent with the evolutionary sequence presented in Battersby et al. (2010), with the exception of the appearance of the 24 μm source which has been shown to come later in Chapter 3. This is reflected in the updated evolutionary sequence shown in Figure 2.3.

The young UCHII region in the active clump is the most evolved, categorized to be in Stage 4 (Battersby et al., 2010), followed by the Stage 3, 8 μm bright, warm (but lacking significant free-free emission) hot core complex in the north, while the two Stage 2, cold 8 μm dark core complexes seem to be the youngest. The hot core complex and dark core complexes exhibit very similar properties in their density structure, both with column densities above the predicted threshold of 1 g cm^{-2} for forming massive stars (Krumholz & McKee, 2008). The hot core complex shows signs of a forming massive star, while the dark core complexes appear to be in a pre-stellar state. The core complexes observed in this IRDC show good agreement with the evolutionary sequence from Battersby et al. (2010) as updated in Figure 2.3, spanning the range from Stage 1 to Stage 4 with

Table 2.4: Virial Parameters

Name	Radius[a] [pc]	Mass[b] [$M_\odot$]	M_{vir}[c] [$M_\odot$]	α_{vir}[d]	Avg. σ_v [km s^{-1}]
Quiescent Clump					
Core1	< 0.12	65	< 25	< 0.4	0.5
Core2	< 0.07	23	< 2	< 0.1	0.2
Core3	< 0.07	10	< 2	< 0.2	0.2
Core4	< 0.07	7	< 2	< 0.3	0.2
Core5	< 0.09	11	< 4	< 0.4	0.2
Active Clump					
Hot Complex					
Core2	< 0.07	110	< 68	< 0.6	1.1
Core6	< 0.07	82	< 108	< 1.3	1.4
Core8	< 0.08	88	< 58	< 0.7	0.9
Dark Complex N					
Core4	< 0.11	180	< 99	< 0.6	1.0
Core5	< 0.07	80	< 79	< 1.0	1.2
Core7	< 0.07	65	< 17	< 0.3	0.5
Core9	< 0.08	66	< 85	< 1.3	1.2
Dark Complex S					
Core1	< 0.07	145	< 16	< 0.1	0.5
Core3	< 0.07	71	< 61	< 0.9	1.0
Core10	< 0.07	47	< 21	< 0.4	0.6
Core11	< 0.08	50	< 22	< 0.4	0.6

[a] The effective radius of the 2-D Gaussian Fit (a circle with this radius has the same area as the area under the Gaussian, $r_{eff} = \sqrt{2}\sigma$). The resolution limit is ∼0.07 pc so many of these are unresolved. The source sizes are not de-convolved and are therefore upper limits, the de-convolved source sizes are presented in §2.4.2.1. For the filament, the value reported is approximately the radius of the cylindrical filament.

[b] The mass from the NH_3 column density map within the effective radius, assuming $\chi_{NH_3} = 4.6 \times 10^{-8}$.

[c] Virial Mass as calculated in §2.4.4, these are upper limits as the radius is not de-convolved.

[d] $\alpha_{vir} = M_{vir}$ / M, a value less than 1 implies that the core is collapsing. These are upper limits as the radius is not de-convolved

the derived temperatures increasing from the youngest to the most evolved phase.

Given the similar column density structure of the dark core complexes and the hot core complex (similar peak column densities, source sizes, and separations), the inference that these complexes represent similar regions in different stages of evolution seems plausible. The quiescent clump, alternatively, has a different column density structure than any of the active clump core complexes, so the assumption of evolution of star formation tracers (made previously in the active clump) must also include an assumption about the evolution of the column density structure. If indeed it will form a similar complex in its future, this implies something significant about the evolution of structure in IRDCs. Observations of a statistically significant sample of such core complexes could place constraints on the timescale of core formation, their properties, and how long they survive in a pre-stellar state. The observations presented here and in other works in the literature (e.g., Zhang & Wang, 2011; Pillai et al., 2011; Beuther et al., 2002) suggest that the youngest, coldest cores may be more extended, and gradually accrete material over time and then fragment into smaller cores. Alternative to being a precursor to active clump, the quiescent clump may just be forming lower mass stars due to the lower fraction of material at high densities.

2.4.6 A Young HII Region in the Active Clump

The quiescent clump shows no sign of radio continuum emission in either our VLA maps (3 σ continuum sensitivity of 0.6 mJy) or in the MAGPIS maps at 6 and 20 cm (White et al., 2005; Helfand et al., 2006). However, one continuum source is detected at (α, δ) = (282.404^o, -0.779^o), G32.03 + 0.05, in the active clump and appears to be interacting with the surrounding dense NH_3 gas. G32.03 + 0.05 is an extended source and we extracted peak and integrated flux densities (using the total of a 2-D Gaussian fit to the data) from the NH_3 data at 1.26 cm and from various epochs of the MAGPIS data at 6 and 20 cm (White et al., 2005; Helfand et al., 2006). Since this source is extended, the fluxes derived are highly sensitive to the largest angular scale of the observationAnderson et al. (2011) point out that MAGPIS source fluxes are often lower limits as there is a good deal of diffuse emission missed. This source appears to be extended enough that

a significant portion of the total flux is lost on the largest angular scales by the filtering function of the interferometer.

While we attempted to fit the three data points with the most closely matched resolutions (our 3″ 1 cm data at 23 mJy, the MAGPIS Epoch 1 5″ 6 cm data at 19 mJy, and the 6″ 20 cm data at 32 mJy) to a thermal bremsstrahlung spectrum, the uncertainties between the epochs and varying levels of recovered fluxes provide only a moderate constraint. G32.03 + 0.05 has confirmed radio recombination lines from Anderson et al. (2011) at 91 km s^{-1} consistent with being associated with the surrounding NH_3 gas. The continuum source is also associated with 8 and 24 μm extended emission. Additionally, in, e.g., Figure 2.2(b) we see morphological evidence that the continuum source has carved a bubble in the dense gas. Despite the inconclusive thermal bremsstrahlung spectral fit, we conclude that this source is a young HII region of a massive star interacting with the surrounding dense gas. From the relatively flat spectrum from 1 cm to 6 cm to 20 cm, we assume a turnover frequency (where the source becomes optically thick) at our longest observed wavelength, 20 cm. A turnover at a longer (shorter) wavelength results in a lower (higher) emission measure and a later (earlier) spectral type.

Using the Strömgren sphere approximation, we calculate the number of ionizing photons produced by this HII region and its main-sequence spectral type assuming that the turnover frequency occurs at 20 cm. Our calculation of the number of ionizing photons per second produced by this HII region (given in the Appendix §2.4.7) gives Q = $10^{47.8}$ s^{-1}, which corresponds to a spectral type B0.5 (Vacca et al., 1996).

2.4.7 HII Region Spectral Type Identification

We approximate the number of ionizing photons produced in the HII region G32.03+0.05 using the Strömgren sphere approximation. The Strömgren sphere approximation assumes that the HII region is spherical, in equilibrium, that there is one electron per ion, and that each energetic

photon ionizes one atom. We calculate the radius of the HII region using the expression

$$\mathrm{r} = \left[\frac{\mathrm{S}_\nu \mathrm{c}^2}{2\nu^2 \mathrm{k} \mathrm{T_e}} 4\mathrm{D}^2\right]^{1/2} \tag{2.3}$$

from which we derive a radius of 0.08 pc at 20 cm. This matches our empirical Gaussian fit to the source, which gives a source radius of 0.1 pc. In the expression above, S_ν is the flux density, ν is the observed frequency, T_e is the electron temperature which we take to be 8000 K, and D is the distance which we assume to be 5.5 kpc. Assuming that the source becomes optically thick at our longest observed wavelength where the spectrum appears relatively flat, $\lambda = 20$ cm, we can derive an emission measure using the expression (from, e.g., Wood & Churchwell, 1989)

$$\mathrm{EM[pc\ cm^{-6}]} = \frac{\tau_\nu}{8.235 \times 10^{-2} \left(\frac{\mathrm{T_e}}{\mathrm{K}}\right)^{-1.35} \left(\frac{\nu}{\mathrm{GHz}}\right)^{-2.1} a(\nu, \mathrm{T_e})} \tag{2.4}$$

where ν is the turnover frequency, where τ=1, which we take to be 1.5 GHz (20 cm) and a(ν, T_e) is a correction factor of order unity. We can then calculate the number density of electrons using the expression

$$\mathrm{n_e} = \sqrt{\frac{\mathrm{EM}}{2\mathrm{r}}} \tag{2.5}$$

and assume that this equals the number density of ions. The number of Lyman continuum photons is given by the Strömgren sphere equation,

$$\mathrm{Q} = \frac{4}{3}\pi \mathrm{r}^3 \alpha_B \mathrm{n}_e^2 \tag{2.6}$$

where α_B is the case B recombination rate coefficient, 3.1×10^{-13} cm^3 s^{-1} for $\mathrm{T}_e = 8000$ K. We derive 6.4×10^{47} Lyman continuum ionizing photons per second, which corresponds to a spectral type of B0.5 (Vacca et al., 1996).

2.5 The Commonality of Physical Conditions in Massive Star-Forming Regions

The body of work observing pre- and star-forming clumps and characterizing their physical properties have led us to understand some common conditions. Together, existing high-resolution

observations of massive star-forming regions show some common physical structure and properties of massive star-forming regions. However, the extent of the innate similarities and differences between the observed regions are difficult to distinguish from differences in observing mode, resolution, or large-scale environment. We place the current work in context by comparing with observations from the literature below and find some common features.

Massive star-forming regions show clumpy filamentary structure on about 1 pc scales containing about 10^3 $M_\odot$ of total mass (e.g Wang et al., 2008; Pillai et al., 2011; Fontani et al., 2012; Liu et al., 2012; Galván-Madrid et al., 2010; Carrasco-González et al., 2010). Embedded within this filamentary structure are complexes of dense cores. These cores are separated by about 0.1 pc (e.g., Rathborne et al., 2008; Pillai et al., 2011; Fontani et al., 2012; Devine et al., 2011), but higher resolution observations show further fragmentation, down to core separations of $\sim$0.01 pc (e.g., Galván-Madrid et al., 2010). The fragmentation scales observed are larger than the thermal Jeans Length (e.g Pillai et al., 2011) implying the importance of turbulence in the fragmentation process.

Embedded within these complexes strung along pc-scale filaments are dense cores with masses of order 10-100 $M_\odot$(e.g., Pillai et al., 2011; Liu et al., 2012; Brogan et al., 2009; Zhang et al., 2009) and sizes of less than 0.007 pc at the highest resolution (e.g Brogan et al., 2009) and around 0.1 pc at more moderate resolution (e.g., Devine et al., 2011; Wang et al., 2007; Rathborne et al., 2008). Observations of the dense cores in massive star-forming regions give typical peak column densities of $N(H_2) \approx 5\times10^{23}$ cm^{-2} (e.g., Zhang & Wang, 2011; Rathborne et al., 2008; Devine et al., 2011; Wang et al., 2007) and up to 1×10^{24} cm^{-2} at the highest resolution (Brogan et al., 2009).

We find that pre-star-forming cores and filaments are characterized by smoothly varying temperatures of about 10-20 K (e.g., Zhang et al., 2009; Zhang & Wang, 2011; Rathborne et al., 2008; Pillai et al., 2011; Ragan et al., 2011; Devine et al., 2011). Interestingly, the pre-star-forming cores and filaments show very little structure in the temperature and no temperature gradients toward the cores. Star-forming cores are uniformly warmer, about 40 K in this study and Zhang & Wang (2011), but can be higher than 100 K when measured using higher excitation transitions

of ammonia (e.g., Beuther et al., 2007a, 2009). The massive star-forming region observed in this work shows two distinct kinematic components within the pc-scale filament. A similar structure is also observed by Devine et al. (2011), Galván-Madrid et al. (2010), and Carrasco-González et al. (2010).

While there are common masses and radii for cores identified in the literature, it is not clear at this point whether this corresponds to a common physical scale or simply a common observationally preferred scale. While our NH_3 VLA observations have the potential to address this question over several clumps and core complexes, our observations still only cover one IRDC. A systematic study of many regions would be required to understand the innate similarities and differences between the regions (similar to the fragmentation analysis presented by Palau et al., 2013).

An interesting feature in this work found elsewhere in the literature is the trend that the coldest cores are more extended (see Figure 2.10 and e.g., Zhang & Wang, 2011; Li et al., 2013; Rathborne et al., 2008; Pillai et al., 2011). Since we model both the temperature and column density, this steepening in the column density profile with evolutionary stage is not a temperature effect. Making the reasonable assumption that the coldest cores evolve over time to become more like the warmer cores suggests that massive star-forming cores begin larger and more extended, and gradually collapse and accrete material over time, quickly forming stars once the dense cores have formed. This is consistent with the shallower intensity profiles observed in pre-star-forming clumps as seen in Beuther et al. (2002). As the cores undergo internal collapse, their density profile steepens, and the dense cores quickly form stars. An alternative explanation is that the difference in density profiles is due to the clumps eventual fate - a cluster containing massive stars or a clustered low-mass star forming region (Bontemps et al., 2010).

2.6 Conclusion

We investigate the high-resolution ($\sim$0.1 pc) temperature and density structure of different evolutionary phases within a single IRDC, allowing us to disentangle the effect of evolution from observational biases introduced by distance, Galactic-scale abundance variations, and large-scale

environment. We observed two regions of the IRDC G32.03 + 0.05 with the (1,1), (2,2), and (4,4) inversion transitions of NH_3 on the VLA and derived temperatures and column densities, average velocities, and velocity dispersions using a radiative transfer model. The observed properties are compared with the literature to explore the range of physical conditions observed in massive star-forming regions.

- ***Temperature Structure:*** The temperature structure in the pre-star-forming cores and filaments is very smooth, varying from about 10 to 20 K. The filaments show no gradient toward the cold cores, except Core 7 in the active clump which shows a temperature gradient from 20 K to 15 K. There is a slight gradient from high to low temperature from the filament exterior to its interior. The pockets of active star formation (the hot core complex, especially Core 2 in the active clump) show an increase in the temperature, to about 35-40 K.

- ***Column Density Structure and the Evolution of Massive Star-Forming Clumps:*** Both clumps show core sub-structuring, but of very different kinds. The quiescent clump contains a smooth, extended central core at the hub of the filaments. This core is over 0.2 pc in diameter, cold, with a peak surface density of about 0.5 g cm^{-2}. This core shows no signs of active star formation (Stage 1; Battersby et al., 2010) and may represent an early stage in massive star formation. The active clump shows three complexes of compact, dense cores near the predicted 1 g cm^{-2} threshold for massive star formation. These three complexes show very similar density structures (similar core sizes, separations, and peak surface densities). However, the hot core complex is in Stage 3 (Battersby et al., 2010) and appears to be actively forming massive stars, while the dark core complexes are in Stage 2 (Battersby et al., 2010), showing the signs of early, embedded massive star formation (8 μm dark and cold, with 6.7 GHz CH_3OH maser emission). Abutting the dark core complex to the south is a young UCHII region (Stage 4; Battersby et al., 2010) which has carved a bubble in the NH_3 gas.

Given the similarity of the column density structures observed, we hypothesize that we are seeing core complexes in slightly different evolutionary stages, from the Stage 2 dark core complexes to the Stage 3 hot core complex to the Stage 4 young UCHII Region. Whether or not the Stage 1 extended cold core observed in the quiescent clump represents the precursor to the dark core complexes remains an open question. There is additional support in the literature that cold cores are generally more extended and less massive, implicating the process of global collapse and accretion in the formation process of dark core complexes, but a conclusive answer would require a larger-scale systematic study.

- ***Common Conditions for Massive Star Formation:*** We compare our results with previous work in the literature and uncover some common conditions for the formation of massive stars. We find clumpy filamentary structure on $\sim$1 pc scales with massive cores, extended (>0.1 pc) in the earliest phase and compact (<0.1 pc) in later stages. Commonly derived fragmentation scales are larger than the thermal Jeans lengths, indicating that turbulence is important in the fragmentation process in these cores. The onset of massive star formation disrupts filamentary structure. The pre-star-forming filament and cores show little temperature variation and average about 10-20 K, while the star-forming cores peak near 40 K.

The observations presented allow us to investigate the role of evolution independently of Galactic-scale abundance variations, distance/resolution and large-scale environmental effects toward one IRDC showing different evolutionary stages. We identify common conditions observed toward massive star-forming regions and discuss how these physical structures may evolve with time. In Chapter 4, we derive the abundance, compare gas and dust properties, and discuss the origin of millimeter continuum emission. In the following paper (Battersby et al., 2013), we discuss the dynamics, virial parameters, and large-scale environment of this massive star forming region.

Chapter 3

Characterizing Precursors to Stellar Clusters with Herschel

Despite their profound effect on the universe, the formation mechanism of massive stars and stellar clusters remains elusive. Recent advances in observing facilities and computing power have brought us closer to understanding this formation process. In the past decade, evidence has emerged that suggests Infrared Dark Clouds (IRDCs) may be precursors to stellar clusters. However, the usual method for identifying IRDCs is biased by the requirement that they are seen in absorption against background mid-IR emission, whereas dust continuum observations allow cold, dense pre-stellar-clusters to be identified anywhere. We aim to understand what dust temperatures and column densities characterize and distinguish IRDCs, to explore the population of dust continuum sources that are not IRDCs, and to roughly characterize the level of star formation activity in these dust continuum sources. We use Hi-GAL (Herschel Infrared Galactic Plane Survey; Molinari et al. 2010) 70 to 500 μm data to identify dust continuum sources in the ℓ=30° and ℓ=59° Hi-GAL Science Demonstration Phase (SDP) fields, to characterize and subtract the Galactic cirrus emission, and perform pixel-by-pixel modified blackbody fits on cirrus-subtracted Hi-GAL sources. We utilize archival Spitzer data to indicate the level of star-forming activity in each pixel, from mid-IR-dark to mid-IR-bright. We present temperature and column density maps in the Hi-GAL ℓ=30° and ℓ=59° SDP fields, as well as a robust algorithm for cirrus subtraction and source identification using Hi-GAL data. We report on the fraction of Hi-GAL source pixels which are mid-IR-dark, mid-IR-neutral, or mid-IR-bright in both fields. We find significant trends in column density and temperature between mid-IR-dark and mid-IR-bright pixels; mid-IR-dark pixels are about 10 K

colder and have a factor of 2 higher column density on average than mid-IR-bright pixels. We find that Hi-GAL dust continuum sources span a range of evolutionary states from pre- to star-forming, and that warmer sources are associated with more star formation tracers. Additionally, there is a trend of increasing temperature with tracer type from mid-IR-dark at the coldest, to outflow/maser sources in the middle, and finally to 8 and 24 μm bright sources at the warmest. Finally, we identify five candidate IRDC-like sources at the far kinematic distance in the Galaxy. These are cold ($\sim$ 20 K), high column density ($N(H_2) > 10^{22}$ cm^{-2}) clouds identified with Hi-GAL which, despite bright surrounding mid-IR emission, show little to no absorption at 8 μm. These are the first inner Galaxy far side candidate IRDCs of which the authors are aware.

3.1 Introduction

Massive stars play a dominant role in shaping the Universe through their immense ionizing radiation, winds, and spectacular explosive death, yet their formation mechanism remains poorly understood. The dominant mode of star formation, and perhaps the only mode for massive star formation seems to be clustered (Lada & Lada 2003; de Wit et al. 2005). The definition of clustered can be called into question (e.g. Bressert et al. 2010; Gieles & Portegies Zwart 2011), but the search for young, massive star forming regions is still directed toward 'proto-clusters:' cold, dense, massive molecular clumps. Galactic embedded clusters are characterized by high densities (n $\sim$ 10^4-10^7 cm^{-3}), radii of about 0.5-1 pc, temperatures of about 50-200 K, and masses around 10^2-10^3 M$_\odot$(Lada & Lada 2003; Motte et al. 2003). Proto-clusters represent a slightly earlier stage, before star formation has commenced, and so we expect the properties to be similar to those of the embedded clusters except that proto-clusters ought to be colder. We are most interested in searching for the more massive proto-clusters where massive stars may be forming, with M $\gtrsim$ 100 M$_\odot$. Direct observation of proto-clusters is complicated: they are rare, and therefore farther away on average than isolated low mass star-forming regions, proto-clusters have high column densities, meaning that the proto-stars are highly embedded, and massive stars evolve rapidly and quickly heat and ionize their surroundings, disrupting their natal molecular cloud.

Searches for proto-clusters or massive proto-stars are usually targeted at long-wavelengths, as dust continuum emission from these cold, dense sources peaks in the far-IR to sub-mm. Surveys of molecular lines are another approach for identifying potential proto-clusters, although these surveys may be time-intensive and interpreting molecular line spectra is complicated by excitation conditions and optical depth. The discovery of Infrared Dark Clouds (IRDCs, Egan et al. 1998; Perault et al. 1996; Omont et al. 2003), opened a new window to viewing these cold, dense potential proto-clusters in silhouette against the bright Galactic mid-IR background. In the past decade, compelling evidence has emerged that suggests that some IRDCs may be precursors to massive stars and clusters (e.g. Rathborne et al. 2006; Ragan et al. 2006; Beuther & Sridharan 2007; Parsons et al. 2009; Battersby et al. 2010). While there exist many small IRDCs (e.g. Peretto & Fuller 2010; Kauffmann & Pillai 2010), the most massive ones (M $\sim 10^{3-4}$ $M_{\odot}$, $n_H > 10^5$ cm^{-3}, T < 25 K, Rathborne et al. 2006; Egan et al. 1998; Carey et al. 1998) are consistent with expectations for a proto-cluster. However, the identification of an IRDC requires that it be on the near side of a bright mid-IR background. This limits our potential to understand the Galactic distribution of potential proto-clusters.

Far-IR and submm dust continuum surveys are a powerful way to identify proto-clusters throughout the Galaxy, as the cold, dense dust is optically thin at these wavelengths. Surveys such as the Bolocam Galactic Plane Survey (BGPS; Aguirre et al. 2011) at 1.1 mm, the APEX Telescope Large Area Survey of the Galaxy (ATLASGAL, Schuller et al. 2009) at 870 μm, and now Hi-GAL (The Herschel Infrared Galactic Plane Survey; Molinari et al. 2010) from 70 to 500 μm are promising tools for understanding star cluster formation on a Galactic scale. However, the sources identified in these surveys may span a large range of evolutionary states, from pre-star-forming to star-forming, and further analysis or intercomparison may be necessary to identify the pre-star-forming regions. Since dust temperatures and column densities can be derived from the multi-wavelength Hi-GAL data, this data set allows for the distinction to be made between pre- and star-forming regions.

For this study, we utilize data from the Hi-GAL survey (Molinari et al. 2010) from 70 to 500

μm in the ℓ=30° and ℓ=59° SDP fields to characterize dust continuum sources. We investigate differences in the physical properties of mid-IR-dark and mid-IR-bright clouds identified in the dust continuum, and also the physical properties of sources associated with various star formation tracers. We use Extended Green Objects (EGOs, also known as "green fuzzies", Cyganowski et al. 2008; Chambers et al. 2009) to trace outflows from young stars, CH_3OH masers to trace sites of massive star formation, and 8 and 24 μm emission to indicate an accreting proto-star or UCHII Region (Battersby et al. 2010).

This chapter is organized as follows. In Section 3.2 we introduce the Hi-GAL observing strategy and discuss archival data used in our analysis. In Section 3.3 we describe the Galactic cirrus emission removal and source identification methods, the modified blackbody fitting procedure, and how the star formation tracers were incorporated. Section 3.4 describes our results, including a discussion of uncertainties, the properties of the cirrus cloud emission, the temperature and column density maps, the association of Hi-GAL sources with mid-IR-dark and mid-IR-bright sources, and star formation tracers in Hi-GAL sources. In Section 3.5 we present five candidate IRDC-like clouds on the far side of the Galaxy, and finally, in Section 3.6 we summarize our conclusions.

3.2 Observations and Archival Data

3.2.1 Hi-GAL

The Herschel Infrared Galactic Plane Survey, Hi-GAL (Molinari et al. 2010), is an Open Time Key Project of the Herschel Space Observatory (Pilbratt et al. 2010). Hi-GAL will perform a 5-band photometric survey of the Galactic Plane in a $|b| \leq 1°$ -wide strip from -70° $\leq \ell \leq$ 70° at 70, 160, 250, 350, and 500 μm using the PACS (Photodector Array Camera and Spectrometer, Poglitsch et al. 2010) and SPIRE (Spectral and Photometric Imaging Receiver, Griffin et al. 2010) imaging cameras in parallel mode. Two 2° × 2° regions of the Hi-GAL survey were completed during the Science Demonstration Phase (SDP; Molinari et al. 2010), centered at approximately $[\ell,b]$ = [30°, 0°] and [59°, 0°].

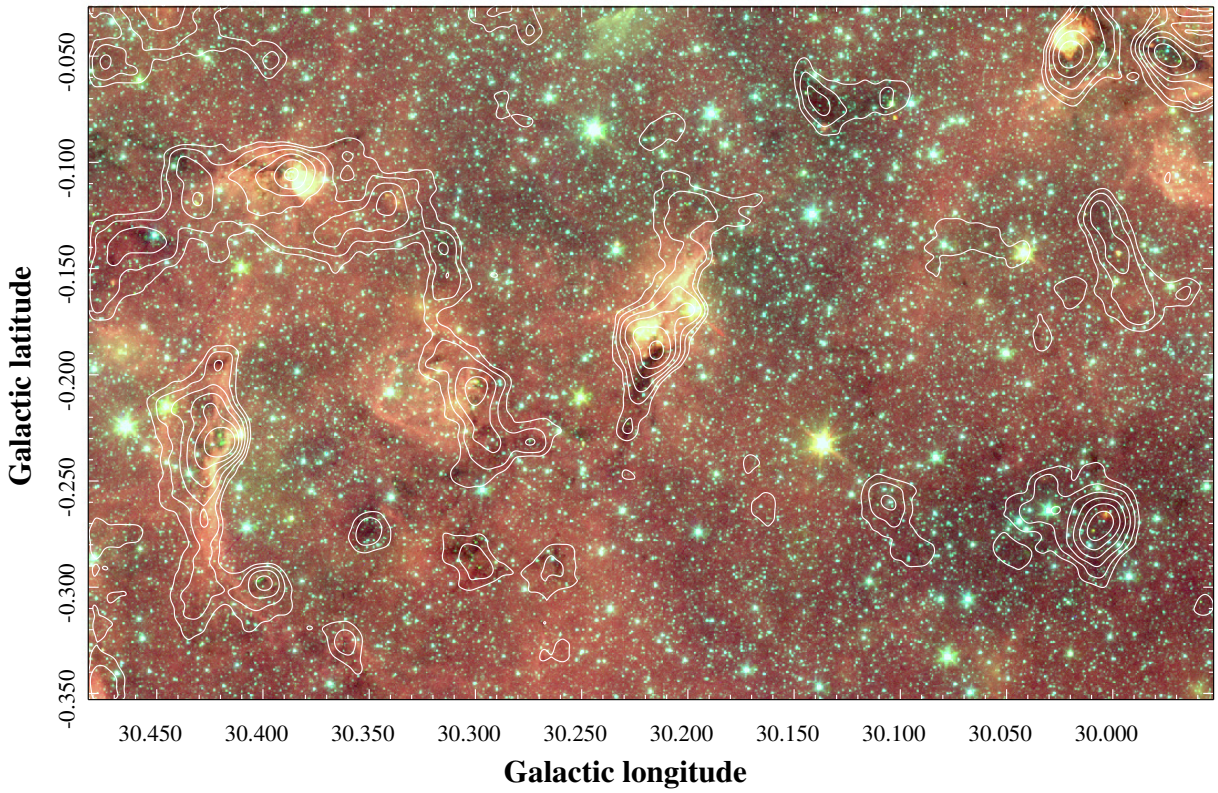

Figure 3.1: A three-color GLIMPSE image with logarithmic BGPS 1.1 mm dust continuum contours (from 90 mJy to 0.8 Jy) on our test region in the Hi-GAL SDP ℓ=30° field. Red: 8 μm , Green: 4.5 μm , and Blue: 3.6 μm. This figure demonstrates the distinction between the IRDC and dust continuum population. Some dust continuum sources are mid-IR-bright, some are mid-IR-dark, and some have no IR correlation. The object in the center is particularly well-suited as a test case for this study as it contains both mid-IR-bright and mid-IR-dark dust continuum sources radiating as filaments on either side of a young HII region complex.

Data reduction was carried out using the *Herschel* Interactive Processing Environment (HIPE, Ott 2010) with custom reduction scripts that deviated considerably from the standard processing for PACS (Poglitsch et al. 2010), and to a lesser extent for SPIRE (Griffin et al. 2010). A detailed description of the entire data reduction procedure can be found in Traficante et al. (2011).

The zero-level offsets in the Herschel maps were established by comparison with the IRAS and Planck data at comparable wavelengths, following the same procedure as described in Bernard et al. (2010). We compared the Herschel-SPIRE and PACS data with the predictions of a model provided by the Planck collaboration (Planck Core-Team, private communication) and constrained on the Planck and IRIS data (Miville-Deschênes & Lagache 2005). The model uses the all-sky dust temperature maps derived from the IRAS 100 μm and the two highest Planck frequencies to infer the average radiation field intensity for each pixel at the common resolution of the Planck and IRAS resolution of $5'$. The Dustem model (Compiègne et al. 2010) with the above value for the radiation field intensity was then used to predict the expected brightness in the Herschel-SPIRE and PACS bands, using the nearest available Planck or IRAS band for normalization and taking into account the appropriate color correction in the Herschel filters. The predicted brightness was correlated with the observed maps smoothed to the $5'$ resolution over the region observed with Herschel and the offsets were derived from the zero intercept of the correlation. We estimate the accuracy of the offset determination to better than 5%.

3.2.2 Archival Data

We utilize the wealth of archival data in the Galactic Plane for our analysis. We use the mid-IR data taken as part of the Galactic Legacy Infrared Mid-Plane Survey Extraordinaire (GLIMPSE; 3.6, 4.5, 5.8, and 8.0 μm, Benjamin et al. 2003) and the MIPSGAL survey (24 μm; Carey et al. 2009). We also make use of the IRDC catalog of Peretto & Fuller (2009), the catalog of Extended Green Objects (Cyganowski et al. 2008, EGOs;), and the 1.1 mm data and catalog from the Bolocam Galactic Plane Survey (BGPS; Aguirre et al. 2011; Rosolowsky et al. 2010). The Multi-Array Galactic Plane Imaging Survey (MAGPIS; Helfand et al. 2006; White et al. 2005), which

provides comprehensive radio continuum maps of the first Galactic quadrant at high resolution and sensitivity, is also used in our analysis.

3.3 Methods

3.3.1 Source Definition and Removal of the Galactic Cirrus

The Hi-GAL data reveal a wealth of structure in the Galactic Plane, from cirrus clouds (Martin et al. 2010) to filaments and clumps, as discussed in Molinari et al. (2010). Figure 3.1 demonstrates the complicated association of mid-IR and dust continuum sources toward the Galactic Ring. In this chapter, we explore the physical properties of the densest components of the Galactic Plane; the potential precursors to massive stars and clusters. In order to properly characterize these dense objects, a careful removal of the Galactic cirrus is required. We have explored a variety of methods for the removal of the cirrus emission and we briefly discuss the pros, cons, and systematic effects of the different subtraction methods. We discuss the first four methods attempted, and finally the fifth and final method used.

3.3.1.1 Methods Tested for Source Identification

Our first step is to project all the data onto a common grid, with a common resolution and common units for comparison. We crop the images to the useable science field, convert the data to units of MJy/sr, Gaussian convolve to a common resolution ($36''$ and $25''$ for the lower and higher resolution modified blackbody fits), and regrid to a common grid with a reasonable pixel size (roughly 1/4 the beam size, Θ_{FWHM}). These images are used in the remainder of the analysis. We include images throughout the chapter of a "test field," (approximately, $[\ell,b]$ = [29.95, -0.35] to [30.50, 0]) chosen for its diversity of mid-IR-bright and mid-IR-dark sources. The analysis was orginally run and optimized on this region and then expanded to the full Hi-GAL fields.

The first method for determining the dense clump source masks was to use Bolocat clump masks derived from the Bolocam Galactic Plane Survey (BGPS; Aguirre et al. 2011; Rosolowsky

et al. 2010) at 1.1 mm. While these masks are a robust tracer of the cold, dense gas, they only extend to $|b| \leq 0.5^\circ$ in the majority of our science field and the sensitivity in the ℓ=59° field is too poor to trace the clumps seen in Hi-GAL.

The following methods all use the SPIRE 500 μm data to determine the source masks, as the cirrus decreases towards longer wavelengths (Gautier et al. 1992) and Peretto et al. (2010) demonstrate that the SPIRE 500 μm data is well-suited for cirrus/dense source distinction. The second method we tried was based on that of Peretto et al. (2010), who found that toward IRDCs, the SPIRE 500 μm flux distribution showed a clear peak at low fluxes with a long tail toward higher fluxes. While this method works well when applied to a single IRDC, as it was used in Peretto et al. (2010), it is not robust enough to be used to create a full Galactic cirrus emission map from high ($|b| \gtrsim 1^\circ$) to low ($|b| = 0^\circ$) Galactic latitudes. We then tried a third method to create the dense source masks using a simple contrast map (contrast = data - background) of the SPIRE 500 μm data and applied a cutoff. This method improved over the previous, however, it suffered from large negative bowls, creating source masks that were much smaller than the physical source sizes. In the fourth method, we define the background first by a second-order polynomial plane fit (along Galactic latitude) to the smoothed 500 μm image. This plane fit to the Galactic cirrus was then subtracted from the original data and a cutoff was applied (determined by eye) to define the dense source masks. This was the first method to do a reasonable job of identifying sources in a range of Galactic latitudes. We found, however, that a polynomial plane was not a very good approximation to the shape of the Galactic cirrus emission, and that the fit was particularly poor at high Galactic latitudes ($|b| \sim 0.8 - 1^\circ$).

3.3.1.2 Final Adopted Method for Source Identification and Cirrus Removal

Figure 3.2 depicts the final method used to identify the dense sources and to separate those from the cirrus cloud emission. The first panel (a) shows the original SPIRE 500 μm image. The first step (shown in panel b) is to convolve the 500 μm image with a Gaussian that is large enough to smooth over the sources but small enough to capture variations in the cirrus emission. We decided

through trial and error that a Gaussian with a FWHM of 12′ was a reasonable compromise. We then fit a Gaussian in latitude to each Galactic longitude, as shown in Figure 3.3 and in panel (c) of Figure 3.2. A Gaussian in latitude is a reasonable approximation for the variation in the Galactic cirrus across the Galactic Plane and worked to identify sources at high and low Galactic latitudes equally well. We then subtract the Gaussian fit approximation of the Galactic cirrus from the original 500 μm data to achieve a "difference image." This "difference image" is the first guess at the cirrus-subtracted source map.

We apply a cutoff to this first guess cirrus-subtracted source map, such that everything above the cutoff is considered 'source.' We determine this cutoff by fitting a Gaussian to the histogram of pixel values (as shown in Figure 3.4). The negative flux values in the distribution of this "difference image" are representative of the random fluctuations in the data, so we mirror the negative flux values about zero, fit a Gaussian to that distribution (representative of the noise in the map) and then apply a cutoff of 4.25 σ to the "difference image." We calculated this cutoff in quarter σ intervals from 3 to 6 σ, a range over which it grows smoothly. The choice of 4.25 σ was selected because that cutoff best represented the sources in both the ℓ=30° and ℓ=59° fields when inspected by eye. While the choice of cutoff is important in determining the final physical properties, there is nothing special about this cutoff; the properties vary smoothly above and below this value.

Once the source cutoff has been selected, the sources are masked out in the original 500 μm image (as shown in solid white in panel (d) of Figure 3.2) and we convolve (with a Gaussian of FWHM 12′) the data outside the source masks, the cirrus emission, treating data in the source masks as missing. This creates a second guess at the cirrus emission, equivalent to panel (b). We then repeat the process of fitting a Gaussian in latitude to this image (as in panel (c)), determining a source cutoff by fitting a Gaussian to the mirrored negative flux distribution in the "difference image," applying these masks (panel (d)), and convolving around the masks (panel (e)) to produce the next guess at the cirrus emission (panel (b)). We iterate on this process until the source masks converge. Figure 3.5 shows the convergence of the source cutoff in both fields. We chose iteration 16 as the final source mask cutoff as it was representative of the converged value around which the

iterations varied, though the exact choice does not matter much, as the cutoff varies very little after iteration 10 in both fields. In panel (d) of Figure 3.2 the white masks are the first iteration source masks and the white contour shows the final (16th) iteration source masks. Once the source masks are determined, they are applied to each wavelength image, and that image is convolved (with a Gaussian FWHM $12'$ and the mask pixels ignored) to create the cirrus image at that wavelength. Subtracting the cirrus image at each wavelength from the original data produces the source images used in the modified blackbody fits, while the smooth cirrus images are used for the modified blackbody fits to the cirrus emission.

The top panel of figure 3.3 shows a slice of 500 μm data through Galactic latitude. The final convolved background (dashed black line) represents the low-lying emission across Galactic latitude, including its asymmetry about b=0° . Notice in the bottom panel that the structure is flat across Galactic latitude and allows for the identification of the source near b=1° , demonstrating the success of the cirrus removal and source identification. The adopted method was the only of the five attempted which succeeded in identifying this source. The other methods failed to remove the cirrus emission at this high Galactic latitude sufficiently to allow identification of this source. Figure 3.4 shows that as the iterations converge, we move flux from negative bowls back to sources as positive features and the mirrored negative distribution then more closely resembles a Gaussian (the black line is the final Gaussian fit to iteration 16).

This method has been fine-tuned by eye to reproduce the significant structure picked out by a human, but is entirely automated and was run in the exact same way for both the ℓ=30° and ℓ=59° fields, despite their vast differences. We have found that this method faithfully identifies sources across the range of Galactic latitudes covered by the data and the range of source confusion and activity observed. The sensitivity of this method is dependent upon the final mask cutoff or confusion, rather than the sensitivity of Hi-GAL. For the ℓ=30° final mask cutoff of 65 MJy/sr, we are sensitive above the cirrus background to a column density of $N(H_2) = 2.9 \times 10^{21}$ cm^{-2} for 20 K dust or $N(H_2) = 9.7 \times 10^{20}$ cm^{-2} for 40 K dust. In the ℓ=59° field the final mask cutoff is about 24 MJy/sr, which gives a sensitivity above the cirrus background to a column density of $N(H_2)$ =

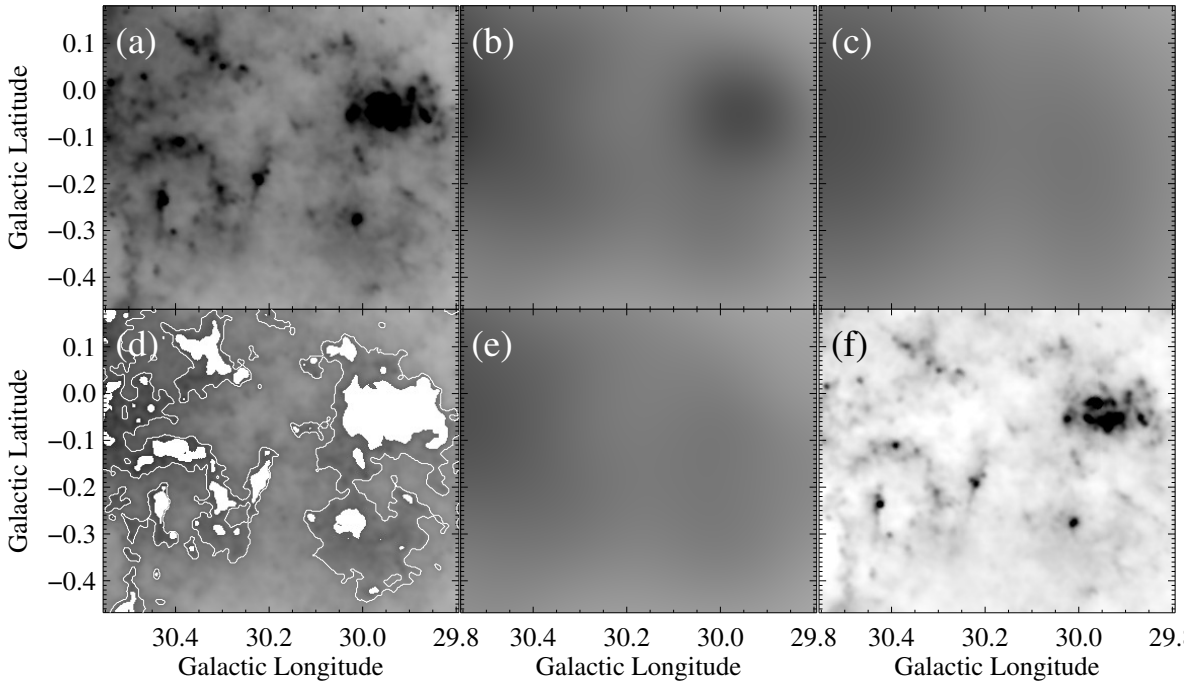

Figure 3.2: A depiction of the cirrus subtraction method for the first iteration. Panel (a) is the original SPIRE 500 μm image (all images on the same linear reverse grayscale, from -10 to 900 MJy/sr). Panel (b) is the smoothed SPIRE 500 μm image that is used to fit the Gaussian shown in panel (c). Panel (c) is then subtracted from panel (a) to produce a contrast image. A 4.25 σ cutoff is then applied to the contrast image to produce the source masks shown in panel (d). Panel (d) is the original SPIRE 500 μm image with the sources masked out in white. This is the first iteration source masks; the final source boundaries are shown as white contours. Panel (d) is then convolved with a Gaussian with the masks treated as missing data to produce panel (e). Panel (e) is considered the cirrus image for the next iteration. In the next iteration, a Gaussian will be fit to the cirrus image (e), as a function of latitude at each longitude, and steps b - e will repeat. Panel (f) is the difference image (original SPIRE 500 μm image (a) - convolved cirrus image (e)) that will eventually be used for greybody fitting in the final iteration.

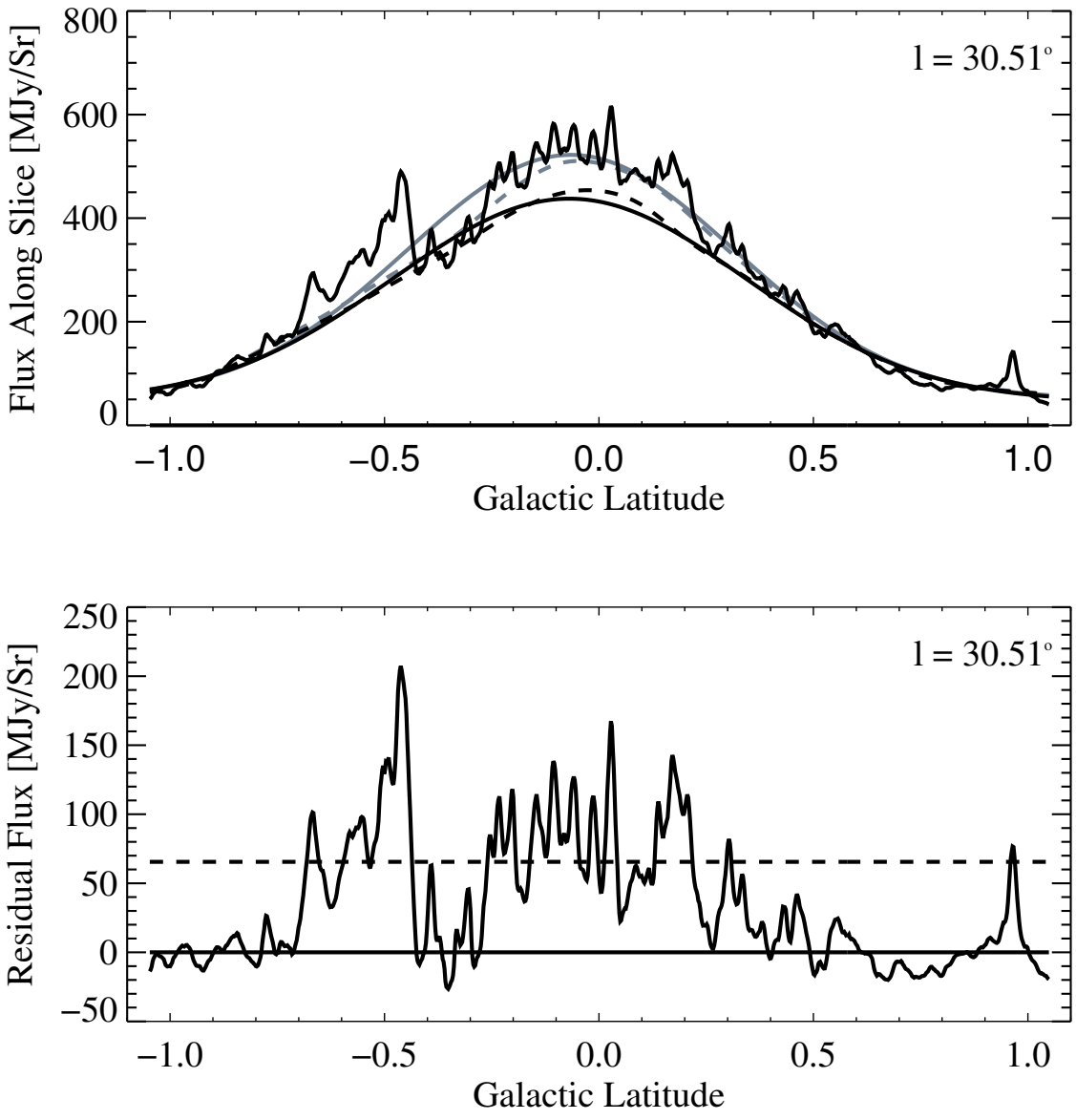

Figure 3.3: A slice across the Galactic Plane at $\ell = 30.51°$ of the SPIRE 500 μm image, demonstrating the cirrus emission removal method. The top panel shows the 500 μm data with the background fits (solid gray: first iteration Gaussian fit to the smoothed background, dashed gray: first iteration convolved background, solid black: same as gray, final iteration, dashed black: same as gray, final iteration). Note that the final background (dashed black line) fits the low-lying diffuse emission nicely, including its asymmetry about $b = 0°$. The bottom panel shows the final background subtracted science image cut along the same Galactic longitude, with the final source cutoff drawn as a dashed black line at 65 MJy/sr.

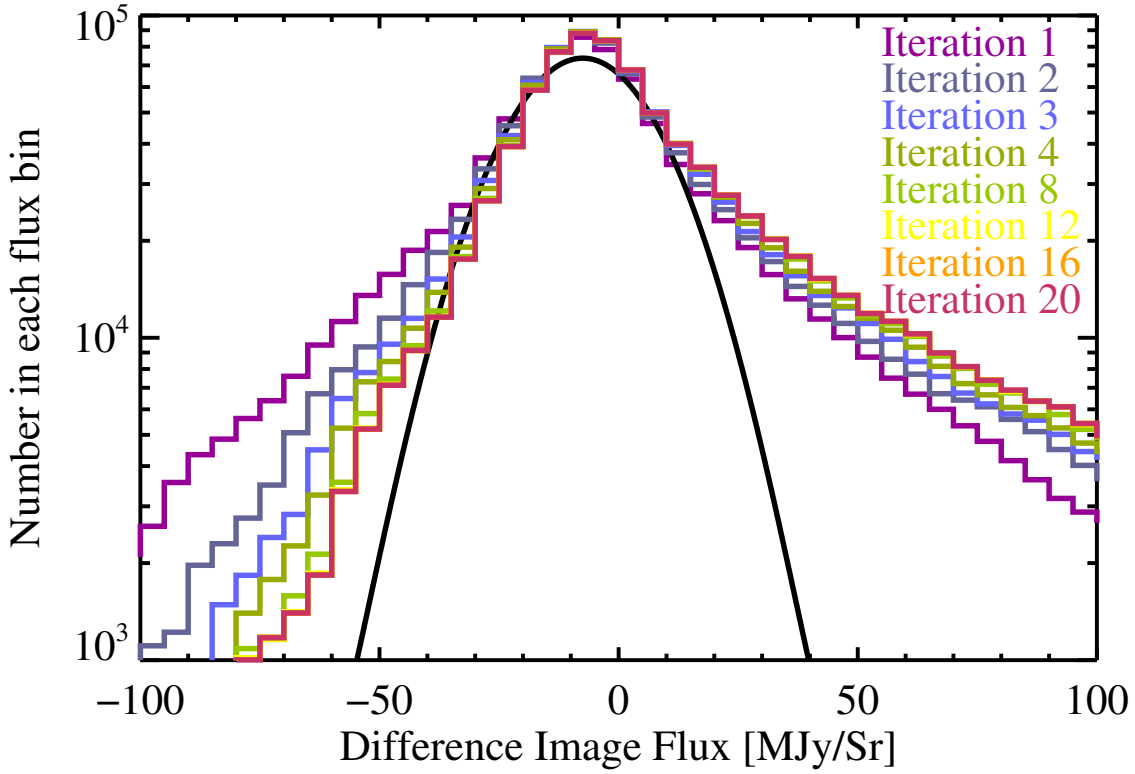

Figure 3.4: The flux distribution in the difference images (original 500 μm image - convolved cirrus image, e.g. Figure 3.2 panel (f)) for 8 iterations from 1 to 20 in the ℓ=30° field. In each iteration, the negative flux distribution was mirrored about 0 and a Gaussian was fit to the distribution to determine the characteristic fluctuations so that a source identification cutoff (of 4.25 σ) could be applied. Plotted here are the full distributions, not the mirrored distributions used to fit the Gaussian. As we iterate, points in the negative end are transferred to the positive end of the distribution as flux is restored in the negative bowls around bright sources. The Gaussian fit to the distribution for the final iteration (16) is shown as the black curve.

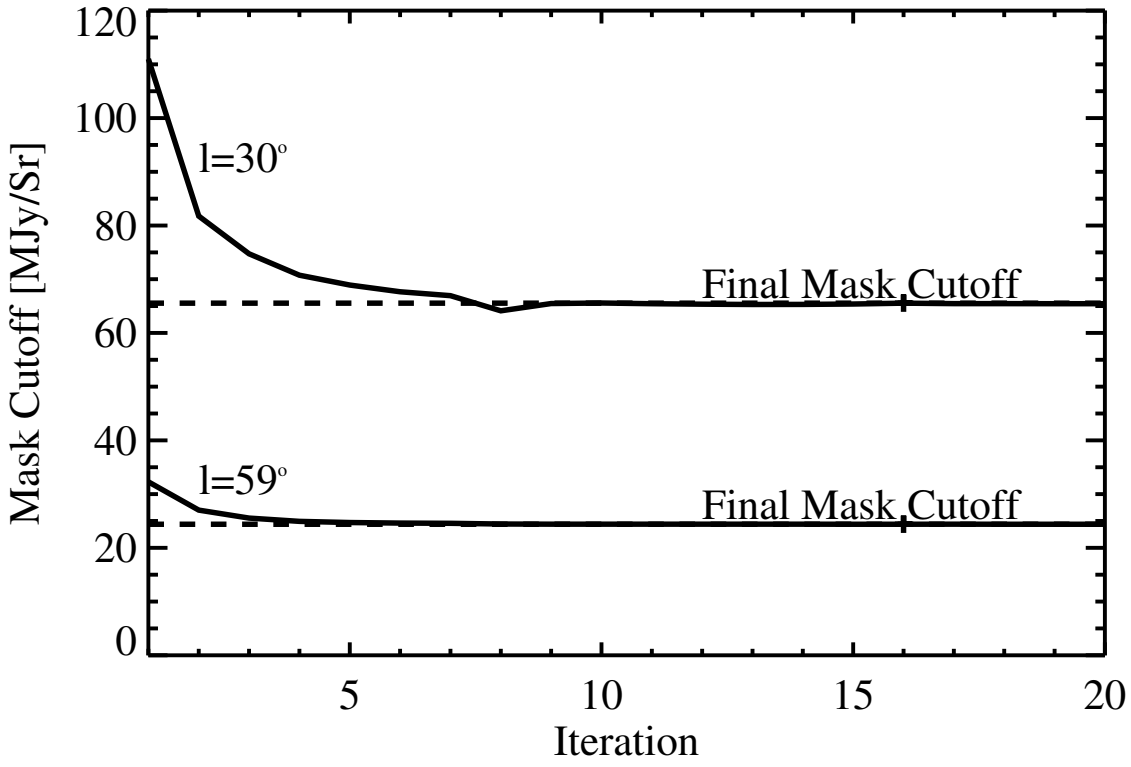

Figure 3.5: The 4.25 σ mask cutoff over 20 iterations. The cutoff is from the Gaussian fit (see Figure 3.4) to the flux distribution of points in the difference image. Both the ℓ=30° and ℓ=59° fields converge after several iterations, but to very different values.

1.1×10^{21} cm^{-2} for 20 K dust or N(H_2) = 3.6×10^{20} cm^{-2} for 40 K dust.

3.3.2 Modified Blackbody Fits

We performed pixel-by-pixel modified blackbody fits to both the cirrus cloud and the dense source clump emission. The cirrus emission fits were performed on the 36″ resolution images with all five Hi-GAL data points. β (the dust opacity spectral index) was allowed to vary as a free parameter. The dense source pixel-by-pixel fits were first performed on the images convolved to 36″ resolution. Following that, the results from the 36″ resolution tests were used as input to pixel-by-pixel fits performed on the images convolved to 25″ resolution. While the fits to the 25″ resolution images formally utilize less data points, they allow us to correlate the physical properties with star formation tracers on a smaller scale. We exclude the 500μm(36″ resolution) for the higher-resolution fit. The 70 μmpoint is also excluded because the optically thin assumption may not be valid (see Section 3.3.2.2 for more details). With only three data points for the fit, we fix β to a value of 1.75 (see Section 3.4.1 for details on how the results change if we instead assume a β of 1.5 or 2).

We use the modified blackbody expression in the form

$$S_\nu = \frac{2h\nu^3}{c^2(e^{\frac{h\nu}{kT}} - 1)}(1 - e^{-\tau_\nu}) \tag{3.1}$$

where

$$\tau_\nu = \mu_{\mathrm{H_2}} \mathrm{m_H} \kappa_\nu \mathrm{N(H_2)} \tag{3.2}$$

where μ_{H_2} is the mean molecular weight for which we adopt a value of $\mu_{H_2} = 2.8$ (Kauffmann et al. 2008), m_H is the mass of hydrogen, N(H_2) is the column density, and κ_ν is the dust opacity. We determine the dust opacity as a continuous function of frequency by fitting a power-law of the form $\kappa_\nu = \kappa_0(\frac{\nu}{\nu_0})^\beta$ to the tabulated Ossenkopf & Henning (1994) dust opacities in the relevant range of frequencies. We used the Ossenkopf & Henning (1994) MRN distribution with thin ice mantles that have coagulated at $n_H = 10^6$ cm^{-3} for 10^5 years model for dust opacity, which is a reasonable guess for these cold, dense clumps. We have assumed a gas to dust ratio of 100, which yielded a κ_0

value of 4.0 cm^2 g^{-1} (this includes the gas to dust ratio of 100) at ν_0 of 505 GHz (593.6 μm) with a $\beta = 1.75$.

3.3.2.1 Cirrus Emission Modified Blackbody Fits

We first fit a modified blackbody to each pixel in the cirrus image (e.g., Figure 3.2 panel (e)) using MPFITFUN (from the Markwardt IDL Libarary, Markwardt 2009). We assign a calibration uncertainty of 20% to the SPIRE and PACS data points and use the covariance matrix returned by MPFITFUN to estimate errors in the parameters. In the modified blackbody fit, we leave the column density, β, and the temperature as free parameters. The temperature was restricted to range between 0 and 100 K, the column density was free to range between 0 and 100 $\times$ 10^{22} cm^{-2}, and β from 1 to 3. We do not use the BGPS 1.1 mm point in the fits because uncertainties in both the absolute calibration and the spatial filter function prevent the BGPS point from significantly helping to constrain the fit at this time.

3.3.2.2 Dense Source Clump Modified Blackbody Fits

We then fit a modified blackbody at each position within the source masks of the cirrus-subtracted science images (e.g. Figure 3.2 panel (f)) to the dense clumps. For these fits of dense clumps, we ignore the 70 μm point since the optically thin assumption may not be valid ($\tau_{70\mu m} =$ 1 at N(H$_2$) = 1.2 $\times$ 10^{23} cm^{-2} using Equation 3.2). In fact, IRDCs often appear in absorption at 70 μm indicating that in these very high column density regimes, the 70 μm data is not optically thin and that it can no longer be modelled by a single dust temperature. Additionally, it has been found (e.g. Desert et al. 1990; Compiègne et al. 2010) that a large fraction of the flux at 70 μm is likely contaminated by emission from very small grains whose temperature fluctuations with time are not representative of the equilibrium temperature of the large grains. Without the 70 μm point we have only four points (usually just on the Rayleigh-Jeans slope) to constrain the fit, so we fix β to 1.75 (Ossenkopf & Henning 1994), and leave only the temperature and the column density as free parameters. We discuss how a value of β of 1.5 or 2 would alter the results in Section 3.4.1.

We acknowledge that perceived changes in temperature may actually be changes in β and discuss this more also in Section 3.4.1. We are, to an extent, looking for changes in the dust properties (β or temperature) across different environments, which we can still achieve.

These pixel-by-pixel modified blackbody fits to the cirrus-subtracted dense clumps were first performed on the images convolved to 36″ resolution. Following that, the results from the 36″ resolution tests were used as input to pixel-by-pixel fits performed on the images convolved to 25″ resolution. While the fits to the 25″ resolution images formally utilize fewer data points (the SPIRE 500 μm point must be excluded because of resolution), they allow us to correlate the physical properties with star formation tracers on a smaller scale. The physical properties returned by the fits at different resolutions agree well. The final temperature and column density maps (as shown in Figure 3.6) show the derived temperatures and column densities from the 25″ map within the source masks, and the smoothed cirrus-background temperatures and column densities outside the source masks.

We note here that star-forming regions contain structure on many scales, and that fitting a single temperature and column density over a region of 25″ (about 0.5 pc at a distance of 4 kpc) is a vast oversimplification. There certainly exist large variations in the temperature and column density in these sources on smaller scales. In this chapter, we present the beam-diluted average source properties on 25″ scales. The column densities presented here are therefore characteristic of the larger-scale clump structure and under-estimates of the peak column densities, while the temperatures will be underestimates in very hot regions (hot cores) and overestimates in very cold regions (starless IRDC cores).

3.3.3 Star Formation Tracer Label Maps

In order to robustly compare the physical properties determined in this chapter with various star formation tracers, we have created star formation tracer label maps. These maps are on the same grid as the science images (temperature, column density, etc.) and have a binary denotion in each pixel: 1 if the star formation tracer is present and 0 if it is not. We create star formation

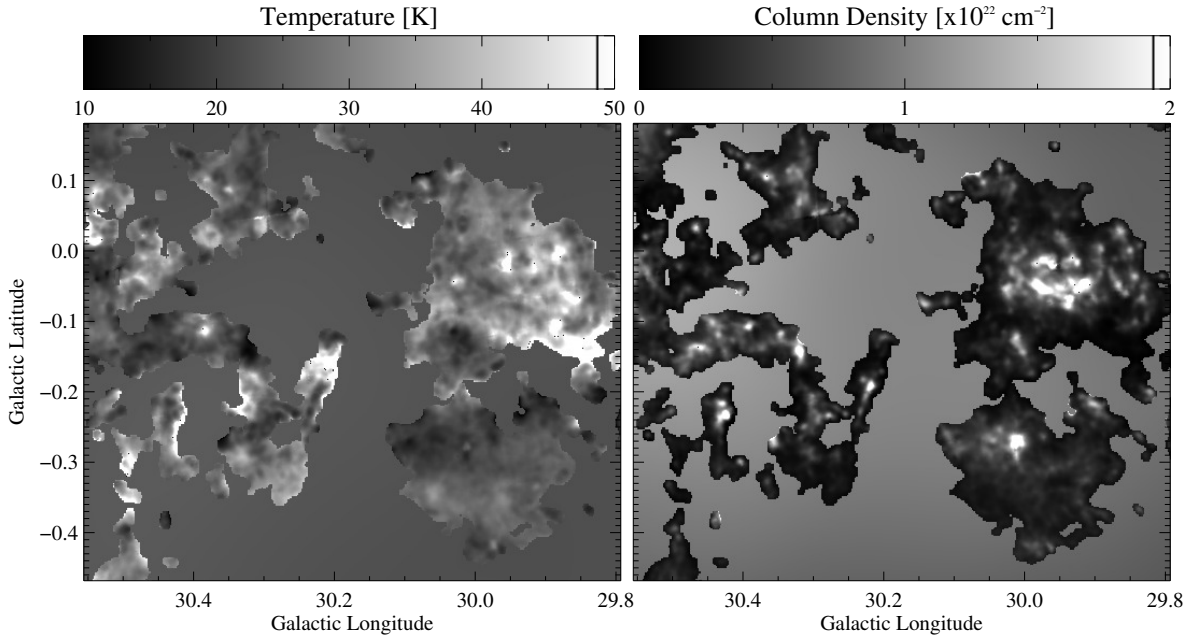

Figure 3.6: Temperature (left) and Column Density (right) maps in the ℓ=30° field test region. In these maps, the background cirrus emission temperature and column densities are plotted outside of the source masks, while the background-subtracted temperature and column densities are plotted inside the source masks. These maps are at 25″resolution and assume $\beta = 1.75$ inside the source masks.

tracer label maps for the MIPS 24 μm emission, 8 μm emission, Extended Green Objects (EGOs; Cyganowski et al. 2008; Chambers et al. 2009), and 6.7 GHz methanol maser emission (Pestalozzi et al. 2005). The MIPS 24 μm images required stitching together using MONTAGE before the label map could be created. Since the ℓ=30° field is more populated, we expect a wider range of star formation activity. This is, of course, assuming that the phase of star formation is generally random with location and that more regions will show a wider age distribution. For this reason, we choose to only perform the star formation tracer analysis on the ℓ=30° field. The 8 μm emission label maps, however, were created and analyzed for both the ℓ=30° and ℓ=59° fields so that we could understand the relationship between mid-IR and Hi-GAL sources in both fields (see Section 3.4.4).

3.3.3.1 GLIMPSE 8μm Emission/Absorption Label Map

The GLIMPSE 8 μm band shows emission from warm dust and Polycyclic Aromatic Hydrocarbons (PAHs). Regions with bright 8 μm emission may contain warm, diffuse dust or UV-excited PAH emission from an Ultra-Compact HII Region (Battersby et al. 2010). The absorption of 8 μm emission by an Infrared Dark Cloud (IRDC) indicates a high column of cold dust obscuring the bright mid-IR background. We note that mid-IR-bright regions generally indicate active star formation, and that the peak of mid-IR emission can be offset from the youngest regions of star formation (e.g. Beuther et al. 2007b). We denote regions of bright 8 μm emission as mid-IR-bright (mIRb), dark regions of absorption at 8 μm as mid-IR-dark (mIRd), and regions without strong emission or absorption at 8 μm as mid-IR-neutral (mIRn). The 8 μm emission label map has both a negative (IRDC, mIRd), positive (mIRb), and neutral (mIRn) component. This map is created by first making a contrast image. The GLIMPSE 8 μm image is convolved with a Gaussian of FWHM 5′ to represent the smooth, slowly varying background. 5′ was determined (see Peretto & Fuller 2009, for more details on this smoothing kernel choice) to be large enough to capture the largest IRDCs and mid-IR-bright objects, while still small enough to capture the background variations. This image is then subtracted from the original image, which is then divided by the

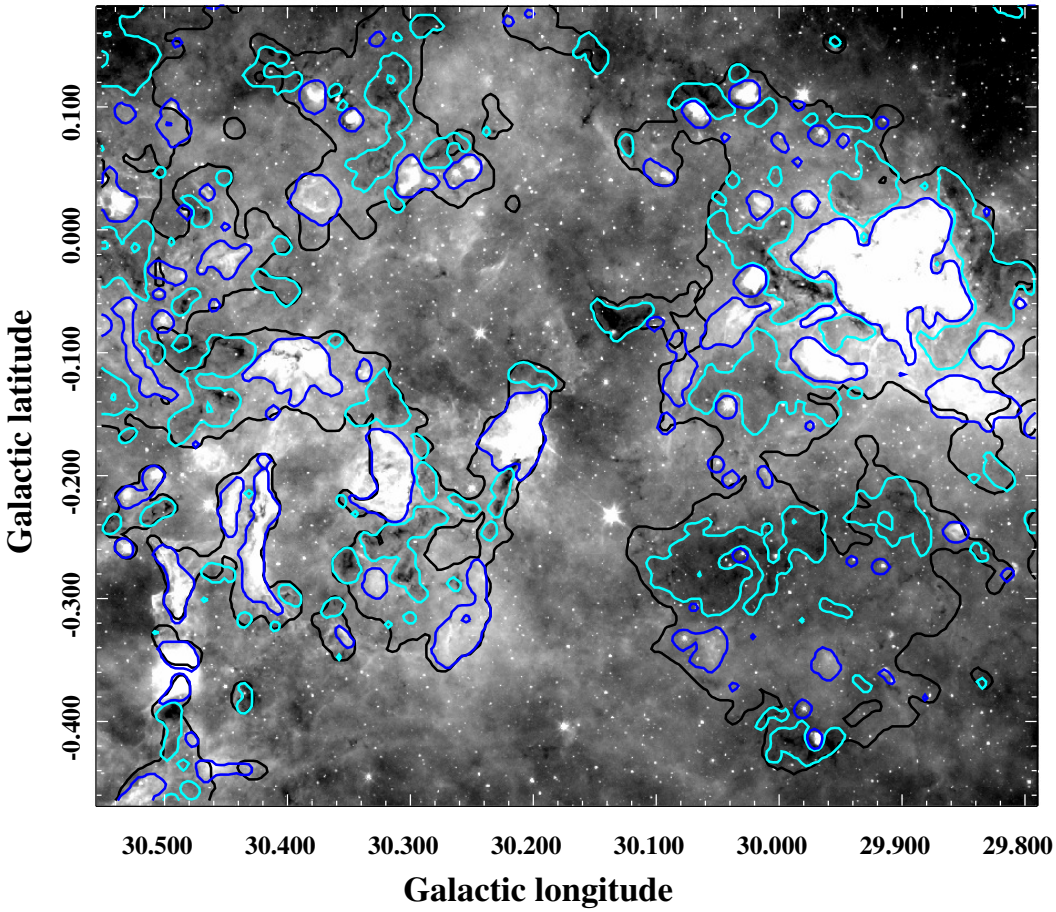

Figure 3.7: GLIMPSE 8 μm image overlaid with contours of the classification as mid-IR-bright (mIRb, dark blue) or mid-IR-dark (mIRd, cyan). The classification is only applied where a far-IR source exists, as denoted by the black contours.

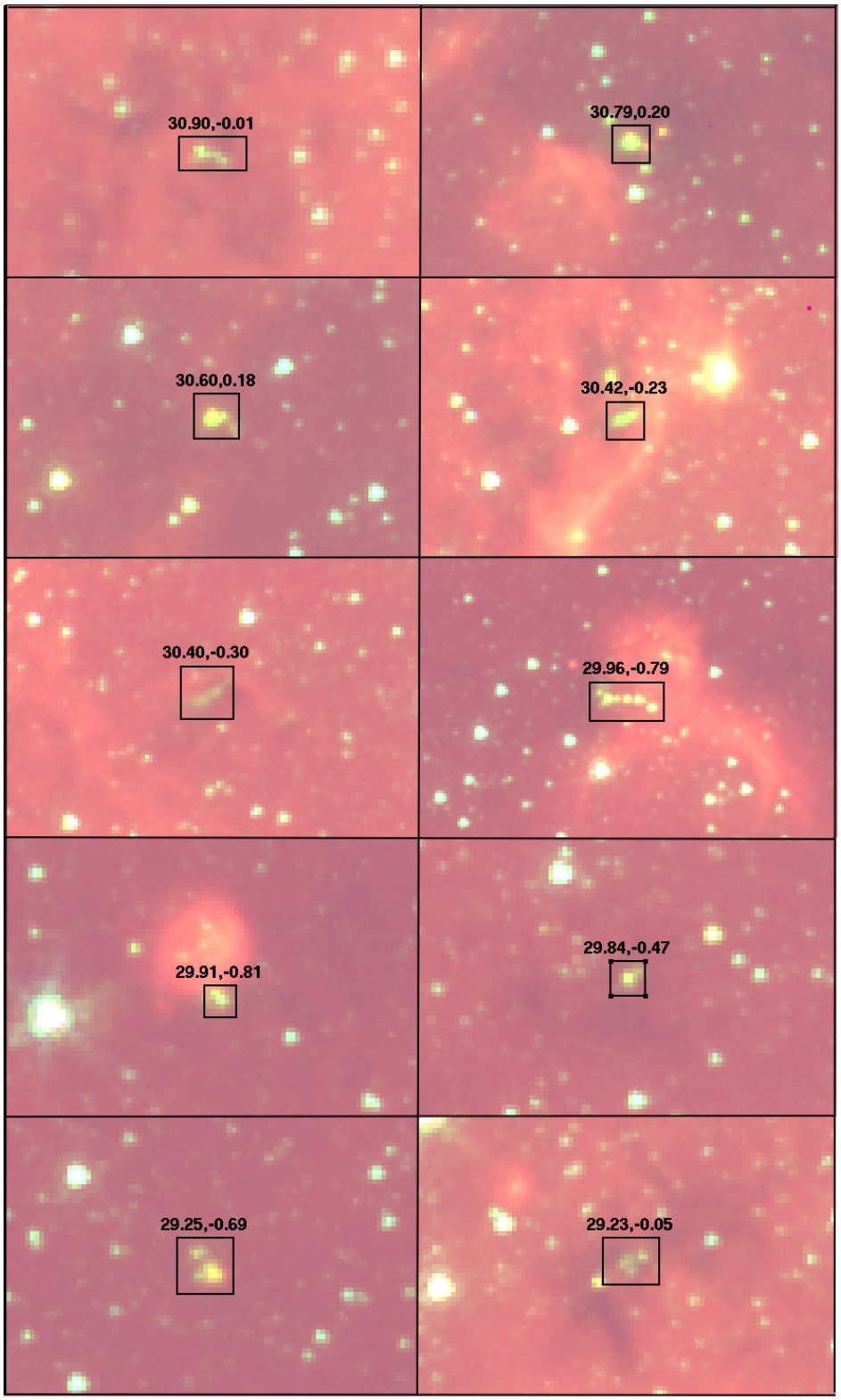

Figure 3.8: GLIMPSE 3-color images (Red: 8 μm, Green: 4.5 μm, Blue: 3.6 μm) of EGOs in the ℓ=30° field. The EGOs shown in the right column of the 3rd and 4th row were identified as "possible" EGOs by Cyganowski et al. (2008) and the others were identified by two independent viewers as EGOs as described in Section 3.3.3. The positions are listed in Table 3.1.

smoothed background. The resulting 'contrast map' enhances the contrast of mIRb and mIRd clouds above the bright mid-IR background. To obtain a fair comparison with the lower resolution ($\sim 25''$) science images, this contrast image is convolved to the same resolution. We then apply a cutoff such that any pixel with a positive contrast greater than or equal to 10% is considered mIRb, and any pixel with a negative contrast greater than or equal to 5% is considered mIRd, while all others are then mIRn. We rely on our eyes to pick out regions of emission and absorption, and have selected the cutoffs that best represent a visual interpretation of that which is dark and bright, as shown in Figure 3.7.

A portion of this label map is shown in Figure 3.7. This method does a good job of picking out the bright and dark regions, and agrees reasonably well (considering the different methods, resolution used, and cutoffs) with the IRDC catalog of Peretto & Fuller (2009). Two important biases to note with this method are: 1) the contrast image technique creates 'negative bowls' around bright objects, and therefore the sizes of the mIRd and mIRb regions are underestimated, and 2) convolving the contrast image to $25''$ resolution causes us to miss some small IRDCs. Additionally, any decrements in the background will be denoted as being mIRd. This issue is partly resolved when we multiply this label map with our source masks, so that our classifications only apply where a Hi-GAL source also exists.

3.3.3.2 MIPSGAL 24μm Emission Label Map

Emission at 24 μm observed using the MIPS instrument traces warm dust. MIPS 24 μm emission can trace warm, diffuse dust in the ISM or warm dust associated with star formation such as material accreting onto forming stars, the gravitational contraction of a young stellar object, or warm dust surrounding a newly formed star. The MIPS 24 μm emission label map was created using the same method as the 8 μm label maps, with the exception that we only include a positive contrast cutoff. While some IRDCs remain dark at 24 μm, the negative contrast is minimal when convolved to $25''$resolution. Additionally, the highest negative contrast in the contrast image arises from the negative bowl artifacts around bright sources, so identifying IRDCs in the 24 μm images

using this method is not adequate. The positive contrast threshhold for the MIPS 24 μm contrast maps was 25%, also chosen by eye. A higher cutoff than at 8 μm was required to select the 24 μm sources above the bright background. These cutoffs greatly affect the resulting trends. See Section 3.4.1 for a discussion of the effects of cutoffs on source identification.

3.3.3.3 Extended Green Objects Label Map

We include the presence of Extended Green Objects (EGOs, also called "green fuzzies" Cyganowski et al. 2008; Chambers et al. 2009) as a star formation tracer. EGOs are regions of enhanced and extended 4.5 μm emission and are thought to be indicative of shocks in outflows (Cyganowski et al. 2009). Cyganowski et al. (2008) catalogued EGOs throughout the Galaxy in the GLIMPSE fields. There are two "possible" EGOs in the ℓ=30° field which we include in our EGO label map. We supplemented the Cyganowski et al. (2008) catalog with an independent visual search of the ℓ=30° field for EGOs that may have been missed. An independent, cross-checked search identified eight further candidates, which we include in our analysis. A list of the locations of the EGOs used in this analysis is given in Table 3.1, and they are shown in Figure 3.8. For each EGO, a box was drawn around the region that contains the EGO, and each pixel in this box was given a flag of 1, while for pixels outside the box the flag is 0.

3.3.3.4 6.7 GHz Class II CH_3OH Masers Label Map

Finally, we employ the presence or absence of 6.7 GHz Class II CH_3OH masers as a star formation tracer. We use the complete catalog compiled by Pestalozzi et al. (2005) to identify unbiased searches for 6.7 GHz methanol masers in the ℓ=30° field. While there have been numerous targeted searches for CH_3OH masers, we utilize the unbiased Galactic Plane searches of Szymczak et al. (2002) and Ellingsen (1996), on the 32m Torun Radio Telescope (FWHM of 5.5′) and the University of Tasmania 26m Radio Telescope (FWHM of 7′), respectively. 6.7 GHz methanol masers are found to be exclusively associated with massive star formation (Minier et al. 2003), and are often offset from the radio continuum emission indicative of an UCHII Region (e.g. Walsh et al.

Table 3.1: EGOs Used in This chapter

EGO Name	R.A. (J2000)	Decl. (J2000)	ℓ x b Size($''$)	Ref.[a]
G29.23-0.05	18:44:51.4	-03:18:41.7	14 x 12	1
G29.25-0.69	18:47:10.7	-03:35:42.0	14 x 14	1
G29.84-0.47	18:47:28.8	-02:58:03.0	9 x 9	2
G29.91-0.81	18:48:47.6	-03:03:31.1	8 x 8	1
G29.96-0.79	18:48:49.8	-03:00:28.7	32 x 32	2
G30.40-0.30	18:47:52.6	-02:23:12.2	17 x 17	1
G30.42-0.23	18:47:40.8	-02:20:31.6	12 x 12	1
G30.60+0.18	18:46:33.7	-01:59:30.3	14 x 14	1
G30.79+0.20	18:46:48.2	-01:48:54.4	12 x 12	1
G30.90-0.01	18:47:45.9	-01:49:00.0	14 x 7	1

[a]1:This work (see Section 3.3.3 and Figure 3.8), 2: Cyganowski et al. (2008)

1998; Minier et al. 2001) and are thought to represent an earlier stage of massive star formation. We chose to include only the unbiased catalogs of Ellingsen (1996) and Szymczak et al. (2002) so as not to choose mIRb regions preferentially. These catalogs together give 22 methanol maser regions, which we use to create a label map where the "size" of the methanol maser regions is given by 2$\times$ the positional accuracy RMS of the observations ($30''$ and $36''$ for Szymczak et al. 2002; Ellingsen 1996, respectively). Methanol maser emission comes from very small areas on the sky (e.g. Walsh et al. 1998; Minier et al. 2001), however, methanol masers are often clustered (Szymczak et al. 2002; Ellingsen 1996, find multiple maser spots towards the majority of sources), so these "source label sizes" are meant to indicate the extent of the star-forming region.

3.4 Results

We discuss here the results of the modified blackbody fits, the properties of the Galactic cirrus emission, a comparison of mIRb and mIRd pixels, and the association with star formation tracers. We discuss what defines the populations of mIRb and mIRd sources, and the objects which have no mid-IR association. Before the discussion of the results, we first mention the many caveats and uncertainties that accompany these findings.

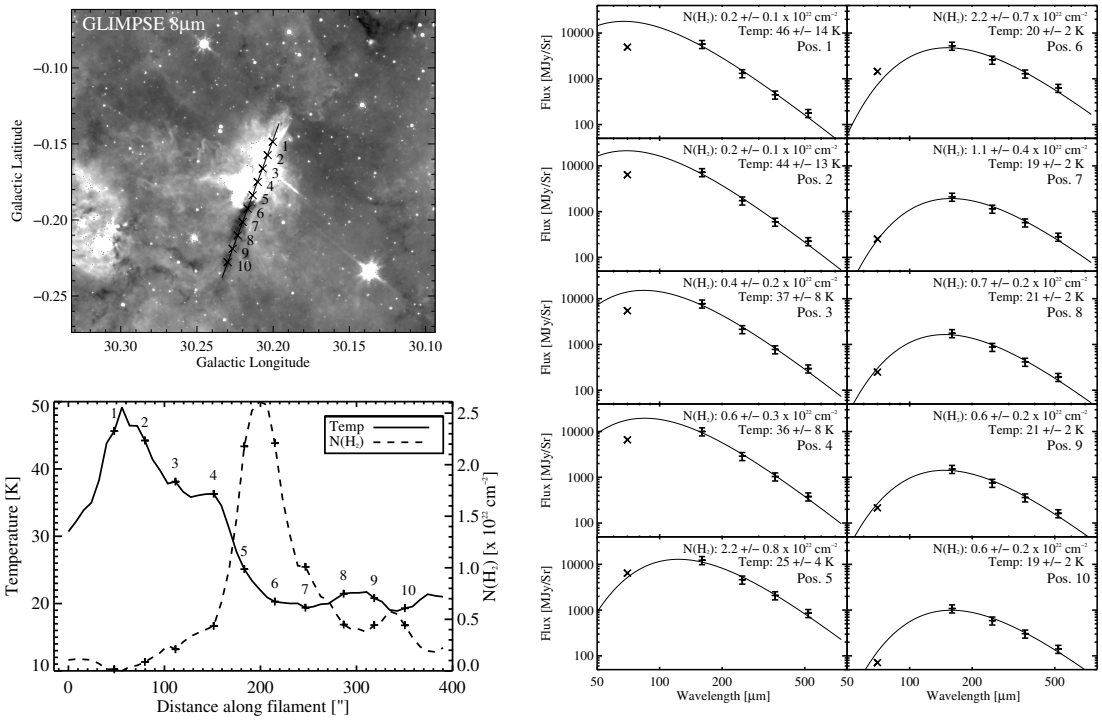

Figure 3.9: *Top Left:* GLIMPSE 8 μm image in our ℓ=30° test region. *Right:* Modified blackbody fits to the points marked on the filament in the top left panel. Since the 70 μm point is not included in these fits (see Section 3.3.2) it is plotted as an X while the other points are shown with their 20% calibration error bars. The errors quoted in temperature and column density are the formal fit errors. As discussed in Section 3.4.1, these are not necessarily representative of the true errors. *Bottom Left:* The temperature and column densities derived along the filament, with 10 points marked. Note the inverse relation between temperature and column density in this example, especially from points 8 to 10.

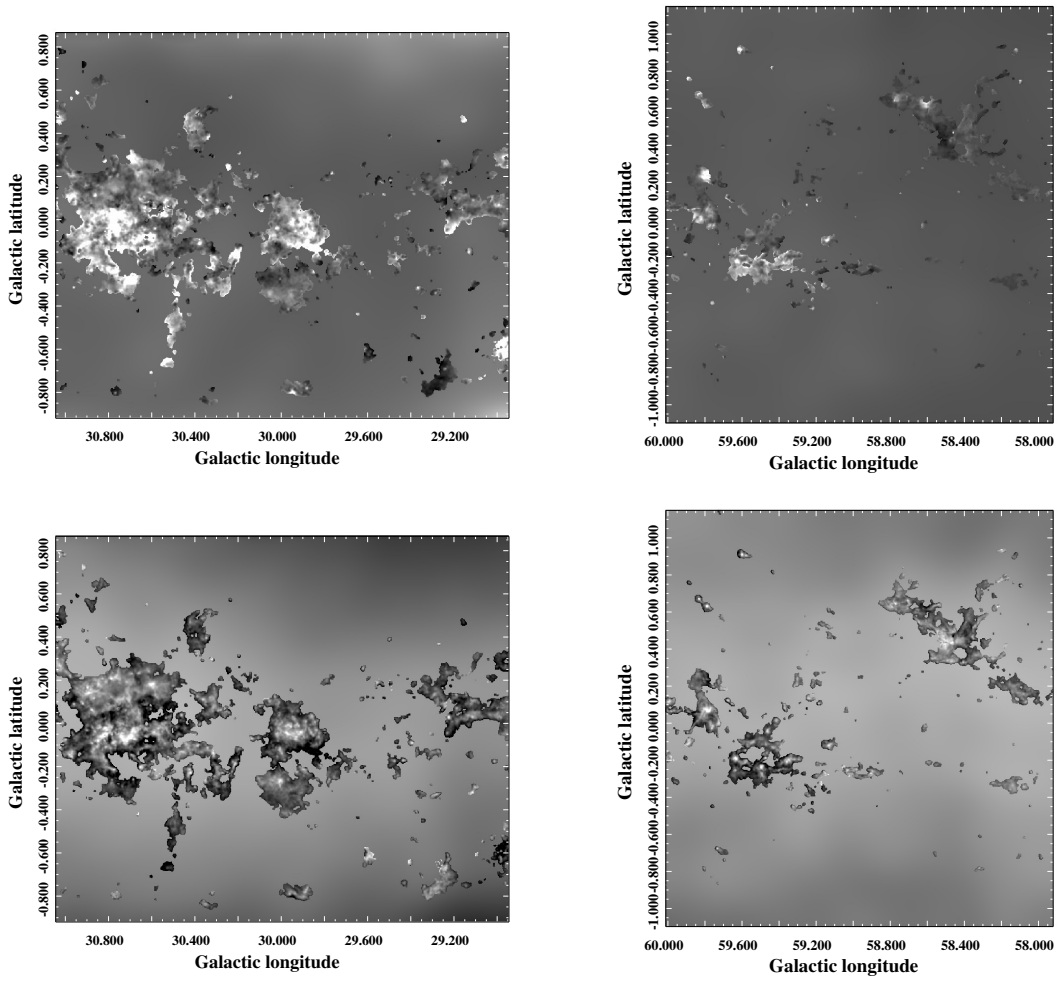

Figure 3.10: *Top:* Temperature (on a linear scale from 0 to 50 K) and *Bottom:* Column Density (on a log scale from $N(H_2)$= 0 to 5 $\times$ 10^{22} cm^{-2}) in the ℓ=30° (left) and ℓ=59° (right) fields. In these maps, the background cirrus emission temperature and column densities are plotted outside of the source masks, while the background-subtracted temperature and column densities are plotted inside the source masks. These maps are at 25″resolution and assume $\beta = 1.75$ inside the source masks.

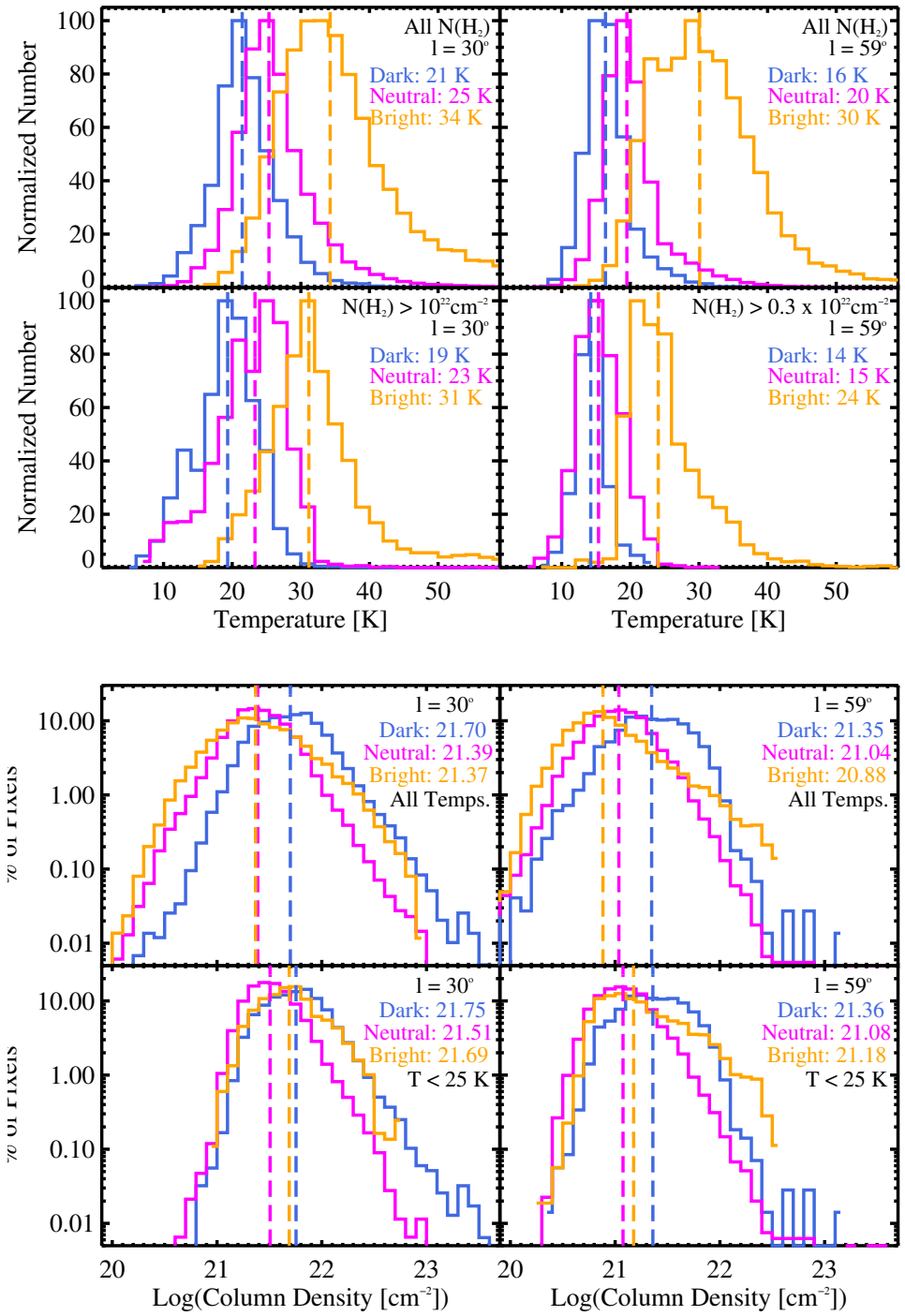

Figure 3.11: Normalized temperature and column density histograms of source pixels in the Hi-GAL fields separated by their 8 μm association; mid-IR-dark (mIRd), mid-IR-neutral (mIRn), or mid-IR-bright (mIRb). The values printed on the plots are the medians of the distributions (also seen in Table 3.3). The mIRd pixels tend to have the lowest temperature and highest column density, while the mIRb pixels have the highest temperature and lowest column density, and the mIRn pixels fall in the middle. *Left:* Normalized temperature histograms in the ℓ=30° (left) and ℓ=59° fields (right), top panels include all source pixels while the bottom panels only include source pixels above a column density cutoff. Introducing this column density cutoff decreases the average temperature, especially for the mIRb pixels. *Right:* Normalized percentage logarithmic column density histograms in the ℓ=30° (left) and ℓ=59° fields (right), top panels include all source pixels while the bottom panels only include source pixels with a temperature below 25 K. These low temperature pixels have higher column densities on average, especially the mIRb ones.

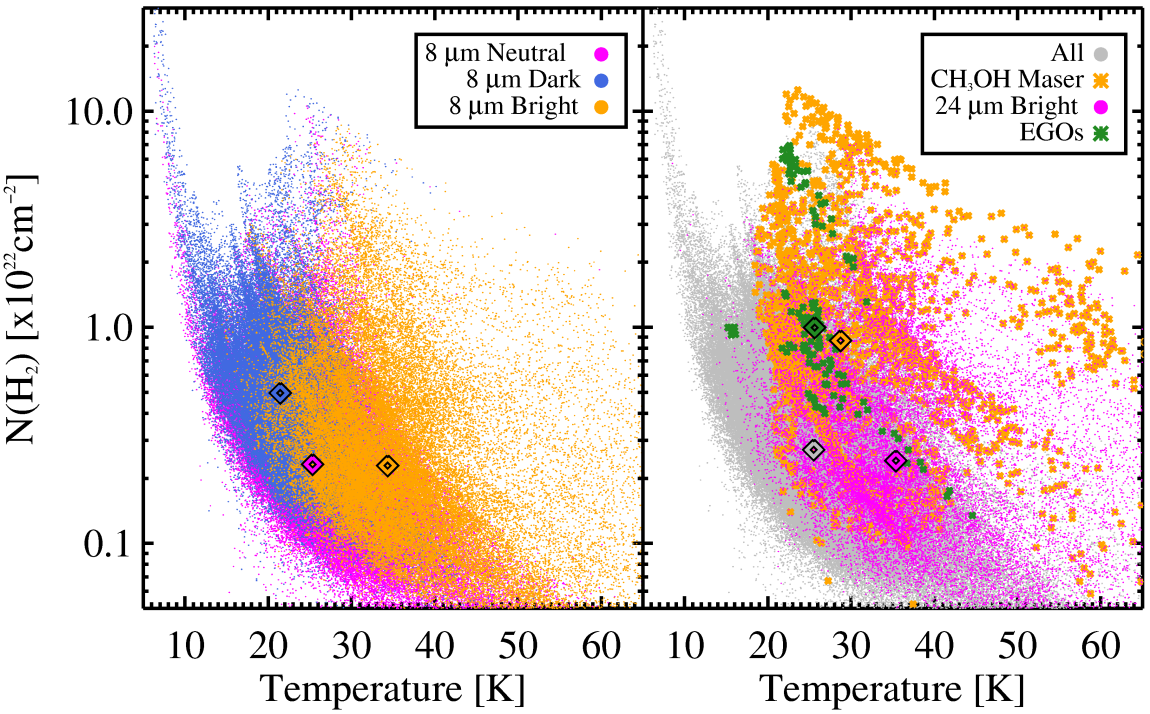

Figure 3.12: *Left:* A column density versus temperature plot comparing mIRn (8 μm neutral, magenta), mIRd (8 μm dark, blue), and mIRb (8 μm bright, orange) pixels within the ℓ=30° source masks, with the median of each value plotted as a diamond on top. The mIRd points occupy the coldest, highest column density portion of the plot, while the mIRb points occupy a range of column densities and warmer temperatures. The mIRn points at the extreme left of the plot are due to the imperfect definition of the 8 μm masks. *Right:* A similar plot as the left, but with all points (gray), points associated with a CH_3OH maser (orange) or EGO (green), and 24 μm bright points (magenta). We note that EGOs occupy a mid-range temperature and the highest column density portion of this plot, while the CH_3OH maser points occupy a wide mid-range of temperatures and a high range of column densities. The 24 μm points are associated with higher temperature points and relatively low column density.

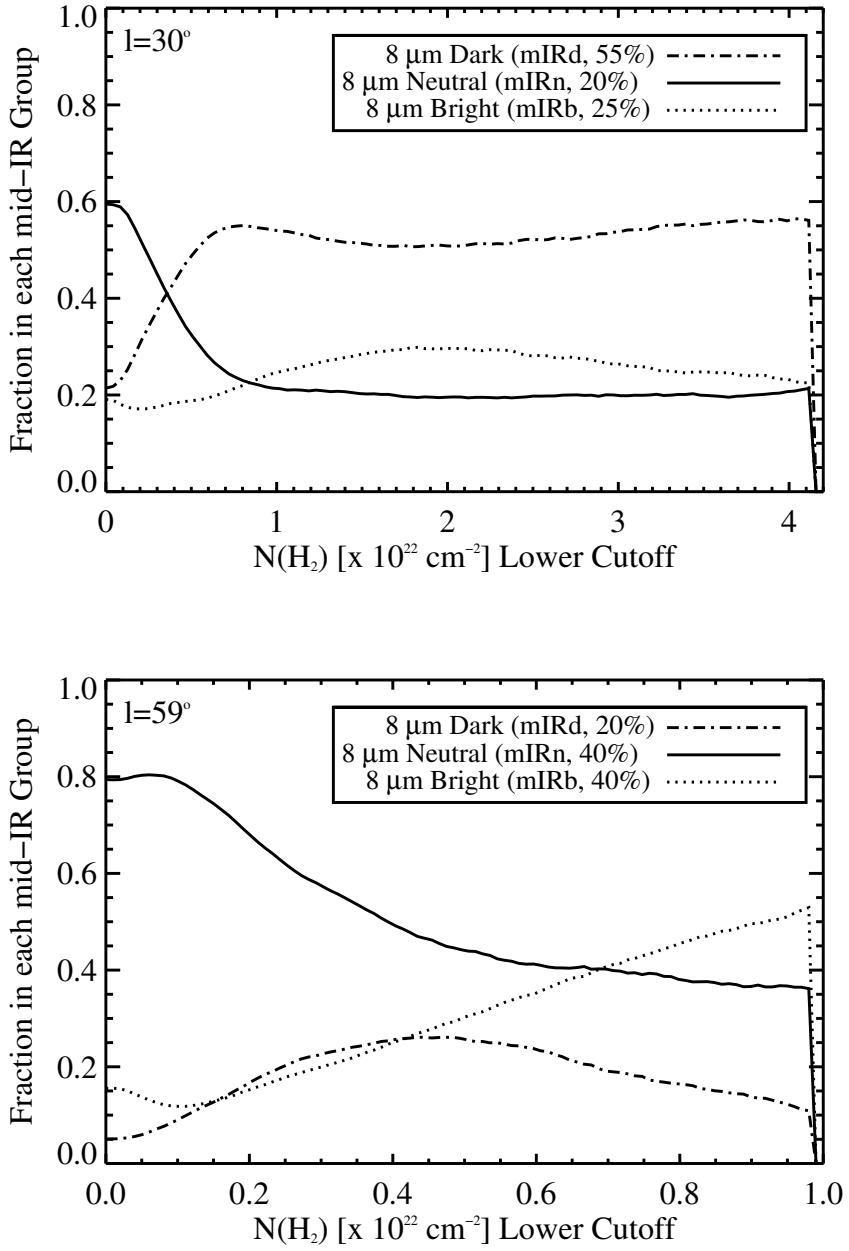

Figure 3.13: Fraction of pixels in each mid-IR categorization (mIRd, mIRn, mIRb) as a function of column density cutoff for the ℓ=30° (top) and ℓ=59° (bottom) fields. In the ℓ=30° field, as the column density cutoff is increased, the mIRd pixels become much more prevalent, replacing the common, but low-significance mIRn pixels, whereas in the ℓ=59° field, the mIRb pixels become more prevalanet as the mIRn contribution lowers. We conclude that in the ℓ=30° field, about 55% of the far-IR sources are mIRd, 20% are mIRn, and 25% are mIRb, while in the ℓ=59° field, about 20% are mIRd, 40% are mIRn, and 40% are mIRb. It is evident from these plots, however, that these numbers are somewhat subjective and can vary depending on the cutoff selected.

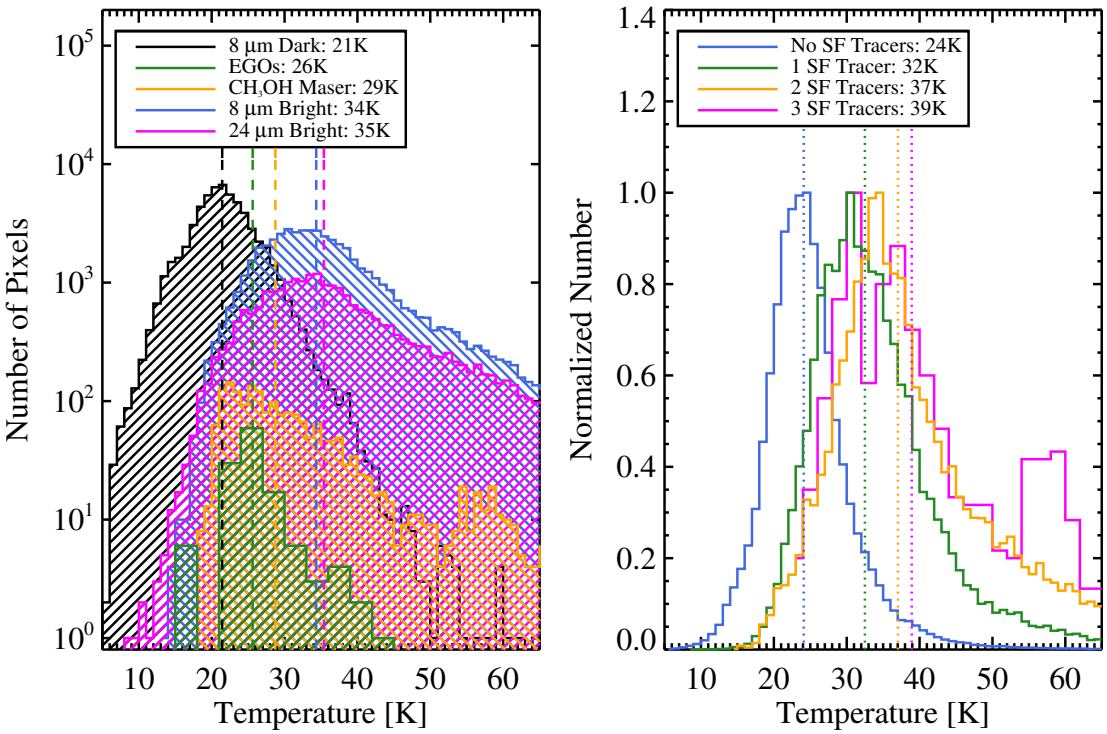

Figure 3.14: A comparison of star formation tracers in the ℓ=30° field. The identification of these tracers is discussed in Section 3.3.3. *Left:* Log histogram of the temperature distributions for all source pixels identified as mIRd (8 μm dark, black), associated with EGOs (green) or a CH_3OH maser (orange), mIRb (8 μm bright, blue), or 24 μm bright (magenta). The median temperature is reported in the legend and with the dashed vertical line for each tracer. If one assumes that a source will monotonically increase in temperature with time, this diagram gives a possible indication of the observed evolution of sources in this field. *Right:* A normalized temperature histogram for all pixels in the ℓ=30° source masks containing 0 (blue), 1 (green), 2 (orange), and 3 (magenta) of the star formation tracers shown in the left panel. The pixels containing 4 star formation tracers are rare, follow the distribution of the EGOs, and have low number statistics and therefore are not plotted. The median temperature is again reported in the legend and with dotted vertical lines. This plot shows that warmer pixels are associated with more star formation tracers.

3.4.1 Remarks on Caveats and Uncertainties

A major uncertainty in this analysis is the use of simple modified blackbody fits. Firstly, star-forming regions show structure on many scales, and so fitting a single column density and temperature to any point does not adequately represent the whole region; rather it serves as a way to categorize and differentiate between bulk, large-scale physical properties of regions. Additionally, this means that the quantities derived are likely to be highly beam-diluted. The true peak column density in any given region is almost certainly higher than the beam-averaged column density reported here. Likewise, the beam-averaged temperatures reported for cold objects are overestimates of the true temperature minimum, while the beam-averaged temperatures reported for hot objects is an under-estimate of the peak. These caveats explain the somewhat small dynamic range observed in both temperature and column density.

In addition, the parameters derived from the modified blackbody fits themselves are rather uncertain. For most of the sources, the temperature is higher than 18 K, so all the points used in the fit lie near the peak of the SED or on the Rayleigh-Jeans slope. This equates to large uncertainties in the fits, especially at high temperatures. The median errors in the derived temperature are about 4 and 3 K (for the ℓ=30° and ℓ=59° fields, respectively), while the median errors in the derived column density are N(H_2) $\approx$ 0.12 and 0.04 $\times$ 10^{22} cm^{-2} (in ℓ=30° and ℓ=59° fields, respectively). The error is a strong function of the parameter value, with a median temperature error of 13% and 18% and median column density error of 44% and 48% (in the ℓ=59° and ℓ=30° field, respectively). These uncertainties are based on the 20% calibration uncertainty assigned to the Hi-GAL fluxes. Additionally, the derived quantities highly depend not only on the background that is subtracted, but also on possible departures between the gain of the PACS and the SPIRE data. Improvements to the general issue of the Planck-Herschel cross calibration with respect to the accuracy of the offset determination as well as to the gain values will be addressed in the future.

The assumption of a fixed β can be considered to contribute the bulk of the uncertainty in the temperature determination. The degeneracy of β-T has been discussed in Paradis et al. (2010).

If we adopt a value of $\beta = 1.5$ (instead of 1.75), the temperatures are about 4K higher on average, and the column densities are about the same. If we adopt a value of $\beta = 2.0$ (instead of 1.75), the temperatures are about 3K lower on average, and again, the column densities are about the same. With only four data points to constrain the fits, fixing β is nearly essential, with the choice of 1.75 being a reasonable guess for these environments. Variations in β from 1.75 to 1.5 or 2 correspond to changes in temperature of about 3 or 4 K. There is the possibility that systematic changes in β, for example a systematic decrease in β toward the center of IRDCs due to dust coagulation (Ossenkopf & Henning 1994), could systematically change our results. In the dark centers of IRDCs, however, a variation in β only changes the temperature by about 2 K (2 K hotter for $\beta = 1.5$, and 2 K colder for $\beta = 2.0$), so while this is an important effect to consider, it is unlikely to negate the observed trends in temperature.

The association with star formation tracers is also subject to uncertainties. Each of the tracers included are not perfectly represented with our methods. The 8 and 24 μm label maps depend entirely on the cutoffs chosen. While we have done our best to choose reasonable cutoffs, a change in these cutoffs would have a significant effect on the properties inferred. The association with EGOs suffers from a similar bias. We have made a careful attempt to identify probable EGO candidates, but the objects themselves are somewhat ill-defined, so again, we resort to the by-eye classification. The association with CH_3OH masers is robust in that it is based on uniform sensitivity blind surveys; however, these surveys suffer from large beam sizes and confusion which consequently beam-dilute their true physical properties. All of these tracers also suffer from the inherent scatter that comes along with varying levels of extinction and different distances.

Despite these caveats, the trends observed over many pixels remain robust. The pixel-by-pixel comparison is an important technique for achieving the best possible associations with the given data, and therefore, the most robust statistics. The object in the center of Figure 3.9 highlights the importance of comparing values on a pixel-by-pixel basis, rather than denoting the entire object as either mIRb or mIRd.

3.4.2 Properties of the Cirrus Cloud Emission

The diffuse Galactic cirrus emission, identified early with IRAS (Low et al. 1984), is thought to be due to the ISM, which is constantly being injected with energy through spiral shocks and stellar feedback and is probably radiatively heated. The emission we see as cirrus most likely comes from a large column of diffuse dust, rather than a single cloud. Various studies have characterized the cirrus noise through its power spectrum (e.g., Gautier et al. 1992; Miville-Deschênes et al. 2007; Roy et al. 2010) and most recently, Martin et al. (2010) have performed a direct estimate of cirrus noise using Hi-GAL.

While we primarily consider the cirrus cloud emission as "background" in this chapter, we report here some useful physical properties derived in this analysis. These maps were smoothed to 12′ (Θ_{FWHM}) resolution, so we report only the average properties in Table 3.2. These data suggest that dust in diffuse clouds in the molecular ring (ℓ=30° field) is warmer, has higher column densities, and a steeper spectral index (β) than dust in diffuse clouds toward the mid-outer Galaxy, outside the molecular ring (ℓ=59° field). In the cirrus background determination, we fit a Gaussian of the form: $g = B + A\exp^{(b-b_0)^2/2\sigma^2}$ across Galactic latitude at each Galactic longitude. We report here the Gaussian fit to the median value across Galactic longitudes. In the ℓ=30° field, the best fit parameters are A = 285 MJy/sr, B = 38 MJy/sr, b_0 = -0.1° , and σ = 0.4° , while in the ℓ=59° field, the best fit parameters are A = 53 MJy/sr, B = 29 MJy/sr, b_0 = 0.1° , and σ = 0.4° . Previous studies (e.g., Rosolowsky et al. 2010) have shown that the mean Galactic latitude where emission peaks depends strongly on the Galactic latitude observed, but that the mean in the First Galactic Quadrant is $\langle b \rangle \approx$ -0.1° . This negative value of the mean Galactic latitude may be related to the location of the sun in the Galaxy. The ℓ=30° field also shows an average Galactic latitude of about -0.1° , while the ℓ=59° field is higher than the average at b0=0.1° . It should be noted that the value of mean Galactic latitude of emission can be severely biased due to the presence of large cloud complexes, especially in small fields.

Table 3.2: Smoothed Cirrus Emission Properties

Hi-GAL Field	β [1]	N(H_2) [1] ($\times 10^{22}$ cm^{-2})	Temperature [1] (K)
ℓ=30°	1.7 ± 0.2	0.7 ± 0.3	23 ± 1
ℓ=59°	1.5 ± 0.2	0.3 ± 0.1	21 ± 1

[1] The values given are the median of all valid values in the map, and the uncertainty quoted is the standard deviation.

3.4.3 The Temperature and Column Density Maps

We present full temperature and column density maps of the Hi-GAL ℓ=30° and ℓ=59° SDP fields. These maps are shown in Figure 3.10 and will available to download as FITS files online with the Hi-GAL data when the processed data is released publicly. The source mask label maps, the source mask temperature and column density maps, the error maps of these quantities, the cirrus emission temperature, column density, and β maps, and their error maps as well as the star formation tracer label maps will all be available for download. The maps presented in Figure 3.10 are displayed such that the values inside the source masks represent the background-subtracted fit values, while the values outside the source mask are the fits to the background itself.

The uncertainties in these maps are discussed in Section 3.4.1. In addition to those, we found that in the ℓ=30° field, our fits were returning unsensible parameters at high Galactic latitudes ($|b| \gtrsim 0.8°$). This is due to imperfect calibration of the zero-level offsets which is especially problematic at high Galactic latitudes where the flux levels are already low. This imperfect calibration negates any physical meaning in the relative fluxes of the Hi-GAL bands in this region. We do not see this same problem in the l=59° field, presumably due to the overall lower variance in flux values from high to low Galactic latitudes. We made several attempts at correcting or properly ignoring those points, with little success, and therefore, recommend that the maps in the ℓ=30° field only be used within $|b| \leq 0.8°$. Additionally, pixels near the edges of the source masks were just barely above the background, and can produce unphysical fits, so be cautious of any pixel that is right on the edge of the source mask.

Table 3.3: Source Properties by Their Mid-IR Association

Hi-GAL Field	Mid-IR Classification	Temperature[1] (K)	High $N(H_2)$ Temp.[2] (K)	Column Density[1] ($\times 10^{22}$ cm^{-2})	Low Temp. $N(H_2)$[3] ($\times 10^{22}$ cm^{-2})
ℓ=30°	Dark (mIRd)	21	19	0.50	0.57
	Neutral (mIRn)	25	23	0.25	0.32
	Bright (mIRb)	34	31	0.23	0.49
ℓ=59°	Dark (mIRd)	16	14	0.22	0.23
	Neutral (mIRn)	20	15	0.11	0.12
	Bright (mIRb)	30	24	0.08	0.15

[1] The values given are the median of all valid values in the map.
[2] The median temperature of all valid points in the map with $N(H_2) > 10^{22}$ cm^{-2} in the ℓ=30° field and $N(H_2) > 0.3 \times 10^{22}$ cm^{-2} in the ℓ=59° field (to account for the fact that column densities in the ℓ=59° field are about 1/3 of that in the ℓ=30° field).
[3] The median column density of all valid points in the map with T < 25 K.

The column density follows the far-IR flux closely, while the temperature is quite varied, and in many cases, inversely correlated with the column density. The median temperatures for all the pixels in the source masks are 26 and 20 K, while the median column densities are 0.25 and 0.10 $\times 10^{22}$ cm^{-2} (for the ℓ=30° and ℓ=59° field, respectively). The highest column density points are found in W43, the large complex near ℓ=30.75° , b=-0.05° (Bally et al. 2010), where the bright millimeter points, MM1 - MM4, have beam-averaged column densities of $N(H_2) \approx 10^{23}$ cm^{-2}.

3.4.4 The association of Far-IR Clumps with mIRb and mIRd sources

The association of Hi-GAL sources identified in the Far-IR with mid-IR sources is of interest, as that gives some indication of their star-forming activity. We find that Hi-GAL sources span the range of pre- to star-forming and that there exist significant trends in both temperature and column density between these populations. The growing interest in IRDCs as potential precursors to stellar clusters emphasizes the importance of identifying IRDC-like sources throughout the Galaxy in an unbiased manner, not just where they happen to exist in front of a bright mid-IR background. A survey such as Hi-GAL is essential to identify IRDC-like objects throughout the Galaxy while a thorough analysis is necessary for understanding the trends in Hi-GAL sources that are pre- versus

star-forming.

We find that mIRd pixels are characterized by colder temperatures (by more than 10 K) and higher column densities (by about a factor of two) than mIRb pixels (see Table 3.3). The mIRn pixels generally have a column density similar to that of mIRb pixels, and a temperature midway between mIRd and mIRn pixels (see Figure 3.11). This trend is also apparent in the left panel of Figure 3.12. The mIRn points at the extreme left in the left panel of Figure 3.12 are due to the imperfect definition of the 8 μm masks. Where mIRb and mIRd regions are adjacent, the pixels between are denoted as mIRn since the two adjacent regions are blurred. This causes some pixels to be denoted as mIRn which may truly be mIRd or mIRb. Figure 3.11 shows that introducing a column density cutoff to the temperature distribution decreases the average temperature, especially for mIRb pixels. If, on the other hand, we introduce a temperature cutoff ($T < 25$ K) to the column density distributions, the average column density increases.

A simple K-S test rules out the possibility that any combination of the mIRd, mIRn, or mIRb populations in temperature or column density are drawn from the same distribution with at least 99.7% confidence. For the K-S test, we calculated the effective number of independent points in each distribution by dividing the number of pixels in each distribution by the number of pixels per beam. Considering the errors discussed in Section 3.4.1, these trends are significant and not likely to be a by-product of systematic errors. Hi-GAL is sensitive to both cold, high column density, likely pre-stellar sources and warmer, more diffuse star-forming regions. We can distinguish between these using the temperature and column densities derived simply from Hi-GAL or through comparison with other tracers.

In Figure 3.13, we plot the fraction of mIRd, mIRn, and mIRb pixels above the column density cutoff plotted on the x-axis. In the ℓ=30° field, the mIRn fraction drops quickly as the mIRd fraction rises, while in the ℓ=59° field, mIRb fraction rises steadily as the mIRn fraction drops. While assigning an overall percentage to each of the categories is somewhat subjective, because of the cutoff-dependent variations, we estimate that in the ℓ=30° field about 55% of the Hi-GAL identified source pixels are mIRd, 20% are mIRn, and 25% are mIRb. In the ℓ=59° field,

we estimate that about 20% of the Hi-GAL identified source pixels are mIRd, 40% are mIRn, and 40% are mIRb. The fact that the fraction of mIRd pixels in the ℓ=59° field is so much lower than that in the ℓ=30° field could be an artifact of the relatively sparse mid-IR background emission in the ℓ=59° field, or it could very well be that there is a lower fraction of cold, high-column density clouds in the ℓ=59° field.

3.4.5 Star Formation Tracers in Hi-GAL Sources

We compare the temperature and column density maps with the star formation tracer label maps (discussed in Section 3.3.3). While we evaluate the evolution of sources by their temperature alone, Beuther et al. (2010) analyze the evolution of four sources with changes over the entire SED. We find that the more star formation tracers associated with a source, the higher the temperature (see Figure 3.14 right). This trend is not surprising: a star-forming clump will be warmer than a pre-star-forming clump. It is reasonable to assume that as a clump evolves, the temperature will increase monotonically. Therefore, we compare the individual star formation tracers with temperature to see if there is any indication about which star formation tracer may turn on first, and what the relative lifetimes might be. The uncertainties in this analysis arediscussed in 3.4.1.

In the left panel of Figure 3.14 we see a progression of star formation tracers with temperature, with a significant overlap. The median temperatures of each population (denoted with a dotted line, and stated in the legend) delineate a monotonic sequence from cold pre-stellar clumps to warm star-forming clumps, from mIRd, to outflow/maser sources, to sources which are bright at 8 and 24 μm. However, the overall distributions are broad, possibly indicating long lifetimes, but more likely an indication of large errors in both the beam-averaged physical properties and the assignment of star formation tracers.

Additionally, the mass (and therefore bolometric luminosity) of each source will have a significant impact on the derived temperatures. This is not included in our evolutionary sequence, as temperature is assumed to monotonically increase with evolution. This would have the effect of preferentially placing high mass star-forming regions at later evolutionary states and low-mass

ones at earlier evolutionary states. However, the massive star must have turned on already to yield this effect, so placing those warmer sources at later evolutionary stages is fair assuming the peak column densities (and therefore most massive star formed) are the same between the colder and warmer sources.

Figure 3.12 shows these trends in both temperature and column density space. The left panel shows that mIRd pixels are generally colder and have higher column densities than mIRb pixels. The right panel shows that all the star formation tracer pixels are warmer than the mIRd population, with CH_3OH masers in the mid-range of temperatures, and 24 and 8 μm bright pixels occupying the highest temperature range. EGOs are characterized by a similar temperature as CH_3OH masers, but a slightly higher column density. Interestingly, the EGOs seem to occupy two distinct regions on the plot in Figure 3.12, one higher and one lower column density, indicating that EGOs are present in a variety of environments. It is not surprising that the EGOs represent the highest column density population, as they are the most localized star formation tracer we have used.

We perform simple K-S tests to determine the likelihood that any combination of the temperature or column density distributions of star formation tracers (pixels which are mIRd, mIRb, 24 μm bright, or contain EGOs or masers) are drawn from the same distribution. For the K-S test, we calculated the effective number of independent points in each distribution by dividing the number of pixels in each distribution by the number of pixels per beam (about 23 in the $25''$ resolution images used for all tracers except the masers, which have an accuracy of about $33''$, or 41 pixels). Since EGOs are defined locally, each pixel is considered independent. When we compare the temperature distributions of all combinations of the mIRd, mIRb, 24 μm bright, EGO and maser populations, we can rule out with at least 99.7% confidence that any are drawn from the same distribution, except the 24 and 8 μm bright points, which have about a 55% probability of being drawn from the same distribution, and the EGO and maser populations which have about a 0.5% chance of being drawn from the same distribution. When we compare the column density distributions of all combinations of the mIRd, mIRb, 24 μm bright, EGO and maser populations, we can rule at with at

least 99.7% confidence that any are drawn from the same distribution, except the EGO and maser populations, which have about a 55% chance of being drawn from the same distribution. The fact that EGOs and CH_3OH masers may be tracing the same population of sources is encouraging, as they are both supposed to trace young, massive outflows. We would also have expected that pixels which are bright at 8 or 24 μm should be tracing similar environments, as both can be excited by the heat or UV light from a young, accreting protostar (although 8 μm traces primarily H II regions).

We see interesting trends in Hi-GAL clumps between temperature and column density and star formation tracers. We find that 8 μm dark pixels are, on average, the coldest, followed by pixels containting EGOs and/or CH_3OH masers, then 8 and 24 μm bright points. If we assume that as a clump evolves, it will monotonically increase in temperature with time, then this could suggest a possible sequence of tracers. However, the scatter is still too large to suggest a definitive sequence or lifetimes. We might expect that one of the first detectable stages will be the formation of an outflow, detectable by an EGO or CH_3OH maser. Following that, the protostar will continue to heat its surroundings and light up at 24 μm. A massive protostar should form an UCHII region while still accreting, whose UV light would excite PAHs in the 8 μm band of GLIMPSE. Unlike Battersby et al. (2010), we find that 24 μm sources light up around the same time as 8 μm sources. This is almost certainly due to the use of a high, automated cutoff to determine the existence or absence of a 24 μm source. In Battersby et al. (2010), UCHII regions were associated with very bright ($\gtrsim$ 1 Jy) 24 μm point sources, which may be the population of bright sources we are picking out here. We note that even though most or all UCHII regions are mIRb, certainly not all mIRb sources are UCHII regions (e.g., Mottram et al. 2010). The fact that the population of mIRb and 24 μm bright are so similar is likely an artifact of the cutoffs chosen. The two should be associated for bright sources, which is the trend we see in this chapter, but for dimmer sources, which are excluded by the cutoff, we do not know the association. The detection of an EGO or 24 μm point source depends on the exinction and the background, and the sensitivity for detection will decrease with distance.

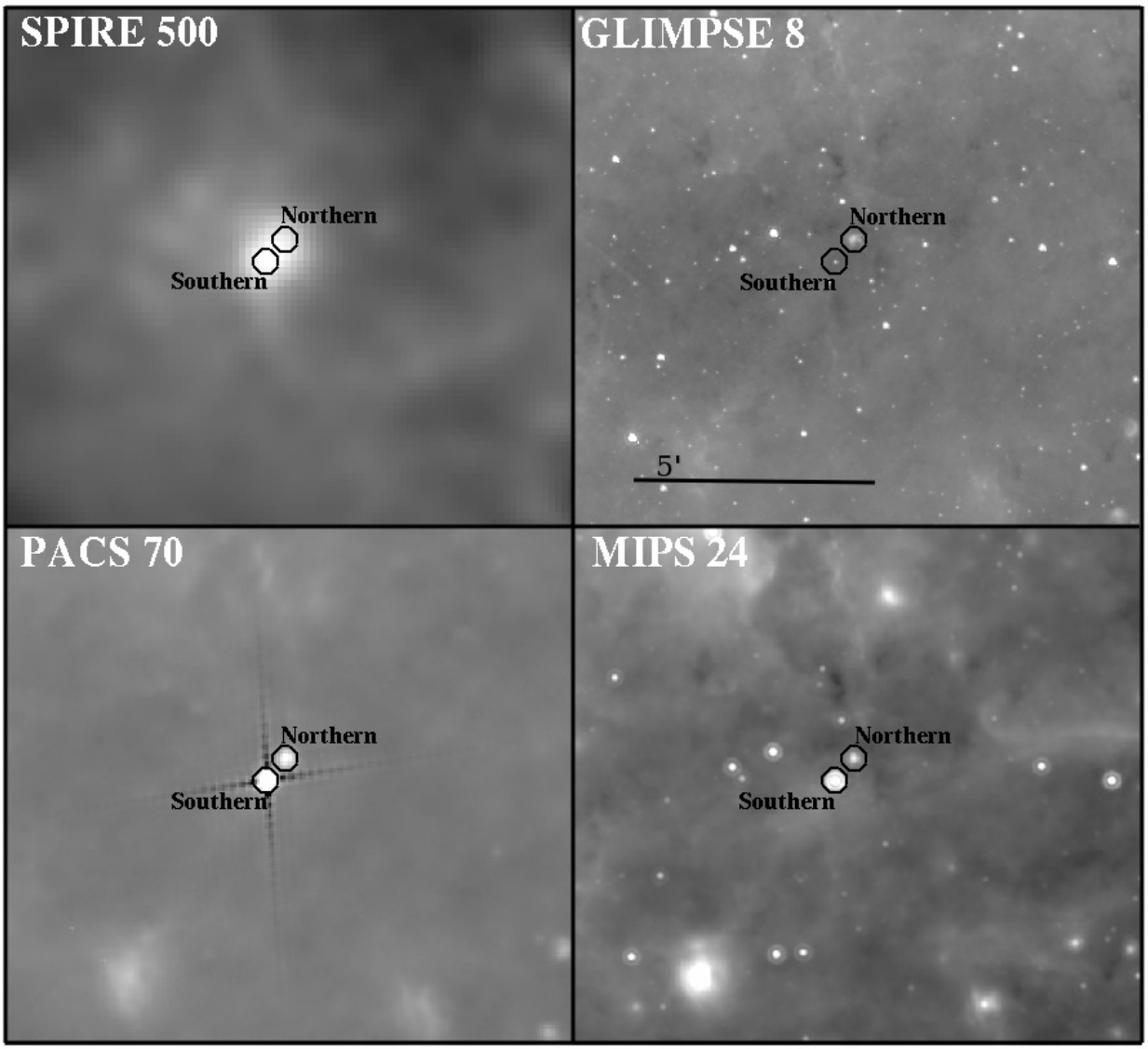

Figure 3.15: A possible IRDC-like source on the far side of the Galaxy. This source is cold ($\sim$ 20 K), has high column density ($\sim 3 \times 10^{22}$ cm^{-2}) and is amidst the bright mid-IR Galactic Plane at (ℓ,b) = (30.01, -0.27). By these measures, it should be an IRDC, but the 8 μm image (top right) shows only a moderate decrement and the near side extinction column density is almost an order of magnitude less than expected from the far-IR column density. This source breaks up into a Northern (ℓ,b) = (30.003,-0.266)and Southern (ℓ,b) = (30.009,-0.274) component at the higher resolution of the PACS 70 μm band. This source is a promising candidate for further study.

Table 3.4: far side IRDC Candidates

Source Name	ℓ (°)	b (°)	Hi-GAL Column ($\times 10^{22}$ cm^{-2})	Extinction[1] Column ($\times 10^{22}$ cm^{-2})	Temperature (K)
G030.60+0.18	30.602	+0.177	6.2	1.1	22
G030.34-0.11	30.345	-0.114	1.7	0.15	19
G030.01-0.27[2]	30.006	-0.270	3.1	0.5	21
G029.31-0.05	29.312	-0.051	1.0	0.06	13
G029.28-0.33	29.284	-0.331	1.6	0.02	20

[1]Not knowing the distances to all these sources, we use the Peretto & Fuller (2009) extinction column density estimation method, which basically assumes the cloud is on the near side of the Galaxy.
[2]This is the source that is discussed in the text in Section 3.5.

3.5 IRDC-like Source Candidates on the far side of the Galaxy

We present a list of candidate IRDCs on the far side of the Galaxy in Table 3.4. These sources are cold ($\sim$ 20 K), high column density ($> 1 \times 10^{22}$ cm^{-2}) objects identified in Hi-GAL with very weak absorption at 8 μm. These are objects that, were they in front of the bright mid-IR background, *should* be IRDCs, but are not. To identify these sources, we calculated an extinction column density map at 8 μm, using the method of Peretto & Fuller (2009) and compared this with the Hi-GAL column density map. Any sources with a Hi-GAL column density $> 1 \times 10^{22}$ cm^{-2} and an extinction column density several (3-4) factors lower was considered. We performed an examination by eye simply to check that these are plausible candidates. The extinction must be weak, the region cannot be mIRb, and it needs to be cold (< 30 K). In other words, these are sources that, if on the near side of the Galaxy, should be dark at 8 μm, yet they are not. None of these sources are identified as IRDCs by the catalog of Peretto & Fuller (2009). Sources at high Galactic latitudes ($|b| \gtrsim 0.5^\circ$) and in the ℓ=59° field were not included because the sparse background adds additional uncertainty to the extinction column density estimate.

We discuss G030.01-0.27, a candidate far side IRDC, in more detail here as an example of this class of objects. G030.01-0.27 is a high-column density ($\sim 3 \times 10^{22}$ cm^{-2}), cold ($\sim$ 20 K) dust continuum source in the ℓ=30° field near the Galactic mid-plane that is not 8 μm dark (see Figure 3.15). There is a slight decrement at 8 μm that is nearly consistent with background fluctuations as this source was not detected in the IRDC catalogs of Peretto & Fuller (2009) or Simon et al. (2006). At 70 μm, this source breaks up into two, a Southern source at (ℓ,b) = (30.009,-0.274) and Northern source at (ℓ,b) = (30.003,-0.266). The Southern source appears to be very small and faint at 8 μm, while the Northern source is a faint, slightly extended source at 8 μm. The Southern source has bright 24 and 70 μm emission. The Northern source is also seen in emission at these wavelengths, though less brightly. Comparison with the MAGPIS (Helfand et al. 2006; White et al. 2005) 20 cm maps show no emission in the radio continuum coincident with either source, while the MAGPIS 6 cm map shows a very faint object associated with the Southern source. This emission

(at 8 μm and the faint emission at 6 cm) indicates some star formation activity, while the cold dust temperature and high column density indicate cold, dense gas available for further star formation.

The faint decrement at 8 μm can be morphologically matched with a molecular cloud in ^{13}CO (Jackson et al. 2006, from the Galactic Ring Survey) at about 104 km s^{-1}. Integrating from 100 to 108 km s^{-1}, assuming 20 K, and using Eq. 17 from Battersby et al. (2010) the column density is about 2.5 $\times 10^{22}$ cm^{-2}, consistent with the Hi-GAL column density estimate. Using the rotation curve of Reid et al. (2009), the near side distance of this ^{13}CO cloud is 5.8 kpc and the far side (far side of the kinematic rotation curve) distance is 8.7 kpc. Using the extinction mass determination technique of Butler & Tan (2009) as applied in Battersby et al. (2010), the 8 μm extinction column density of the cloud is 0.5 $\times 10^{22}$ cm^{-2} assuming it is on the near side of the Galaxy or 1 $\times 10^{22}$ cm^{-2} assuming it is on the far side of the Galaxy. It is not expected that the extinction column density estimation method will be very robust for clouds on the far side of the Galaxy, but this very slight extinction is at least consistent with the cloud being on the far side of the Galaxy. Additionally, this cloud shows no obvious HI self-absorption (Stil et al. 2006). While none of this evidence is conclusive, it all seems to indicate that this cloud is on the far side of the Galaxy. Another possibility, however, would be that this cloud is simply *behind* the majority of the diffuse mid-IR emission, and still on the near side of the Galaxy. Either way, it is an interesting source that was otherwise missed as such in previous study.

The fact that the mid-IR background is bright at the locations of these sources, yet the 8 μm extinction column density is extremely low is a strong indication that these sources are *behind* the bright mid-IR background. In fact, the Hi-GAL distance analysis by Russeil et al. (2011) finds that all the sources in Table 3.4 are either at the far or tangent distance ($>$ 7 kpc) except for G029.28-0.33, which is on the near side at about 6 kpc, so still likely behind most of the bright mid-IR emission.

With their high far-IR column density and low temperature, these sources are easily categorized (based on the left panel of Figure 3.12) as IRDC-like. These are the first candidate far side IRDCs of which the authors are aware. The potential outer Galaxy IRDC identified by Frieswijk

et al. (2007) is similar in that they are both IRDC-like objects identified independent of 8 μm absorption. However, these sources are not in the outer Galaxy, but on the far side of the inner Galaxy. These candidates are just a few of potentially many more IRDC-like sources which remain to be uncovered in a study like this over the Galactic Plane.

3.6 Conclusions

We have performed cirrus-subtracted pixel-by-pixel modified blackbody fits to the Hi-GAL ℓ=30° and ℓ=59° SDP fields. The source identification and cirrus-subtraction routines are robust and can be applied to Hi-GAL data throughout the Galactic Plane. We present temperature and column density maps of the dense clumps in these fields and cirrus column density, temperature, and β maps. We find that the cirrus cloud emission is characterized by $\beta = 1.7$, N(H_2) = 0.7×10^{22} cm^{-2}, and T = 23 K in the ℓ=30° field and β = 1.5, N(H_2) = 0.3×10^{22} cm^{-2}, and T = 21 K in the ℓ=59° field.

We also characterize each pixel as mid-IR-bright (mIRb), mid-IR-dark (mIRd), or mid-IR-neutral (mIRn), based on the contrast at 8 μm. The association of Hi-GAL sources identified in the far-IR with mid-IR sources is of interest, as the far-IR sources span the range of pre- to star-forming regions, and the mid-IR can help to separate these. We find that in the ℓ=30° field, about 55% of the pixels are mIRd, 20% are mIRn, and 25% are mIRb, while in the ℓ=59° field, about 20% are mIRd, 40% are mIRn, and 40% are mIRb. There exist significant trends in temperature and column density between the populations of mIRd to mIRb. We find that mIRd dark pixels are about 10 K colder and a factor of two higher column density than mIRb pixels. The mIRd pixels are likely cold pre-star-forming regions, while the mIRb pixels are in regions that have probably begun to form stars. It is important to note that mIRd pixels may be forming low-mass stars which are simply embedded and not seen at these distances, and that these regions are not necessarily pre-cursors to massive star forming regions. This study has shown that Hi-GAL-identified sources span the range from cold, pre-star-forming to actively star-forming regions.

We also include the presence or absence of EGOs (Extended Green Objects, indicative of

shocks in outflows), CH_3OH masers, and emission at 8 and 24 μm as star formation tracers. We find that warmer pixels are more often associated with star formation tracers and also that the warmer a pixel is the more star formation tracers it is associated with, as seen in Figure 3.14. We also find a wide but plausible trend in temperature, where the coldest pixels, on average, are mid-IR-dark, followed by pixels containing EGOs and/or CH_3OH masers, then 8 and 24 μm bright sources. While the systematic errors are too large to suggest an evolutionary sequence, this trend is intriguing.

Finally, we identify five candidate far side IRDCs. These objects are cold ($\sim$ 20 K), high column density ($> 1 \times 10^{22}$ cm^{-2}) sources identified with Hi-GAL that have very weak or no absorption at 8 μm. We explore one such candidate in more detail in Section 3.5. This object at roughly (ℓ,b) = (30.01, -0.27) has a high far-IR column density (N(H_2) $\sim 3 \times 10^{22}$ cm^{-2}), is cold ($\sim$ 20 K) and in a position near an abundantly bright mid-IR background, yet shows almost no decrement at 8 μm. In fact, the 8 μm extintion-derived column density is almost an order of magnitude lower than expected from the far-IR estimate. These candidate near side IRDCs are the first of their kind of which the authors are aware. This type of analysis will likely uncover many more such objects. With a complete sample of IRDC-like (cold, high column density) clouds, independent of the local mid-IR background, one could map the clouds in the earliest stages of star-formation over the entire Galaxy.

Chapter 4

The Comparison of Physical Properties Derived from Gas and Dust

We explore the relationship between gas and dust in massive star-forming regions by comparing the physical properties derived from each. We compare the temperatures and column densities in a massive star-forming Infrared Dark Cloud (IRDC, G32.02+0.05), which shows a range of evolutionary states, from quiescent to active. The gas properties were derived using radiative transfer modeling of the (1,1), (2,2), and (4,4) transitions of NH_3 on the Karl G. Jansky Very Large Array (VLA), while the dust temperatures and column densities were calculated using cirrus-subtracted, modified blackbody fits to Herschel data. We compare the derived column densities to calculate an NH_3 abundance, $\chi_{NH_3} = 4.6 \times 10^{-8}$. In the coldest star-forming region, we find that the measured dust temperatures are lower than the measured gas temperatures (mean and standard deviations $T_{dust,avg} \sim 11.6 \pm 0.2$ K vs. $T_{gas,avg} \sim 15.2 \pm 1.5$ K), which may indicate that the gas and dust are not well-coupled in the youngest regions or that these observations probe a regime where the dust or gas temperature measurements are unreliable. Finally, we forward model the NH_3 data (calculate millimeter fluxes based on the temperatures and column densities derived from NH_3) to show that millimeter dust continuum observations of massive star-forming regions, such as the Bolocam Galactic Plane Survey or ATLASGAL, can probe hot cores, cold cores, and the dense gas lanes from which they form, and are generally not dominated by the hottest core.

4.1 Introduction

The derivation of physical properties in interstellar space is always subject to bias and observational uncertainty. Toward massive star and cluster forming regions, we are interested in probing the physical conditions of dense molecular gas clumps, which are highly embedded ($A_V \sim$ 10-100). Hence, we observe at longer wavelengths, where the thermal dust emission blackbody spectrum peaks and low energy molecular transitions can be observed. Understanding the physical conditions, like temperature and column density, at the onset of massive star formation provides crucial constraints for models of star and cluster formation.

Many molecular gas species (e.g., CO, NH_3, H_2CO) can be employed for this task, NH_3 being one of the most popular (e.g., Ho & Townes 1983; Mangum et al. 1992; Longmore et al. 2007; Pillai et al. 2006, 2011). NH_3 has been shown to be a reliable tracer of the mass-averaged gas temperatures to within better than 1 K (Juvela et al. 2012). The rotational energy states of NH_3 are described by quantum numbers (J,K) and dipole transitions between different K ladders are forbidden. Therefore, their relative populations depend only on collisions and are direct probes of the kinetic temperature of the emitting gas. Each (J,K) rotational energy level is divided into inversion doublets, the (1,1) and (2,2) inversion transitions being the most commonly observed (e.g., Ragan et al. 2011; Pillai et al. 2006). The hyperfine structure of the inversion transitions allows for straightforward measurements of the optical depth of the lines. The inversion doublet transitions of NH_3 provide a robust and straightforward tool for measuring gas temperatures and column densities.

The optically thin thermal emission from dust grains at long wavelengths can also be utilized to derive the physical conditions deep within massive star and cluster forming regions. To derive the temperature and column density of the observed dust requires fitting a modified blackbody to the dust emission spectra over a range of wavelengths. The measured modified blackbody directly traces the thermal emission from dust grains and provides a reasonable estimate of the dust temperature and column density, the accuracy of which depends on the number of data points, their uncertainty,

and, of course, how well the region can be represented by the model of a modified blackbody at a single temperature, column density, and dust spectral index.

Gas and dust temperatures and column densities are generally used interchangeably in these dense molecular gas clumps. In the densest regions of these clumps we expect the gas and dust to be tightly coupled ($n > 10^{4.5}$ cm^{-3} Goldsmith 2001). In this work, we compare the physical properties derived from gas and dust in a massive star-forming Infrared Dark Cloud (IRDC G32.02+0.05) that shows a range of evolutionary states (Chapter 2). The gas physical properties are derived using radiative transfer modeling of three inversion transitions of para-NH_3 ((1,1), (2,2), and (4,4)) observed with the Karl G. Jansky Very Large Array (VLA) as described in Chapter 2. The dust physical properties are derived using cirrus-subtracted modified blackbody fits data from the Herschel Infrared Galactic Plane Survey (Hi-GAL Molinari et al. 2010) using the method described in Chapter 3. The column densities derived from each tracer are compared with column densities derived using 1.1 mm dust emission data from the Bolocam Galactic Plane Survey (BGPS, Aguirre et al. 2011; Rosolowsky et al. 2010), 8 μm dust absorption data from the Galactic Legacy Mid-Plane Survey Exraordinaire (GLIMPSE, Benjamin et al. 2003) using the method from Battersby et al. (2010), and ^{13}CO emission data from the Boston University-Five College Radio Astronomy Observatory Galactic Ring Survey (BU-FCRAO GRS or just GRS Jackson et al. 2006).

In §4.2 we summarize the data products and methods to derive physical properties. In §4.3 we calculate the abundance of NH_3 in this IRDC and compare the column densities derived from each tracer. §4.4 presents a comparison of the properties derived from gas with those derived from dust. We compare the high-resolution NH_3 observations with lower-resolution observation on the Green Bank Telescope (GBT) in §4.5. Finally, in §4.6, we forward model the high-resolution gas temperatures and column densities derived from the VLA to derive the millimeter fluxes that would be observed with the BGPS, allowing us to explore the high-resolution ($\sim$ 0.1 pc) nature of pc-scale dense, molecular clumps. We conclude in §4.7.

4.2 Data

4.2.1 VLA NH_3

The observations and radiative transfer modeling used to derive NH_3 gas temperatures and column densities are presented and explained in detail in Chapter 2.

The (1,1), (2,2), and (4,4) inversion transitions of para-NH_3 were observed toward two clumps within IRDC G32.02+0.05 with the National Radio Astronomy Observatory[1] Karl G. Jansky Very Large Array (VLA). We observed two clump locations within the IRDC G32.02+0.06, an active clump ([ℓ, b] = [32.032^o, +0.059^o]) and a quiescent clump ([ℓ, b] = [31.947^o, +0.076^o]). The active clump displays signs of active star formation including a 6.7 GHz methanol maser (Pestalozzi et al. 2005), 8 and 24μm emission as well as radio continuum emission (see Chapter 3, White et al. 2005; Helfand et al. 2006) indicative of Ultra-Compact HII Regions. The quiescent clump doesn't show any of those star formation signatures, except for possible association with a faint 24 μm point source. The final beam FWHM produced by the model was about 4.4$''$ ($\sim$0.1 pc at the adopted distance of 5.5 kpc, see Chapter 2) and RMS noise was about 6 mJy/beam.

The gas physical properties were derived from the inversion transitions using radiative transfer modeling of the lines. The ammonia lines were fit with a Gaussian line profile to each hyperfine component simultaneously with frequency offsets fixed. The fitting was performed in a Python routine translated from Erik Rosolowsky's IDL fitting routines (Section 3 of Rosolowsky et al. 2008). Typical statistical errors are in the range $\sigma(\mathrm{T}_K) \sim$ 1-3 K for the kinetic temperature, and $\sigma\left(\log[N(NH_3)]\right) \lesssim 0.05$ (about 10% in N(NH_3)) for the column density of ammonia.

[1] The National Radio Astronomy Observatory is a facility of the National Science Foundation operated under cooperative agreement by Associated Universities, Inc.

4.2.2 Dust Continuum Column Density

4.2.2.1 Herschel Infrared Galactic Plane Survey

The Herschel Infrared Galactic Plane Survey, Hi-GAL (Molinari et al. 2010), is an Open Time Key Project of the Herschel Space Observatory (Pilbratt et al. 2010). Hi-GAL will perform a 5-band photometric survey of the Galactic Plane in a $|b| \leq 1^o$ -wide strip from -70$^o \leq \ell \leq 70^o$ at 70, 160, 250, 350, and 500 μm using the PACS (A Photodetector Array Camera and Spectrometer, Poglitsch et al. 2010) and SPIRE (Spectral and Photometric Imaging Receiver, Griffin et al. 2010) imaging cameras in parallel mode. We use the Hi-GAL data to derive dust continuum column densities and temperatures at 25$''$ resolution using pixel-by-pixel modified blackbody fits to the SPIRE 500, 350, and 250 μm data. Generally, the PACS 160 μm data are also part of the modified blackbody fit (as in Chapter 3), however, the quiescent clump has an exceptionally cold temperature and relatively low column density, such that the PACS 160 μm point is lower than the background (this happens in less than $\sim$5% of pixels) and so that point is not included. The fits are very similar both qualitatively and quantitatively with and without the PACS 160 μm point.

The modified blackbody fits are performed on data that has had the cirrus foreground subtracted using an iterative routine discussed in detail in Chapter 3. The modified blackbody fits assume a spectral index, β, of 1.75, a gas to dust ratio of 100, a mean molecular weight of 2.8 (e.g., Kauffmann et al. 2008), and the Ossenkopf & Henning (1994) MRN distribution model with thin ice mantles that have coagulated at 10^6 cm^{-3} for 10^5 years for the dust opacity. The cirrus foreground removal and modified blackbody fits are discussed in their entirety in Chapter 3.

4.2.2.2 Bolocam Galactic Plane Survey

We utilize the 1.1 mm dust continuum emission from the Bolocam Galactic Plane Survey (BGPS, Aguirre et al. 2011; Rosolowsky et al. 2010) to estimate the isothermal column densities. We derive column density maps at 33$''$ resolution assuming the dust temperature from the corresponding

pixel in Hi-GAL. The column density is given by

$$N(H_2) = \frac{S_\nu}{\Omega_B \kappa_\nu B_\nu(T) \mu_{H_2} m_H} \tag{4.1}$$

$$N(H_2)_{1.1mm} = 2.20 \times 10^{22} (e^{13.0/T} - 1) S_\nu \text{ cm}^{-2} \tag{4.2}$$

where S_ν is the source flux (in Jy in Eq. 4.2), B_ν(T) is the Planck function at dust temperature T, Ω_B is the beam size, and μ_{H_2} is the mean molecular weight for which we adopt a value of μ_{H_2} = 2.8 (Kauffmann et al. 2008). Additionally, we adopt a value of $\kappa_{1.1mm} = 0.0114$ cm^2 g^{-1} from Enoch et al. (2006), in which we have assumed a gas-to-dust ratio of 100. This opacity is consistent with the Ossenkopf & Henning (1994) model used for the 8 μm opacity in the extinction masses as well as the opacity used for the Hi-GAL column densities. We use the dust temperatures derived from Hi-GAL in each pixel above in the calculation of the column densities. One could perform a similar analysis using data from the APEX Telescope Large Area Survey of the Galaxy at 870 μm(ATLASGAL; Schuller et al. 2009).

4.2.3 Extinction Column Density

Dense clumps of dust and molecular gas will absorb the bright mid-IR Galactic background and appear as dark extinction features in the mid-IR (e.g., Carey et al. 1998; Egan et al. 1998; Peretto & Fuller 2009). We use data from the Galactic Mid-Plane Survey Extraordinaire (GLIMPSE; Benjamin et al. 2003) to derive column density maps from the extinction of the dense clumps at 8 μm at 2$''$ resolution. The extinction mass and column density are calculated using the Butler & Tan (2009) method with the correction as applied in Battersby et al. (2010). However, we (as did Battersby et al. 2010) use a dust opacity ($\kappa_{8\mu\text{m}} = 11.7$ cm^2 g^{-1}) from the Ossenkopf & Henning (1994) model of thin ice mantles that have undergone coagulation for 10^5 years at a density of n_{H_2} $\sim 10^6$ cm^{-3}, which is a reasonable model for the cold, dense environment of an IRDC. This and the assumption of a gas-to-dust ratio of 100 is consistent with the opacity used for our dust emission column density estimate. This method relies on an 8 μm emission model of the Galaxy and then uses the cloud distance to solve the radiative transfer equation for cloud optical depth. We com-

pare this estimate with that derived using the Peretto & Fuller (2009) extinction column density method. The Peretto & Fuller (2009) method assumes that most of the observed 8 μm emission is local to the cloud, so a distance is not required. For this particular source, the column densities derived using the Peretto & Fuller (2009) method are about 15% higher than the Butler & Tan (2009) method, with very little scatter. We use the Butler & Tan (2009) method for the remainder of the discussion.

4.2.4 GRS ^{13}CO Column Density

We utilize data taken as part of the Boston University Five College Radio Astronomy Observatory (BU-FCRAO GRS or just GRS, Jackson et al. 2006) of the ^{13}CO J=1-0 transition at 46″ resolution to calculate a column density assuming a gas temperature from the corresponding pixel in the NH_3 gas temperature map. In the optically thin, thermalized limit, the H_2 column density derived from ^{13}CO is given by

$$N(H_2) = \frac{8\pi k\nu^3 X_{^{13}CO}}{3c^3 h B_J A_{10}} (1 - e^{-h\nu/kT_{ex}})^{-1} \int T_{mb}\, dv \tag{4.3}$$

where ν is the frequency of the ^{13}CO J=1-0 transition, A_{10} is the Einstein A coefficient of ^{13}CO from state J=1 to J=0, T_{ex} is the excitation temperature, B_J is the rotation constant, and $X_{^{13}CO}$ is the abundance fraction of ^{13}CO to H_2. We adopt a value of ^{12}CO / ^{13}CO of 58 from Lucas & Liszt (1998), and a value of ^{12}CO / H_2 of 10^{-4}, a value of 55.101038 GHz for B_J, and standard NIST values for all constants and spectral transition values. This expression then reduces to

$$N(H_2) = 1.45 \times 10^{17} \frac{\int T_{mb}\, dv}{1 - e^{-5.29/T}} \text{ cm}^{-2} \tag{4.4}$$

For more details on the column density estimation from ^{13}CO see §3.5 of Battersby et al. (2010).

4.3 Abundance and the Correlation of N(NH_3) with N(H_2)

An abundance measurement of NH_3 ($\chi_{NH_3} = \frac{N(NH_3)}{N(H_2)}$) can be derived from a comparison of the derived NH_3 column densities to the H_2 column densities from a variety of independent measurements: dust continuum emission, dust extinction, and ^{13}CO line emission. The dust continuum

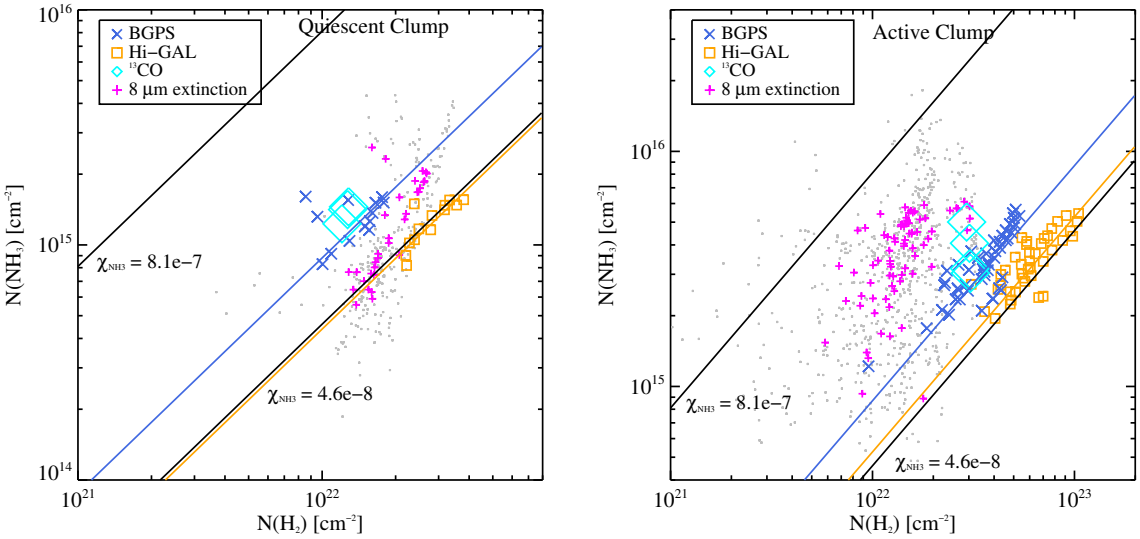

Figure 4.1: The correlation of column densities derived from various independent data-sets vs. the ammonia column density for the abundance calculation. Column densities are derived from Hi-GAL and BGPS 1.1 mm dust continuum emission (using dust temperatures derived from Hi-GAL), ^{13}CO integrated intensity, and 8 μm extinction and plotted on the x-axis against the NH_3 integrated intensity column density on the y-axis. The *left* plot is pixels within the quiescent clump, while the *right* is the active clump. Both dust continuum emission tracers show good correlation with the NH_3 emission, however, with a systematic offset. The 8 μm extinction estimate shows excellent morphological agreement on large scales but the correlation on small scales is highly scattered (gray points show all data, magenta is an average for comparison). The details of these plots are discussed in §4.3. Linear fits are shown for the BGPS (in blue) and Hi-GAL (in orange) points. We also show two abundance lines for comparison, $\chi_{NH_3} = 8.1 \times 10^{-7}$ from Ragan et al. (2011) and $\chi_{NH_3} = 4.6 \times 10^{-8}$ from this work and Pillai et al. (2006).

column densities are derived as described in §4.2.2 using Hi-GAL and BGPS (25″ and 33″ resolution, respectively) with dust temperatures from Hi-GAL (Chapter 3). The dust extinction column density is calculated using 8 μm extinction as described in §4.2.3 with 2″ resolution. We also utilize N(H_2) derived from ^{13}CO (as described in §4.2.4) using the NH_3 gas temperatures, despite ^{13}CO's much lower resolution at 46″.

For a pixel-by-pixel comparison with the NH_3 column density maps in the quiescent and active clump, we convolve and re-grid the higher resolution data (the NH_3 column density maps in all cases except the 8 μm extinction) to match the lower resolution data for each clump. The pixel-by-pixel comparison is shown in Figure 4.1. While there is a good deal of scatter, there also appear to be systematic differences in the column densities derived from the different methods. We comment briefly on the magnitude and possible reasons for these offsets below. These systematic offsets should help to give a flavor for the uncertainties involved in such measurements; Battersby et al. (2010) conclude that typical mass uncertainties using such tracers are about a factor of two neglecting systematic effects such as freeze out.

For each clump and each H_2 tracer we fit a linear using a least-squares Markov Monte-Carlo fitter between N(NH_3) and N(H_2). We assume an approximate error of 50% on each of the column densities (N(NH_3) and N(H_2)). We first fit a line with the zero-point (y-intercept) fixed at zero (the typical method for determining abundances), then fit a line allowing for a non-zero y-intercept. We only include points with N(H_2) between 10^{20} and 10^{24} cm^{-2} which also fit the "mask" criteria applied to all the NH_3 data as described in Chapter 2. We exclude a handful of noisy pixels near the edges of the maps. The results of the fits are shown in Table 4.1.

Hi-GAL: The Hi-GAL column densities show a good correlation with the NH_3 data. The average derived NH_3 abundance is about 4.6 $\times$ 10^{-8}, or with a non-zero y-intercept, about 3.3 $\times$ 10^{-8} with an NH_3 offset of about 3-9 $\times$ 10^{14} cm^{-2}. This offset likely indicates that the abundance relationship is not well described by a single linear abundance for all column densities.

BGPS: The BGPS column densities also show a good correlation with the NH_3 column densities. The average abundance is about 8.6 $\times$ 10^{-8}, or 5.7 $\times$ 10^{-8} with an intercept of about 4

$\times 10^{14}$ cm^{-2}. There is a systematic offset of the BGPS column densities from the Hi-GAL measured column densities of about 1.9, which can be plausibly explained (see §4.3.1).

8 μm dust extinction: The NH_3 and 8 μm dust extinction show excellent morphological agreement (as seen in Chapter 2); the masks created using a column density threshold for each of them are nearly identical. However, comparing their column densities within those masks reveals a great deal of scatter. All the data points are plotted in Figure 4.1 in gray, and their averages (on 15$''$ scales to show less scatter) in magenta. A few interesting things to note: 1) the extinction column densities seem to flatten out or become highly non-linear around N(H_2) $\sim 3.5 \times 10^{22}$ cm^{-2}, 2) the active clump is a bit warmer and has a brighter local 8 μm background which fills in some of the absorption, explaining the low extinction column densities derived in that region, and 3) variations in the NH_3 abundance, 8 μm background, and/or dust opacity are likely responsible for the very large scatter in the extinction column densities. The ratio of extinction to BGPS column densities is about the same as found in Battersby et al. (2010), with a ratio of 0.5 (was 0.7, now 0.5 with the 1.5 correction factor to BGPS) in the active clump and a ratio of about 1.3 (was 2.0, now 1.3 with 1.5 correction factor to BGPS) in the quiescent clump.

GRS: While we wouldn't expect to find a very strong correlation in column density over the few resolution elements the GRS ^{13}CO has over the VLA field of view, the comparison of the overall column densities should be informative. The total column density derived from ^{13}CO GRS is about half that from Hi-GAL and slightly less than the BGPS (about 90%). Whether this indicates CO depletion, optically thick ^{13}CO, or some other physical effect cannot be determined from these data alone.

We adopt the average Hi-GAL derived abundance of $\chi_{NH_3} = 4.6 \times 10^{-8}$ throughout the remainder of this analysis. Since the Hi-GAL column densities are derived simultaneously with the dust temperature, and utilize data at multiple wavelengths to perform full modified blackbody fits, we consider these column densities to be more robust than those determined at a single wavelength with an assumed temperature. We note, however, that BGPS-derived column densities would be less susceptible to gradients in the dust temperature. Additionally, the conditions probed

with the Hi-GAL data (dust continuum emission from cold, dense clumps) are roughly the same conditions probed with NH_3 (dense gas emission from cold, dense clumps), making the Hi-GAL data a reasonable choice for the derivation of NH_3 abundance. We do not see significant evidence of NH_3 depletion. If the difference in the measured Hi-GAL NH_3 abundance between the quiescent and active clump is due to depletion, then the NH_3 is depleted by about 30% in column density in the quiescent clump, see Figure 4.4.

Our measured average abundance, $\chi_{NH_3} = 4.6 \times 10^{-8}$, is very close to that derived by Pillai et al. (2006) in IRDCs.Additionally, Dunham et al. (2011b) studied the abundance of ammonia as a function of Galactocentric radius and found a decrease in abundance of a factor of 7 from a radius of 2 to 10 kpc. Given the Galactocentric radius of the IRDC studied here (4.7 kpc), the relationship determined by Dunham et al. (2011b) predicts an abundance of 4.5×10^{-8}, which is in agreement with the abundance determined in this study and also the recent abundance determination toward this cloud by Chira et al. (2013). One major difference is that Pillai et al. (2006); Dunham et al. (2011b); Chira et al. (2013) use single-dish NH_3 observations of two NH_3 lines, while we use interferometric observations of NH_3 modeled with three lines, all para-NH_3. Our higher resolution observations are probing smaller spatial scales and therefore deriving higher average column densities, however, we are also insensitive to spatial scales above $66''$. The agreement despite the difference in spatial scales probed indicates that both the NH_3 and dust are found preferentially in the densest gas, which is clumpy on scales smaller than our largest angular scale ($66''$). These abundances are also consistent with previous literature values of 3×10^{-8} and 6×10^{-8} from Wang et al. (2008) and 3×10^{-8} from Harju et al. (1993). Our adopted abundance, $\chi_{NH_3} = 4.6 \times 10^{-8}$ is in minor disagreement with the interferometrically derived 8 μm extinction based abundance of 8.1×10^{-7} by Ragan et al. (2011) in IRDCs, but given the large scatter in our extinction-derived abundances (average of 1.1×10^{-7}), the disagreement is not too surprising.

4.3.1 The BGPS and Hi-GAL Discrepancy

In comparing the column densities derived from various datasets, we find a systematic offset of about 1.9 from Hi-GAL to BGPS derived column densities. We suggest that a handful of smaller effects can easily explain this significant offset. Hi-GAL is sensitive to larger spatial scales, and despite the background subtraction, we might still expect slightly lower values in the BGPS due to spatial filtering (perhaps of order 20%). We have checked and confirmed that the difference does not arise from the convolutions, or re-gridding of the data, and that the BGPS data have been multiplied by the correction factor of 1.5 (see Aguirre et al. 2011). While both use the same model for the dust opacity (Ossenkopf & Henning 1994), the power-law fit opacity used for Hi-GAL extrapolated from Ossenkopf & Henning (1994) is slightly higher (0.0135 using a power-law fit and β=1.75 vs. 0.0114, linearly interpolating tabulated values near 1.1 mm, about 1.2 $\times$ higher) at 1.1 mm than the tabulated value used in the BGPS column density. The Hi-GAL procedure required a dust opacity that was a continuous function of frequency so we used a power-law fit to Ossenkopf & Henning (1994) dust opacity rather than the tabulated value. Additionally, the spectral index β may be steeper than the assumed value of 1.75. If we assume that about 20% of the total flux is lost in BGPS due to spatial filtering and use the Hi-GAL power-law extrapolated opacity at 1.1 mm, and assume a spectral index of β slightly steeper than 2 (about 2.25) then we can bring the two column densities into agreement. The large systematic offset can be plausibly explained by a few smaller effects that all push the BGPS column density to lower values. Additionally, the upcoming version 2 BGPS reduction (Ginsburg et al., in prep.) with improved recovery of large-scale structure may shed some light on this discrepancy.

4.4 A Comparison of the Dust and Gas Properties

An understanding of how the physical properties of massive star-forming regions derived from various tracers compare is crucial, especially when only one is available. We present a comparison of Hi-GAL dust-derived temperatures and column densities with those derived from NH_3 observations on the VLA in Figures 4.2 and 4.3 as described in §4.3.

The dust and gas column densities are well correlated for about an order of magnitude. The derived abundance is slightly higher (about 30%) in the active than the quiescent clump (see e.g., Figures 4.2, 4.4), potentially indicating some small amount of depletion. If the differences in derived abundances from the quiescent clump to the active clump is due to depletion of NH_3 onto dust grains, then the average depletion is of order 30% or less, see Figure 4.4.

We estimate volume densities by assuming that the plane-of-the-sky structure sizes are about the same as the line-of-sight structure sizes. We divide both the quiescent and active clump maps into "core" and "filament" pixels and use appropriate plane-of-the-sky structure sizes for each to translate the NH_3 column densities into volume densities. The active cores are about $6''$ (0.16 pc) in diameter while the filament surrounding the active cores is about $10''$ (0.27 pc) in diameter. The quiescent core is about $9''$ (0.24 pc) and its surrounding filament is about $6''$ (0.16 pc) in diameter. These filaments are wider than the universal filament width found in the Gould Belt by Arzoumanian et al. (2011).

The estimated volume densities are plotted versus the gas to dust temperature ratio in Figure 4.3, as well as with the boxed symbols in Figure 4.2. The gas and dust are expected to be coupled above about $10^{4.5}$ or 10^5 cm^{-3} (Goldsmith 2001). The dust and gas temperatures agree reasonably well (within about 20%) above n=10^5 cm^{-3}, however the scatter in the temperature ratio does not show any dependence on derived density. We note that the average densities for the quiescent clump are lower, and typically near or below the threshold density for gas and dust to be coupled.

While the dust and gas temperature agree within about 20% in the active clump, the dust and gas temperatures seem completely uncorrelated in the quiescent clump. We suggest that the dust

Table 4.1: Abundance Measurements

Comparison of N(NH_3) with N(H_2) from	χ_{NH_3} [a,b]	χ_{NH_3} with offset [c,b]	NH_3 Offset [b,d] cm^{-2}
Quiescent Clump			
Hi-GAL	4.0e-8 ± 0.2e-8	3.0e-8 ± 0.7e-8	3e14 ± 2e14
BGPS	8.6e-8 ± 0.8e-8	3.9e-8 ± 0.7e-8	4.8e14 ± 0.7e14
8 μm extinction	4.64e-8 ± 0.09e-8	9.3e-8 ± 0.4e-8	-7.4e14 ± 0.7e14
GRS ^{13}CO	9.5e-8 ± 0.2e-8	1.9e-7 ± 0.6e-8	-1.2e15 ± 0.8e15
Active Clump			
Hi-GAL	5.3e-8 ± 0.2e-8	3.6e-8 ± 0.6e-8	9e14 ± 3e14
BGPS	8.7e-8 ± 0.3e-8	7.5e-8 ± 0.8e-8	4e14 ± 2e14
8 μm extinction	2.19e-7 ± 0.04e-7	2.46e-7 ± 0.08e-7	-2.3e14 ± 0.7e14
GRS ^{13}CO	1.1e-7 ± 0.2e-7	-1.8e-6 ± 0.6e-6	6e16 ± 2e16

[a] NH_3 Abundance: Linear fit to data without a y-intercept.
[b] Assuming a column density error of 20%.
[c] NH_3 Abundance: Linear fit to data with a y-intercept.
[d] NH_3 Column Density Offset: y-intercept of the fit to the abundance.

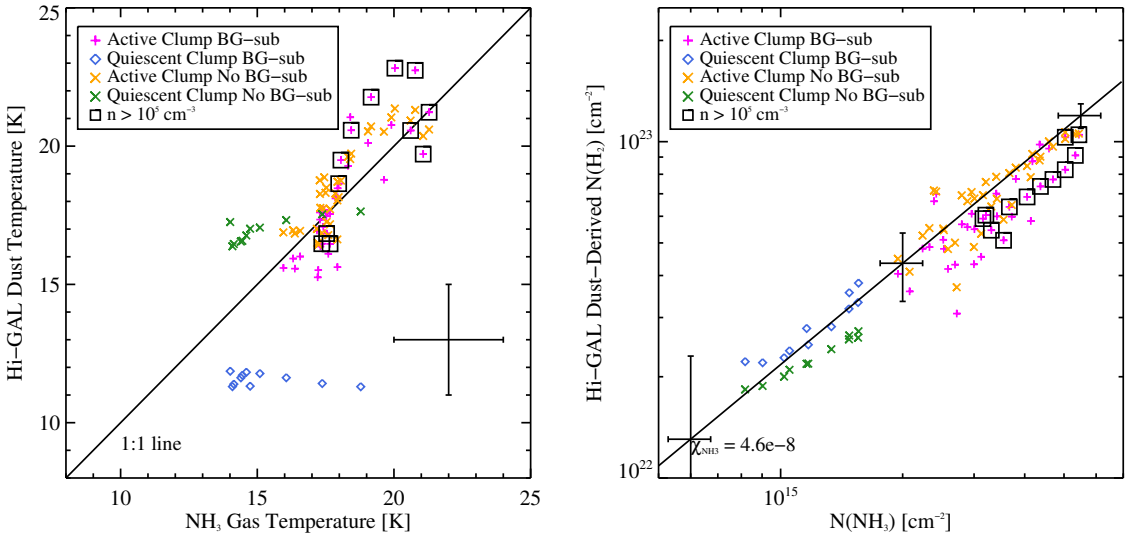

Figure 4.2: A comparison of the Hi-GAL dust-derived temperatures and column densities with those derived from NH_3 on the VLA shows good correlation except for the gas and dust temperatures in the quiescent clump. The magenta and blue points show the active and quiescent clump pixels, respectively, which have had the background subtracted and have been used throughout the text, while the orange and green points show the active and quiescent clump pixels, respectively, which have not had the background subtracted for comparison. *Left:* The dust vs. gas temperature for both clumps. The two show reasonable correlation, though with much scatter, for the active clump and ***no*** correlation for the quiescent clump. A typical model fit error bar (2 K in both T_{dust} and T_{gas} is shown in the bottom right). See the discussion in §4.4. *Right:* The column densities are reasonably well-correlated over a wide range. A typical model fit error bar (10% in $N(NH_3)$, 1×10^{22} cm^{-2} in $N(H_2)$ is shown at three points throughout the plot (to give a sense of errors in the log-log plot).

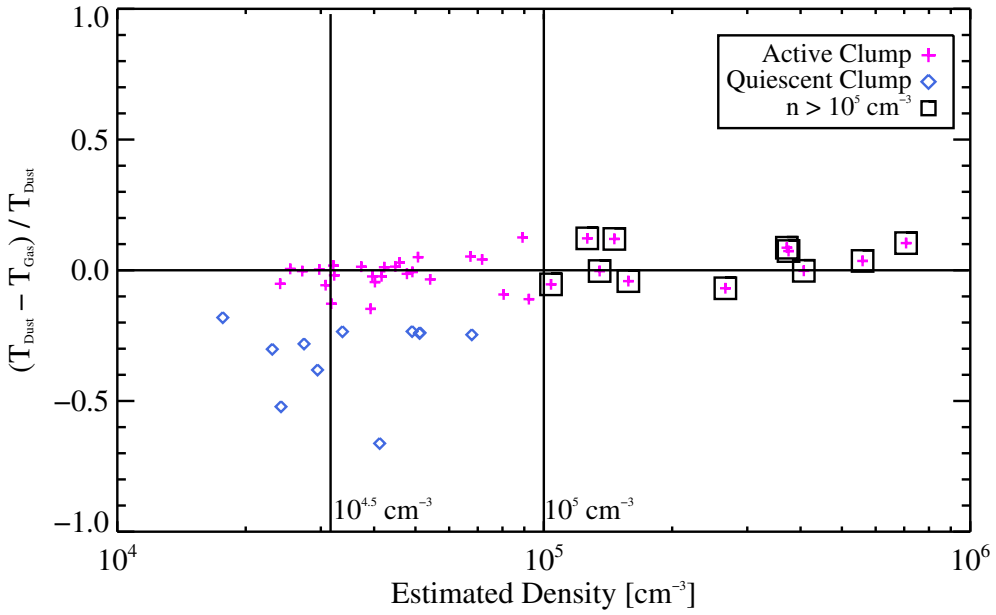

Figure 4.3: Estimated volume densities plotted against the fractional difference between the Hi-GAL dust and NH_3 gas temperatures. This plot agrees well with the cluster-scale simulation of a star-forming region by Martel et al. (2012) at a time-step of about 0.5 Myr. The volume densities are estimated as in §4.4. Two vertical lines at n=$10^{4.5}$ and 10^5 cm^{-3} are plotted to indicate typical densities above which the dust and gas are coupled. The dust and gas are in decent agreement (within about 20%) in the active clump, however show disagreement in the quiescent clump, which may indicate a lack of dust/gas coupling or the limits of the dust temperature derivation algorithm in this regime.

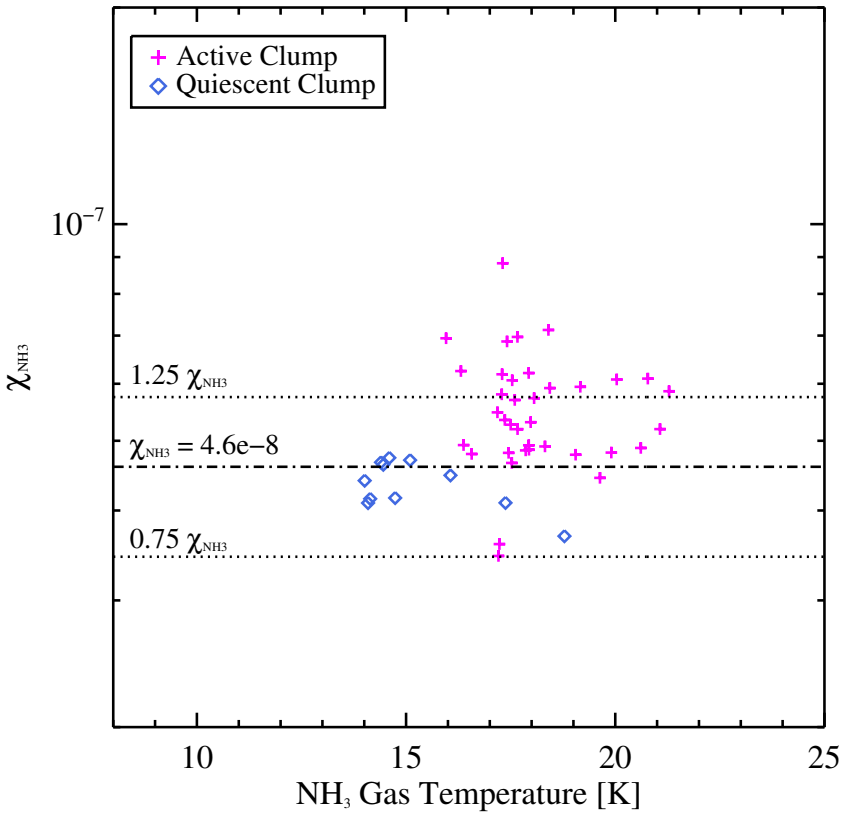

Figure 4.4: A plot depicting the potential effect of depletion in the quiescent clump, which we estimate to be of order 30% or less. This plot shows the ratio of N(NH_3) to Hi-GAL N(H_2) for each point in the clumps (active in magenta crosses, quiescent in blue diamonds) vs. the associated NH_3 gas temperature. We adopt an abundance of $\chi_{NH_3} = 4.6 \times 10^{-8}$, and we see that most of the active clump points fall at slightly higher abundances and temperatures while the points in the quiescent clump are generally colder and have a slightly lower derived abundance.

and gas are not well-coupled in the quiescent clump and that the dust can cool more efficiently than the gas and so is at a uniformly low temperature, while the gas temperature is higher and variable with location. Additionally, this indicates that the interplay between gas and dust heating/cooling is not simple in these young star-forming clumps, even at $10^{4.5}$ cm^{-3}. Alternatively, this offset could be explained if the gas and dust tracers are probing different layers, though we think this is unlikely due to the high critical density of NH_3 and the fact that the interior (as probed more effectively by NH_3) should be cooler in the quiescent clump than the exterior (as probed by dust emission). It should be noted that the absolute agreement in the quiescent clump is better (they agree within about 20%) if the Hi-GAL background is not subtracted (see Figure 4.2), however, the dust temperature variation is equally flat with changing gas temperature. This analysis should be re-examined in a region where the Hi-GAL background is less significant, as we may be probing a regime in which the background subtracted modified blackbody fits break down.

The dust and gas temperature vs. density plotted in Figure 4.3 shows remarkable similarity to the youngest instance (about 1.6 of the cloud free-fall collapse time or 0.5 Myr) of the simulated cluster-forming region of Martel et al. (2012) (top left of their Figure 8). The dust and gas temperatures were calculated individually in this SPH simulation of a cluster-scale ($\sim$ 1 pc, 1000 M$_\odot$) star-forming region. Just when the gas clump has begun to form a few stars (about 1.6 t_{ff} or 0.5 Myr), the dust is very cold, as it has not yet been significantly heated by the forming stars, while the gas is slightly warmer due to heating from cosmic rays. The agreement of our observations with this simulation suggests the importance of simulating gas and dust temperatures separately, especially at early times and densities n $< 10^5$ cm^{-3}. This agreement lends some support for a lifetime for the currently observed and previously existing IRDC phase of order 0.5 Myr (similar to the 0.6 - 1.2 Myr starless lifetime found in Chapter 5).

4.5 Comparison with the Single-Dish GBT Data

The gas temperatures and column densities found here agree with the single-dish GBT results found by Dunham et al. (2011b) in a survey of NH_3 toward BGPS clumps. The VLA results

presented here have a resolution roughly 10 times better than the BGPS, and are able to detect smaller, higher density regions within the large-scale BGPS clump.

In the quiescent clump, the VLA observations returned a gas kinetic temperature of 8-15 K for the filament and 13 K for both the Main (Core 1) and Secondary cores (Cores 2, 3, and 4). The single-dish data in this region centered on the peak of BGPS source number 4901, which is very close to Core 1 in the VLA data. The single-dish data returned a gas kinetic temperature of 14.9 K, which is slightly warmer than the VLA data because the GBT beam also included a significant amount of the surrounding warmer filament gas within the 31 arcsec beam.

In the active clump, the hot core and cold core complexes, as well as the UCHII region all fall within a single BGPS source (number 4916). In particular, the hot core complex corresponds to the position of the single-dish data. The single-dish gas temperature is slightly lower than the VLA-derived gas temperature (30.4 K and 35-40 K, respectively). This difference can be explained in the same way as the difference in the quiescent clump: the single-dish observations include some of the surrounding cooler gas which lowers the derived kinetic temperature. Although the exact numbers differ between this study and the single-dish study, the results are consistent. This comparison highlights the hierarchical nature of star formation, showing increasing complexity and sub-structure down to our resolution limit.

4.6 The High-Resolution Origin of Sub-mm Clump Emission

The high-resolution NH_3 data from the VLA allows the unique opportunity to explore the properties of dense gas on sub-pc scales. The Bolocam Galactic Plane Survey (BGPS) on the other hand allows for an investigation of these properties across the Galaxy, but on $\gtrsim 1$ pc scales ($33''$ resolution corresponds to clumps on the near side of the Galaxy or whole clouds on the far side). A comparison of this high resolution NH_3 data with large-scale BGPS data allows an opportunity to address the small-scale origin of the millimeter flux.

In this particular IRDC, the contribution of free-free emission to the millimeter flux is negligible (Chapter 2), as the only radio continuum source (G32.03 + 0.05) observed at 1, 6 and 20 cm is

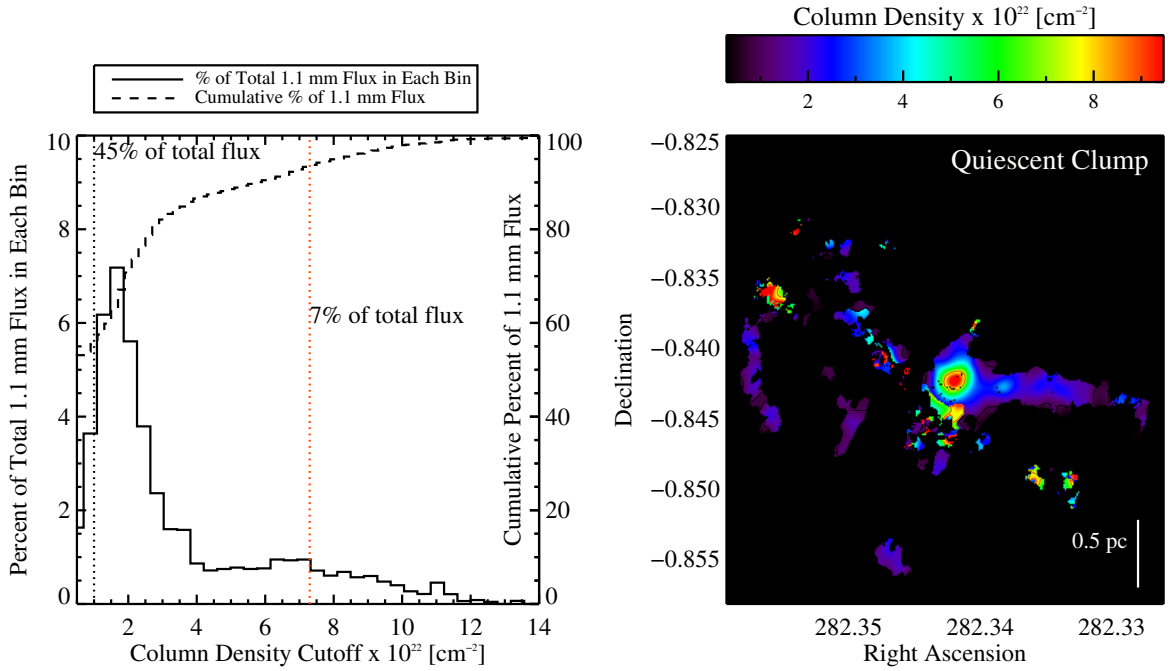

Figure 4.5: A depiction of the origin of the simulated 1.1 mm BGPS flux (see text §4.6) in the quiescent clump. The plot on the left shows the fractional (solid) and cumulative (dashed) distribution of 1.1 mm flux as a function of column density. A few lines are shown for reference at [1, 7.3, 21] $\times$ 10^{22} cm^{-2} (black, orange, purple, see text §4.6). The image on the right shows the column density map with contours at the reference column densities in corresponding colors. In the quiescent clump 55% of the total 1.1 mm flux is below N(H_2) = 1 $\times$ 10^{22} cm^{-2} and is filtered out by the interferometer, while 45% of the flux comes from dense filaments (black dotted line, N(H_2) $>$ 1 $\times$ 10^{22} cm^{-2}), 7% of the flux arises from massive star forming cores (orange dotted line, N(H_2) $>$ 7.3 $\times$ 10^{22} cm^{-2}, Kauffmann & Pillai 2010), and 0% of the flux arises from cores above the theoretical threshold for forming massive stars (purple dotted line in Figure 4.6 not shown here, N(H_2) $>$ 21 $\times$ 10^{22} cm^{-2}, Krumholz & McKee 2008).

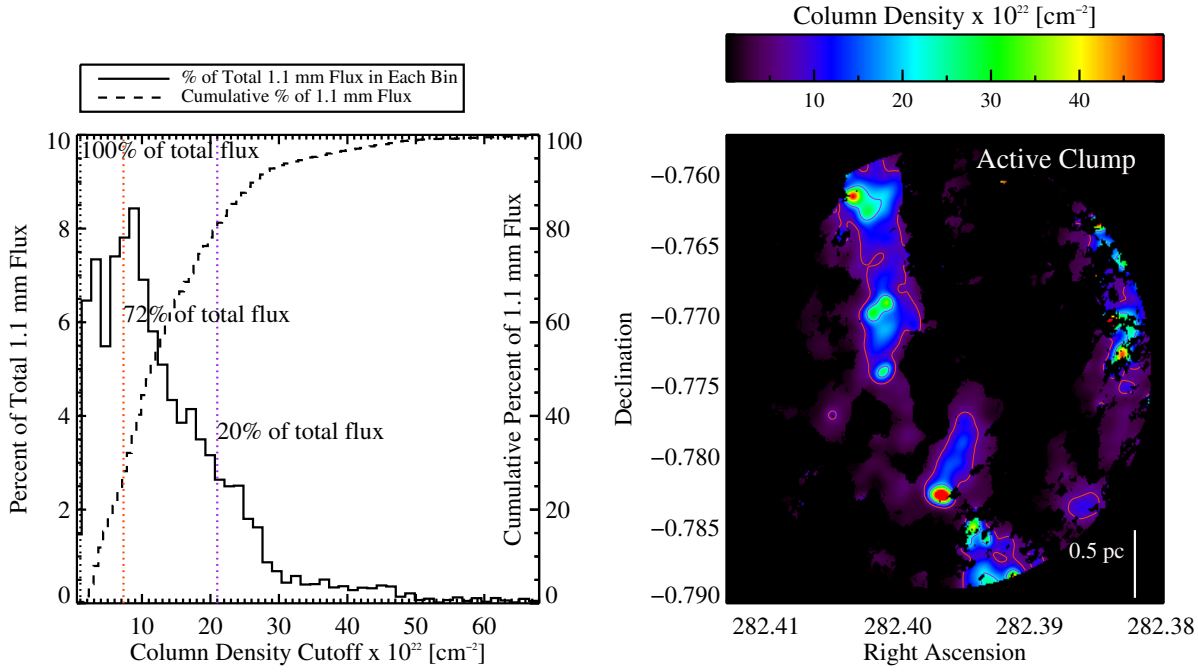

Figure 4.6: Same as Figure 4.5, but for the active clump. A depiction of the origin of the simulated 1.1 mm BGPS flux (see text §4.6). In the active clump none of the emission has been filtered out (simulated 1.1 mm BGPS flux is consistent with total real 1.1 mm BGPS flux), meaning that 100% of the flux originates from dense filaments (black dotted line), 72% from massive star forming cores (orange dotted line, $N(H_2) > 7.3 \times 10^{22}$ cm^{-2}, Kauffmann & Pillai 2010), and 20% from the densest cores (purple dotted line, $N(H_2) > 21 \times 10^{22}$ cm^{-2}, Krumholz & McKee 2008).

not coincident with the millimeter emission; the source is evolved enough to have blown out most of the dense gas and dust. In order to determine the relative contributions of the cores and filaments to the millimeter flux, we invert Eq 4.2 in §4.2.2, the equation to derive the dust column density from millimeter flux, and solve it for the millimeter flux using the column density and temperature maps derived from the NH_3 data. This gives us a simulated map of 1.1 mm flux on sub-pc scales. This, of course, assumes a tight coupling between the dense gas and dust. If the gas and dust are less well-coupled, especially in the lower density filaments, then we are overestimating the flux from the filament (because the dust would be colder than we are assuming), and a higher fraction of the millimeter emission arises from the dense gas cores.

In Figures 4.5 and 4.6 we measure what structures are responsible for the observed pc-scale sub-mm emission observed at 1.1 mm with the BGPS. We compare the simulated (forward-modeled) 1.1 mm flux with the real 1.1 mm BGPS flux and find that in the quiescent clump, about 55% of the global BGPS flux is filtered out by the interferometer / masking, meaning that only about 45% of the sub-mm flux arises from dense filaments with $N(H_2) > 10^{22}$ cm^{-2}. In the active clump, the gas is more compact and all of it appears to arise from structures with $N(H_2) > 10^{22}$ cm^{-2} (i.e. the simulated sub-pc 1.1 mm flux matches the real pc-scale 1.1 mm flux). About 7% vs. 72% of the total 1.1 mm flux arises from massive star-forming dense cores for the quiescent and active clumps respectively, where massive star-forming cores refers to being above the massive star-forming threshold from Kauffmann & Pillai (2010) which corresponds very roughly to $N(H_2) > 7.3 \times 10^{22}$ cm^{-2} for one resolution element in our maps. About 0% vs. 20% of the total 1.1 mm flux arises from the densest cores with $\Sigma > 1$ g cm^{-2} in the quiescent and active clumps respectively, the theoretical threshold for the formation of massive stars from Krumholz & McKee (2008), corresponding to about $N(H_2) > 21 \times 10^{22}$ cm^{-2}.

In summary, sub-mm BGPS clumps show a variety of sub-pc structure and the origin of 1.1 mm emission can be from diffuse clumps, dense filaments, and massive star-forming cores. In some clumps (like the quiescent clump), over 50% of the flux arises from the diffuse clump, about 40% from the dense filament, and only about 10% from massive star-forming cores. In other clumps

(like the active clump), all of the sub-mm flux arises from dense filamentary structures with N(H_2) $> 10^{22}$ cm^{-2} and about 75% from massive star-forming cores, in a range of evolutionary states. Sub-mm dust clumps probe a range of density structures and star-forming evolutionary states.

4.7 Conclusion

We explore the relationship between dust and gas derived physical properties in a massive star-forming IRDC, G32.03 + 0.05 showing a range of evolutionary states. The gas properties (temperature and column density) were derived using radiative transfer modeling of three inversion transitions of NH_3 on the VLA, while the dust properties (temperature and column density) were derived with cirrus-subtracted modified blackbody fits to Herschel data. We derive an NH_3 abundance and compare different tracers of column density (dust emission and extinction and gas emission). The gas and dust temperatures agree well in the active clump, but the disagreement in the quiescent clump calls into question either the reliability of dust temperatures in this regime or the assumption of tight gas and dust coupling. We also explore the high-resolution ($\sim$ 0.1 pc) origin of pc-scale dust emission by forward modeling the gas temperature and column densities to derive 1.1 mm fluxes and comparing with the observed BGPS 1.1 mm fluxes.

- ***NH_3 Abundance:*** A comparison of the NH_3 column density with those derived from various independent tracers exemplifies some of the uncertainties involved in such measurements, as the systematic variations between these tracers is about a factor of two. The Hi-GAL dust continuum data show a good correlation with the NH_3 from which we derive an abundance of $\chi_{NH_3} = 4.6 \times 10^{-8}$, in agreement with previous single-dish observations. This agreement indicates that both the gas and dust are clumpy on scales smaller than about 60″ (the largest angular size to which our NH_3 observations are sensitive).

- ***Gas and Dust Coupling:*** The gas and dust column densities show good agreement. Depletion of NH_3 in the quiescent clump is of order 30% or less. The dust and gas temperatures are scattered, but agree reasonably well for the active clump (within about 20%).

The quiescent clump, however, shows no correlation between dust and gas temperature. In this regime, the two may not be well-coupled, or we may be probing a regime in which the dust or NH_3 temperature estimates break down. A comparison of these temperatures with densities agrees well with a cluster-scale star formation simulation(Martel et al. 2012) just before the stars begin to turn on (about 0.5 Myr). The disagreement of gas and dust temperatures at early times (and the agreement with the simulation where dust and gas temperatures are calculated separately) suggests the importance of simulating the gas and dust heating and cooling processes individually in young star-forming regions.

- ***The Origin of Dust Continuum Emission:*** Forward modeling of the NH_3 data (temperatures and column densities) to produce millimeter fluxes and comparing these with BGPS millimeter fluxes reveals that millimeter dust continuum observations, such as the BGPS, Hi-GAL, and ATLASGAL, probe hot cores, cold cores, as well as the dense filaments from which they form. The millimeter flux is not dominated by a single hot core, but rather, is representative of the cold, dense gas as well. The quiescent clump is dominated by diffuse flux filtered out by the interferometer (about 55%) and the cold, dense filament (about 45%). Only about 7% of the total 1.1 mm flux arises from massive star-forming cores in the quiescent clump. The active clump is dominated by high density gas, both hot and cold, in the form of dense filaments (100% of the flux from material with $N(H_2) > 10^{22}$ cm^{-2}) and massive star-forming cores (72% of the flux from massive star-forming cores; $N(H_2) > 7.3 \times 10^{22}$ cm^{-2} and 20% from material with $N(H_2) > 2.1 \times 10^{23}$ cm^{-2}).

Chapter 5

The Lifetimes of Phases in Massive Star Forming Regions

The relative lifetime of phases in the formation of massive stars and stellar clusters is important in distinguishing theories of their formation mechanisms. Whether dense clumps in Giant Molecular Clouds collapse slowly and globally, or if dynamic, fast, large-scale accretion flows are the origin of clustered massive star-forming regions is still a question of great debate. In this letter, we report on the observed relative (and absolute assuming a 6.7 GHz CH_3OH maser lifetime) lifetimes of three major evolutionary phases in clustered massive star-forming regions. We report that the cold, dense, infrared-dark phase has a relative lifetime of $\sim$ 70% (0.6 - 1.2 Myr), while the 6.7 GHz CH_3OH maser phase has a relative lifetime of $\sim$ 2-4% (35,000 years), and the warm, infrared-bright phase has a relatively lifetime of $\sim$ 30% (0.3 - 0.5 Myr). The relative lifetimes of the starless vs. star-forming phases are robustly determined, while the absolute lifetime determinations from the maser lifetime are more tenuous and will benefit from further, higher resolution analyses. We find that 6.7 GHz Class II CH_3OH masers tend to be found at the intersection of starless and star-forming High Surface Density (HiSD) regions, indicating that they exist for a short period of time just when a massive star turns on.

5.1 Introduction

Massive stars dominate the life cycle of gas and dust in our Galaxy, driving the dynamics in the interstellar medium and lighting up the universe around us. The transition of Giant Molecular Clouds (GMCs) into massive stars and stellar clusters is fundamentally important to our under-

standing of the global process of star formation, the origin of the Initial Mass Function (IMF), planet formation in star clusters, and star formation rates in nearby galaxies. We have yet to fully understand the formation mechanism, early evolution, and lifetimes of massive star-forming regions and this quest remains a cornerstone of modern astrophysics. Whether star clusters and massive star-forming regions form as the result of slow, equilibrium global collapse of clumps (e.g., Tan et al. 2006) over several free fall times or if they collapse quickly on the order of a free-fall time (e.g., Elmegreen 2000, 2007; Hartmann & Burkert 2007), perhaps through large scale accretion along filaments (Myers 2009), remains an open question.

In order to study the formation mechanism, early evolution, and lifetimes of massive star-forming regions, we seek the earliest phases of massive star formation. Young, embedded clusters have high densities (10^4 - 10^7 cm^{-3}), sizes of about 0.5 - 1 pc radii, temperatures of 50-200 K, and masses $\gtrsim$ 100 M$_\odot$ (Lada & Lada 2003). We expect the precursors to these clusters to have similar properties, except that they ought to be colder. Hence, searches for these young, massive star-forming regions are typically targeted toward longer wavelengths where the dust continuum peaks for these cold, dense clumps (e.g., BGPS, ATLASGAL, Hi-GAL, Aguirre et al. 2011; Schuller et al. 2009; Molinari et al. 2010). These cold dense clumps can also be seen as Infrared Dark Clouds (IRDCs, Egan et al. 1998; Perault et al. 1996; Omont et al. 2003), absorbing the diffuse Galactic mid-IR light behind them, appearing as dark features in the mid-IR. Due to their cold temperatures (T $<$ 20 K, Pillai et al. 2006) and high densities ($>$ 10^5 cm^{-3}) the most massive of these (M $>$ 10^3 M$_\odot$) are commonly cited as the birthplaces for massive stars and stellar clusters (e.g., Rathborne et al. 2006; Beuther et al. 2007a; Parsons et al. 2009; Battersby et al. 2010), yet not all IRDCs will form massive stars (Kauffmann & Pillai 2010). Additionally, the selection of IRDCs is inherently biased by the fact that their identification requires that they be on the near-side of a bright-mid-IR background.

In Chapter 3, we showed that the physical properties of dust continuum clumps (temperature and column density) can be used to distinguish the pre-star-forming and actively star-forming populations, independent of whether or not they are dark in the mid-IR. We utilize these physical

properties in this work to study a sample of massive star-forming regions and determine the relative populations in the starless and star-forming phase. Unlike other similar analyses (e.g., Chambers et al. 2009; Miettinen 2012; Wilcock et al. 2012; Tackenberg et al. 2012; Parsons et al. 2009, discussed in §5.3.3), we analyze all the pixels above a massive star-forming threshold (which we call High-Surface Density Regions, HiSD regions), independent of their association into 'clumps' or 'cores,' as many times a single clump can contain both actively star-forming and quiescent regions. Additionally, our analysis is not targeted toward IRDCs but to all dust continuum pixels above a massive star-forming threshold (HiSD regions) and we use the source temperatures in addition to their mid-IR signature to determine their star forming activity.

In §5.2, we discuss the derivation of dust temperatures and column densities, the massive star forming threshold implemented, the distinction between starless and star-forming, and the association with 6.7 GHz CH_3OH masers. In §5.3 we present our derived relative and absolute lifetime estimates, comparison with other estimates of massive star forming lifetimes, and a discussion of our uncertainties. We conclude in §5.4.

5.2 Method

Using data from the Herschel Infrared Galactic Plane Survey (Molinari et al. 2010, Hi-GAL), the Spitzer legacy project GLIMPSE (Benjamin et al. 2003), and complete, unbiased surveys for 6.7 GHz CH_3OH masers (Pestalozzi et al. 2005), we search a $2^o \times 2^o$ field centered at [l,b] = [30^o, 0^o] for the relative fraction of sources above a column density threshold for forming massive stars in the starless versus star-forming phase. We use the relative fraction to infer lifetimes. In order to robustly determine these lifetimes, we utilize two identification methods for starless and star-forming HiSD regions, a 'generous' and a 'conservative' method. The column densities and dust temperatures we use are determined from modified blackbody fits to background-subtracted Hi-GAL data from 160 to 500 μm, as in Chapter 3. The identification of starless vs. star-forming HiSD regions is based on the approach from Chapter 3 and uses the HiSD region temperature and signature at 8 μm to determine whether it is starless or star-forming, the details of which are

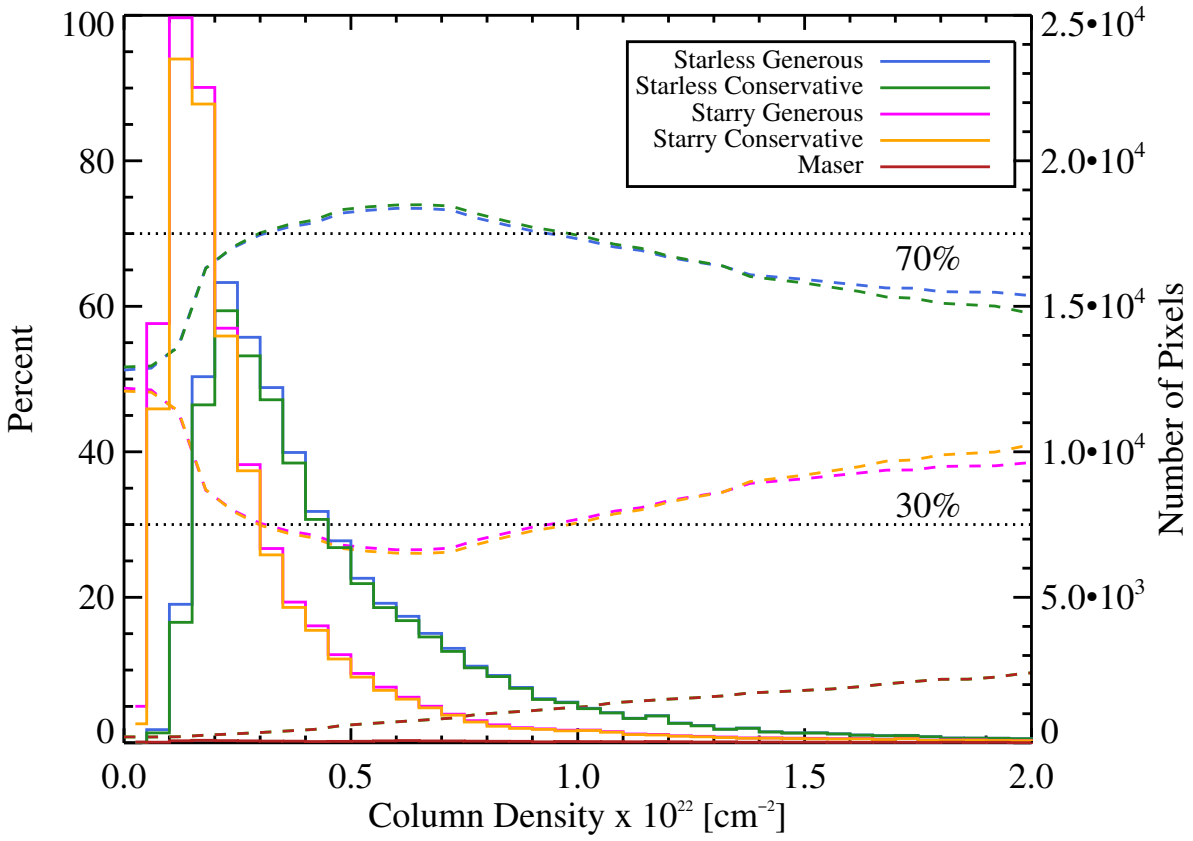

Figure 5.1: The relative fraction of pixels which are starless (70%) vs. star-forming (30%) is mostly insensitive to column density cutoff over a reasonable range of thresholds ($N(H_2) \sim 0.3$ - 1.3×10^{22} cm^{-2}). The left y-axis and dashed lines show the relative percentage of pixels which are starless (cyan and green using the generous and conservative identification methods respectively) vs. star-forming (magenta and orange using the generous and conservative identification methods respectively) or which contain a maser (red) as a function of the column density threshold selected. The right y-axis and solid lines show the column density distribution of the same populations.

described in §5.2.2. All of the data used are convolved to a common resolution of 25″.

We first select pixels above a column density threshold for forming massive stars (HiSD regions), as described in §5.2.1. Next, we identify each HiSD region as starless or star-forming as in §5.2.2. From the relative fraction of HiSD regions capable of forming massive stars in the starless vs. star-forming phase, we determine the relative lifetimes of each phase. Above our column density threshold, we also search for 6.7 GHz Class II CH_3OH masers from the unbiased searches by Szymczak et al. (2002) and Ellingsen (1996), as described in §5.2.3. Using the relative fraction of HiSD regions containing 6.7 GHz masers and their absolute lifetime of 35,000 years from the literature (van der Walt 2005), we determine some range of absolute lifetimes for each phase.

5.2.1 Column Density Threshold for Forming Massive Stars

The predicted theoretical criterion for forming massive stars is a surface density, $\Sigma \sim 1$ g cm^{-2} (Krumholz & McKee 2008), which corresponds to a column density, N(H_2) $\sim 2.1\times10^{23}$ cm^{-2}. However, at distances of several kpc observed with a 25″resolution beam, most cores are highly beam-diluted. In an attempt to derive a realistic massive star-forming column density threshold for beam-diluted sources, we model a core with a peak core density corresponding to $\Sigma = 1$ g cm^{-2}, place it at typical source distances toward $\ell = 30^o$, integrate along the line of sight to get column density, convolve the core to 25″resolution, and take the peak column density of the beam-diluted core to be our column density threshold. We assume a spherical core with a flat peak central density out to a radius r_f which then falls off as r^{-p}, where p is the density power-law exponent, in following form:

$$n(r) = n_f(r/r_f)^{-p} \tag{5.1}$$

We use the best-fit central core radius, $r_f = 1000$ AU, and density power-law index, p = 1.8, from the Mueller et al. (2002) study of 51 massive star-forming cores. For a peak central density, we use $n_f = 6.2 \times 10^7$ cm^{-3}, which integrated over $r_f = 1000$ AU, corresponds to the theoretical surface density threshold for forming massive stars of $\Sigma = 1$ g cm^{-2}.

At typical distances of 5.5 and 9 kpc toward the $\ell = 30^o$ field (Ellsworth-Bowers et al., in

prep.) a 25″beam corresponds to 0.7 and 1.1 pc. Placing our model core at these distances and convolving it with a 25″beam results in column density cutoffs of $N(H_2) = 0.8$ and 0.4×10^{22} cm^{-2}, respectively. Figure 5.1 demonstrates that the relative lifetimes we derive are relatively insensitive within reasonable column density thresholds (∼0.3 to 1.3 × 10^{22} cm^{-2}, corresponding to distances of 11 and 3 kpc). We adopt two cutoffs for our determination of relative lifetimes, the lower of which ($N(H_2) = 0.4 \times 10^{22}$ cm^{-2}) we call our 'generous' cutoff, while the higher ($N(H_2) = 0.8 \times 10^{22}$ cm^{-2}) is our 'conservative' cutoff. For the remainder of the paper, we call pixels above this column density threshold for forming massive stars, High-Surface Density Regions (HiSD regions). It is worth noting that these images have already had a significant Galactic cirrus emission component subtracted (of order $N(H_2) = 10^{22}$ cm^{-2}) as described in Chapter 3.

5.2.2 Starless vs. Star-Forming

In Chapter 3 we found that Herschel dust continuum sources can be separated out into starless and star-forming based on their star-forming signatures and that the starless and star-forming clumps have significantly different distributions of dust temperatures. We utilize these dust temperature distributions in combination with each HiSD region's mid-IR star-forming signature to identify each HiSD region as starless or star-forming. In this work, we are only sensitive to star-forming signatures of massive stars. Therefore, the term "starless" refers only to a HiSD region's lack of massive star-forming signatures and could be hosting active low-mass star formation.

Above the column density threshold for forming massive stars (see §5.2.1) we classify each HiSD region as either starless of star-forming, based on its temperature and signature at 8 μm. A HiSD region can be mid-IR-dark (cold, dense dust absorbing the background 8 μm mid-IR light), mid-IR-neutral (no signature at 8 μm), or mid-IR-bright (likely from UV excited PAH emission in the 8 μm band). Above the column density thresholds, we have reasonable confidence that the mid-IR-dark HiSD regions are starless, while the mid-IR-bright HiSD regions are associated with massive star formation. Therefore, above each column density threshold (generous and conservative, $N(H_2)$ = 0.4 and 0.8 × 10^{22} cm^{-2}, respectively), we fit a Gaussian to the mid-IR-dark and mid-IR-bright

temperature distributions and use these temperature distributions to classify all HiSD regions as starless or star-forming.

As with the column density threshold, we apply two different cutoffs based on the temperature distributions, a 'generous' and 'conservative' cutoff, corresponding to 3 and 2 σ cutoffs, respectively. A HiSD region is classified as starless if it: 1) is mid-IR-dark and falls within 2 (or 3 for the 'generous' cutoff) σ of the mid-IR-dark temperature distribution (Conservative: 11-28 K, Generous: 9-32 K) or 2) is mid-IR-neutral and falls within the same distribution, with an upper limit at 25 K so as not to overlap with the star-forming population. Conversely, a HiSD region is classified as star-forming if it: 1) is mid-IR-bright and falls within 2 (or 3 for the 'generous' cutoff) σ of the mid-IR-bright temperature distribution (Conservative: 21-42 K, Generous: 12-47 K) or 2) is mid-IR-neutral and falls within the same distribution, with a lower limit at 25 K so as not to overlap with the starless population.

5.2.3 Maser Association

The presence of a 6.7 GHz Class II CH_3OH maser must be determined independently of its association with an IR-bright source, so it is important to utilize a survey which is unbiased; we use the Galactic Plane searches by Szymczak et al. (2002) and Ellingsen (1996) as compiled by Pestalozzi et al. (2005). We define the 'size' of the methanol masers sources by a circle with a radius of the positional accuracy RMS of the observations (30″and 36″respectively for Szymczak et al. 2002; Ellingsen 1996). While methanol maser emission comes from very small areas of the sky (e.g., Walsh et al. 1998; Minier et al. 2001), they are often clustered (Szymczak et al. 2002; Ellingsen 1996, find multiple maser spots towards the majority of sources), so these methanol maser "sizes" are meant to represent the extent of the star-forming region. Future higher sensitivity and resolution unbiased searches (e.g., the 6 GHz multi beam maser survey, Green et al. 2009) will certainly improve this characterization.

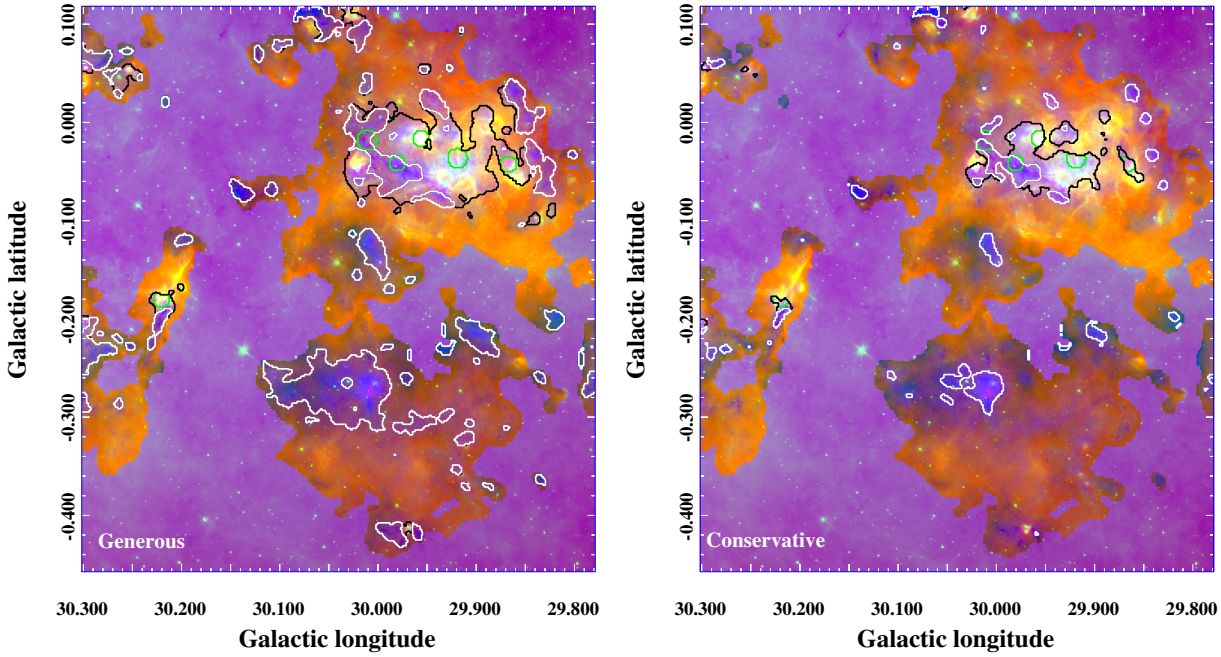

Figure 5.2: Depiction of starless (white contour), star-forming (black contour), and maser (green contour) associated HiSD regions plotted on a three-color image in which red is the temperature, blue is the column density, and green is the 8 μm emission. Predominantly blue regions in this map are starless (cold, high column density, and 8 μm dark or neutral), while predominantly white/purplish regions are star-forming (warm, high column density, and 8μm bright). Red/yellow regions are warm but have low column densities. The 'generous' HiSD region identifications ($N(H_2)$ $> 0.4 \times 10^{22}$ cm^{-2}, 3σ temperature distribution) are depicted on the *left* while the 'conservative' HiSD region identifications ($N(H_2) > 0.8 \times 10^{22}$ cm^{-2}, 2σ temperature distribution) are depicted on the *right*. Both identifications yield relative lifetimes of approximately 70% starless and 30% star-forming, though the associated relative maser lifetime is 2% on the left and 4% on the right. The sharp edges in red and blue are the 'source masks' in the temperature and column density maps (see Chapter 3 for details).

5.3 Lifetimes

5.3.1 Discussion of Uncertainties

In determining the starless and star-forming lifetimes for massive star-forming regions, we have made the following assumptions: i) this sample is complete and unbiased in time and space, ii) each HiSD region represents a region which is forming or will form a massive star, iii) the HiSD regions' lifetime doesn't depend on its mass, iv) star formation rate is constant as a function of time, v) starless and star-forming regions occupy similar areas on the sky (number of pixels), and vi) the signatures at 8 μm (mid-IR bright or dark) and their associated temperature distributions are good indicators of the presence or absence of a massive star. While these assumptions are generally reasonable, many are highly uncertain.

Assumption (i) is reasonable if there has been no large-scale triggering event. The argument for assumption (ii) laid out in §5.2.1 strongly suggests that the majority of HiSD regions (with characteristic density profiles and at typical distances) have the ability to form massive stars, but there are always exceptions and outliers which will break this assumption. This assumption could be improved upon with distance (and hence mass and size) determinations. Assumption (iii) is necessary at this time, but could potentially be removed by a careful separation of sources into mass bins when distances are determined. Assumption (iv) is reasonable over a large enough sample size (similar to assumption (i)) and over these relatively short Myr timescales. Since the column density threshold is the same for starless and star-forming HiSD regions, and there is little variation above that threshold, both should represent equal regions capable of forming massive stars, meaning that assumption (v) is reasonable. Various studies (e.g., Battersby et al. 2010; Chambers et al. 2009; Rathborne et al. 2006) argue in favor of assumption (vi), but more sensitive and higher resolution studies will continue to shed light on the validity of this assumption.

5.3.2 Observed Lifetimes

We find that, in both the 'conservative' and 'generous' cases, the relative fraction of pixels in the starless phase (percent of total pixels) is 70% vs. the relative fraction in the star-forming phase of 30%. This relative fraction is robust over many different variations in the cutoffs selected, see Figure 5.1. Slight changes in the temperature distributions (for example, including all HiSD regions down to 0 K in the starless and up to 100 K in the star-forming case) used also have a negligible effect on this result. The observational result that of the massive star-forming clumps (observed in the cold, dust continuum) observed in the l=30^{o}region, about 70% (by area on the sky) are in the starless (cold, no 8 μm emission) phase and 30% (also by area on the sky) are in the actively star-forming phase (still observed as a dusty clump, but showing emission at 8 μm) is robustly determined. If we make the assumptions discussed in §5.3.1, then we conclude that massive star-forming clumps spend about 70% of their lives in the starless phase and 30% in the actively star-forming phase.

We anchor the relative starless / star-forming lifetimes of 70% to 30% to an absolute lifetime using an estimate of the 6.7 GHz Class II CH_3OH maser lifetime from the literature of 35,000 years (van der Walt 2005). This estimate uses the same unbiased surveys we use to identify the maser locations (Szymczak et al. 2002; Ellingsen 1996). This estimate is based on extrapolating the number of masers detected in these surveys to a Milky Way total and using an IMF and global Milky Way star formation rate to estimate the lifetime of the masers *observed in these surveys*, a method similar to that used by Tackenberg et al. (2012) to determine the absolute lifetimes of starless clumps. This method includes the fact that never every massive star-forming region will necessarily go through a maser phase. The value of the absolute lifetime derived using CH_3OH masers is the most contentious in this analysis and will likely be improved upon in future studies (e.g., the 6 GHz multi beam maser survey, Green et al. 2009).

While the relative fraction of starless vs. star-forming HiSD regions is robust over many different column densities, the fraction of HiSD regions associated with methanol masers goes

steadily up as a function of column density (see Figure 5.1). In our two extreme determinations, 'generous' and 'conservative', the methanol maser fraction is 2% and 4%, respectively. Therefore, in the 'generous' identification, we derive an absolute starless lifetime of 1.2 Myr and a star-forming lifetime of 0.5 Myr for a total dust clump lifetime of 1.7 Myr, while in the 'conservative' identification, we get an absolute starless lifetime of 0.6 Myr and a star-forming lifetime of 0.3 Myr for a total dust clump lifetime of 0.9 Myr.

These starless lifetimes correspond to roughly a free fall time for typical clump sizes and densities at these distances. For the 'generous' criteria: $N(H_2) = 0.4 \times 10^{22}$ cm^{-2}, r = 1.1 pc (25″at the far distance of 9 kpc), $\tau_{ff} = 0.9$ Myr, so the starless lifetime of 1.2 Myr is just over 1 free fall time. For the 'conservative' criteria: $N(H_2) = 0.8 \times 10^{22}$ cm^{-2}, r = 0.7 pc (25″at the near distance of 5.5 kpc), $\tau_{ff} = 0.5$ Myr, so the starless lifetime of 0.6 Myr is also just over 1 free fall time. These densities are averages above the threshold used, so the free fall times are over the entire clump. The higher density cores embedded with each clump will have much shorter free fall times.

Interestingly, we find that the 6.7 GHz CH_3OH masers are nearly always found near the intersection of starless and star-forming HiSD regions. If we assume that the preferred location for these CH_3OH masers indicates a preferred time, then 6.7 GHz CH_3OH masers exist for a short period of time right around when a massive star turns on and are great targets for observations of the earliest phase of massive star formation.

5.3.3 Comparison with Other Lifetime Estimates

Previous lifetime estimates have found relative starless fractions between about 30-80% and extrapolate these to absolute starless lifetimes typically ranging from 10^3 - 10^4 years and up to 3.7 $\times 10^5$ years. These are based primarily on mid-IR emission signatures at 24 μm toward samples of IRDCs. Chambers et al. (2009) using a sample of 106 IRDC cores find 65% starless and 35% with 24 μm emission and EGOs (or 82% starless and 18% star-forming if we only include those cores identified to contain 8 μm emission as star-forming). They then extrapolate this to an absolute

starless lifetime of 3.7×10^5 years assuming a representative YSO lifetime accretion timescale of 2×10^5 years (Zinnecker & Yorke 2007) for the star-forming phase. Miettinen (2012) finds a starless / star-forming ratio of 44% to 56% using LABOCA, and extrapolate this in the same way to an absolute lifetime of 1.6×10^5 years. Wilcock et al. (2012) using Hi-GAL find 18% starless, 15% with emission at 24 μm, and 67% with emission at 8 μm, extrapolating in the same way to derive an absolute starless lifetime of 2×10^5 years. Tackenberg et al. (2012) target their search toward starless clumps in the ATLASGAL survey and derive a lifetime of the starless phase for the *most massive clumps* of 6×10^4 years based on an extrapolated total number of starless clumps in the Milky Way and the Milky Way star formation rate. Parsons et al. (2009) derive 33% starless and 67% with 24 μm emission using SCUBA targeted toward IRDCs. They extrapolate this to a starless lifetime of order 10^3 to 10^4 years based on typical estimates for massive star formation lifetimes. Dunham et al. (2011a) looked for mid-IR star formation signatures toward Bolocam Galactic Plane Survey (BGPS Aguirre et al. 2011) clumps find that 56% are starless, or when accounting for chance alignment, 80% are starless. Peretto & Fuller (2009) find a starless fraction of between 80%- 32% toward IRDCs, based on their lack of association with 24 μm point sources.

Many of the previous estimates of the lifetimes of the starless and star-forming phase for massive star forming regions discussed were targeted toward IRDCs and used emission at 24 μm as the indicator of star formation. Our analysis is not biased toward IRDCs and we include all HiSD regions above a massive star-forming column density threshold. We use 8 μm emission to uniquely indicate the signature of massive star formation, rather than 24 μm emission, which, while it may turn on earlier (e.g., Battersby et al. 2010), is not necessarily indicative of massive star formation (does not require UV-excited PAH emission). Additionally, previous analyses have calculated relative fractions of 'clumps' or 'cores,' defined in various ways and generally of arbitrary size. Each 'clump' or 'core' is denoted as starless or star-forming, meaning that a single 24 μm point source would classify the entire clump star-forming. Hence, since we use individual pixels, our somewhat higher than average starless fraction is not surprising. Additionally, our choice of maser lifetime to anchor our absolute lifetimes is unique and gives a longer than average absolute lifetime

estimate. If instead, we assume that the star-forming lifetime is 2×10^5 years (representative YSO accretion timescale, Zinnecker & Yorke 2007), as many others, we instead get a starless lifetime of 4.7×10^5 years.

5.4 Conclusion

Using column densities and dust temperature distributions derived from Hi-GAL, Spitzer 8 μm star formation signatures, and unbiased surveys for 6.7 GHz Class II CH_3OH masers, we determine the relative lifetimes of the starless and star-forming phases for massive star-forming regions in a $2^o \times 2^o$ field centered at [ℓ, b] = [30^o, 0^o]. We identify HiSD regions capable of forming massive stars by their column density and find that massive star-forming regions identified in the dust continuum spend about 70% of their lifetimes in the starless phase and 30% in the star-forming phase. 'Starless' refers only to a lack of massive stars and was determined by the temperature (cold, roughly $\leq$ 25 K, see §5.2.2 for details) and signature at 8 μm (dark or neutral). 'Star-forming' refers to active massive star formation as indicated by warmer dust temperatures ($>$ 25 K, roughly, see §5.2.2 for details) and emission at 8 μm. This relative fraction is determined robustly over a variety of reasonable cutoff parameters.

We use the absolute lifetime of methanol masers (35,000 years) determined from van der Walt (2005) to anchor these relative lifetimes to an absolute timescale. Our two extreme cutoffs suggest a starless lifetime of the order of 0.6 to 1.2 Myr (70%) and a star-forming lifetime of the order of 0.3 to 0.5 Myr (30%) for massive star-forming regions identified in the dust continuum. These starless lifetimes correspond to roughly a free fall times at typical clump densities (high density cores embedded in these clumps will have much shorter free fall times).

We also find that 6.7 GHz CH_3OH masers appear at the intersection between starless and star-forming HiSD regions. This provides evidence to support the idea that these masers exist for a short period of time right when a massive star turns on, and that 6.7 GHz masers trace the earliest phase of massive star formation.

Chapter 6

Conclusion

In this thesis, we present a global and high-resolution analysis of the formation of massive stars and stellar clusters. We measure the physical conditions (temperature, column density, and virial parameter) at the onset of massive star formation, study how these conditions change with evolutionary phase, and estimate the duration of each of the phases. These results allow us to identify precursors to stellar clusters in a systematic way throughout the Galaxy for the first time as well as providing the tools and necessary framework for a true Galactic-scale understanding of massive star and stellar cluster formation.

In Chapter 2, we measure the high-resolution ($\sim$ 0.1 pc) temperature and density structure as a function of evolutionary phase within a single IRDC, which allows us to disentangle the effects of evolution from observational biases introduced by distance, Galactic-scale abundance variations, and large-scale environment. We compare our observations with the literature and find some common conditions at the onset of massive star formation. Much work remains to be done, however, to fully disentangle the effects of evolution and observational biases on these observed conditions. We find that the youngest cores seem to be more extended, with shallower density profiles, than the more evolved cores, and hypothesize global clump collapse as the cores collapse. Whether or not these cores accrete from large (clump) scales or are undergoing slow collapse in approximate virial equilibrium remains an open question. Answering this question will require a large sample of high-resolution observations of the dense gas kinematics toward cores in a variety of evolutionary stages.

Chapter 3 presents an expansion of this analysis to larger scales (about 4×2 square degrees of the Galactic Plane) but at lower spatial resolution ($\sim 25''$). In this analysis, we derive temperature and column density maps based on dust continuum emission observed with the Herschel Infrared Galactic Plane Survey (Hi-GAL) and compare these physical properties with the observed star formation tracers in a systematic way. The method presented to derive temperatures and column densities is the only one of its kind (a modified blackbody fit to Herschel far-IR data) to subtract off the diffuse Galactic cirrus emission, making a significant qualitative and quantitative difference in the analysis. This method allows us to identify pre-cluster clumps (PCCs) based on their physical properties, and we demonstrate that we can identify PCCs throughout the Galaxy by identifying IRDC-like clouds on the far-side of the Galaxy for the first time. Using this method over the entire Hi-GAL survey, we could identify the Galactic population of PCCs, and in doing so, derive their Galactic distribution, formation rate, and mass function.

Our systematic comparison of physical properties with star formation tracers allows us to measure the changes in physical properties as a function of evolutionary stage. The evolutionary sequence we observe matches that at higher-resolution, though with less contrast due to beam dilution of each stage. This sequence begins with cold quiescent clumps which are dark or neutral at 8 μm and show no signs of star formation. The next stage is slightly warmer and shows signs of shocks in outflows, such as EGOs and CH_3OH masers. As star formation proceeds, the clump continues to heat up and, if there is a massive star, we can observe a UCHII region and the associated PAH UV-excited bubble lighting up at 8 μm. This work provides the first demonstration of systematically different physical properties as a function of evolutionary stage.

In Chapter 4, we compare the physical properties in massive star-forming regions derived from gas with those derived using dust. A comparison of the column densities using a variety of tracers allows us to derive an NH_3 abundance while also providing a reminder that systematic differences between tracers can easily lead to discrepancies of order a factor of 2. The measured dust and gas temperatures agree well in the actively star-forming region observed, but the dust temperature measured is lower ($T_{dust} \sim 11$ K) than the measured gas temperature ($T_{gas} \sim$ 13-17

K). This discrepancy is likely due to either a lack of gas and dust coupling in the youngest regions ($\sim$ 0.5 Myr) or a failure of the cirrus-subtracted modified blackbody fits in this extreme (very cold) regime. More evidence is required to support either hypothesis.

We also compare the high-resolution ($\sim$ 0.1 pc, 4″) NH_3 observations with single dish Green Bank Telescope (GBT) NH_3 observations and Bolocam Galactic Plane Survey (BGPS) 1.1 mm observations. The high-resolution observations agree very well with the GBT data. To compare the high-resolution NH_3 data with BGPS observations, we convert the NH_3 derived gas temperatures and column densities to derive a 1.1 mm flux and compare that with the lower resolution (33″) BGPS flux. We find that there is no dominant origin for pc-scale millimeter continuum emission. The millimeter emission traced by the BGPS traces high-density cores, both cold and hot, as well as the dense filaments from which they form, and the diffuse envelope surrounding the filaments. The fraction of flux originating from each structure is variable.

Finally, in Chapter 5, we use data presented in Chapter 3 to separate out starless and star-forming clumps and estimate a relative lifetime for the two phases in massive star-forming regions. We use the dust temperatures and 8 μm signature (dark, neutral, or bright) to separate the starless from the star-forming pixels, where we use the starless to signify a lack of the signature of a massive star. We then estimate an approximate beam-diluted column density threshold for massive star formation and include only pixels above that threshold. Then, assuming that the relative fraction in each state represents the relative lifetime, we find that massive star-forming regions spend about 70% of their lives in the starless phase and about 30% in the warm, 8 μm bright phase.

We also calculate the relative fraction of pixels containing Class II CH_3OH masers and find that it represents about 2-4% of the total lifetime of clumps. The absolute lifetime of Class II CH_3OH masers has been determined in van der Walt (2005) to be about 35,000 years. If we use that lifetime to anchor the relative lifetimes of the starless and star-forming populations, we find a starless lifetime of about 0.6 to 1.2 Myr (70%) and a star-forming lifetime of about 0.3 to 0.5 Myr (30%). These lifetimes refer to the lifetime during which the region has sufficient cold dust column density to be detected in the Herschel survey above our massive star-forming threshold.

We also find that the Class II CH_3OH masers tend to appear right at the intersection between the starless and star-forming phase, indicating that they may trace the very earliest phases of massive star formation.

This thesis provides constraints on the physical properties at the onset of massive star formation, how these properties evolve, and how long these phases last. Each piece is more of a beginning than an end, as the tools that have been created for this analysis can and ought to be applied to more regions. In particular, we intend to implement the modified blackbody fitter across the Galactic Plane using Hi-GAL, which, in combination with distance estimates, should allow for a measure of the Galactic distribution, formation rate, and mass function of forming star clusters.

The evolutionary sequence presented is limited in its sophistication by the nature of the present data. Larger samples will allow for a better disentanglement of evolutionary stage and other factors. The future of this research will be incorporating the gas dynamics on both large and small scales. How is the gas collapsing and on what scales and at what rates? The large-scale gas dynamics are crucial for understanding how quiescent clumps collapse to form stars. How do these clumps accrete their mass? Whether clumps accrete mass from large scales through filamentary gas flows, undergo slow global collapse, or rapid free-fall collapse is still an open question to be addressed by studying the large-scale gas dynamics. An understanding of the gas dynamics at small scales may be the best way to conclusively distinguish between competing theories of massive star formation. Are the star-forming cores bound and in virial equilibrium or rapidly collapsing and accreting material?

In the future, we will continue to study the formation of massive stars and stellar clusters both globally and at high-resolution. We plan to use the algorithm presented to identify pre-cluster clumps (PCCs) throughout the Galaxy and derive their Galactic distribution, formation rate, and mass function. Using existing Galactic surveys of dense gas emission, we can study the large-scale gas kinematics toward our identified PCCs as a function of evolutionary stage. From this large sample, we can select both an extreme (e.g., highest mass, lowest temperature, lowest virial parameter) and representative (e.g., typical masses, temperatures, and virial parameters) sample

for high-resolution follow-up.

Bibliography

Aguirre, J. E., Ginsburg, A. G., Dunham, M. K., Drosback, M. M., Bally, J., Battersby, C., Bradley, E. T., Cyganowski, C., Dowell, D., Evans, II, N. J., Glenn, J., Harvey, P., Rosolowsky, E., Stringfellow, G. S., Walawender, J., & Williams, J. P. 2011, ApJS, 192, 4

Anderson, L. D., Bania, T. M., Balser, D. S., & Rood, R. T. 2011, ApJS, 194, 32

Arzoumanian, D., André, P., Didelon, P., Könyves, V., Schneider, N., Men'shchikov, A., Sousbie, T., Zavagno, A., Bontemps, S., di Francesco, J., Griffin, M., Hennemann, M., Hill, T., Kirk, J., Martin, P., Minier, V., Molinari, S., Motte, F., Peretto, N., Pezzuto, S., Spinoglio, L., Ward-Thompson, D., White, G., & Wilson, C. D. 2011, A&A, 529, L6

Bally, J., Anderson, L. D., Battersby, C., Calzoletti, L., Digiorgio, A. M., Faustini, F., Ginsburg, A., Li, J. Z., Nguyen-Luong, Q., Molinari, S., Motte, F., Pestalozzi, M., Plume, R., Rodon, J., Schilke, P., Schlingman, W., Schneider-Bontemps, N., Shirley, Y., Stringfellow, G. S., Testi, L., Traficante, A., Veneziani, M., & Zavagno, A. 2010, A&A, 518, L90+

Battersby, C., & Bally, J. 2012, ArXiv e-prints

Battersby, C., Bally, J., Ginsburg, A., Bernard, J.-P., Brunt, C., Fuller, G. A., Martin, P., Molinari, S., Mottram, J., Peretto, N., Testi, L., & Thompson, M. A. 2011, A&A, 535, A128

Battersby, C., Bally, J., Jackson, J. M., Ginsburg, A., Shirley, Y. L., Schlingman, W., & Glenn, J. 2010, ApJ, 721, 222

Battersby, C., Longmore, S., Ginsburg, A., & Bally, J. 2013, in prep

Benjamin, R. A., Churchwell, E., Babler, B. L., Bania, T. M., Clemens, D. P., Cohen, M., Dickey, J. M., Indebetouw, R., Jackson, J. M., Kobulnicky, H. A., Lazarian, A., Marston, A. P., Mathis, J. S., Meade, M. R., Seager, S., Stolovy, S. R., Watson, C., Whitney, B. A., Wolff, M. J., & Wolfire, M. G. 2003, PASP, 115, 953

Bergin, E. A., & Tafalla, M. 2007, ARA&A, 45, 339

Bernard, J., Paradis, D., Marshall, D. J., Montier, L., Lagache, G., Paladini, R., Veneziani, M., Brunt, C. M., Mottram, J. C., Martin, P., Ristorcelli, I., Noriega-Crespo, A., Compiègne, M., Flagey, N., Anderson, L. D., Popescu, C. C., Tuffs, R., Reach, W., White, G., Benedetti, M., Calzoletti, L., Digiorgio, A. M., Faustini, F., Juvela, M., Joblin, C., Joncas, G., Mivilles-Deschenes, M., Olmi, L., Traficante, A., Piacentini, F., Zavagno, A., & Molinari, S. 2010, A&A, 518, L88+

Beuther, H., Henning, T., Linz, H., Krause, O., Nielbock, M., & Steinacker, J. 2010, A&A, 518, L78+

Beuther, H., Schilke, P., Menten, K. M., Motte, F., Sridharan, T. K., & Wyrowski, F. 2002, ApJ, 566, 945

Beuther, H., & Sridharan, T. K. 2007, ApJ, 668, 348

Beuther, H., Walsh, A. J., & Longmore, S. N. 2009, ApJS, 184, 366

Beuther, H., Walsh, A. J., Thorwirth, S., Zhang, Q., Hunter, T. R., Megeath, S. T., & Menten, K. M. 2007a, A&A, 466, 989

Beuther, H., Zhang, Q., Bergin, E. A., Sridharan, T. K., Hunter, T. R., & Leurini, S. 2007b, A&A, 468, 1045

Bonnell, I. A., Bate, M. R., Clarke, C. J., & Pringle, J. E. 2001, MNRAS, 323, 785

Bontemps, S., Motte, F., Csengeri, T., & Schneider, N. 2010, A&A, 524, A18

Bressert, E., Bastian, N., Gutermuth, R., Megeath, S. T., Allen, L., Evans, II, N. J., Rebull, L. M., Hatchell, J., Johnstone, D., Bourke, T. L., Cieza, L. A., Harvey, P. M., Merin, B., Ray, T. P., & Tothill, N. F. H. 2010, MNRAS, 409, L54

Briggs, D. S., Schwab, F. R., & Sramek, R. A. 1999, in Astronomical Society of the Pacific Conference Series, Vol. 180, Synthesis Imaging in Radio Astronomy II, ed. G. B. Taylor, C. L. Carilli, & R. A. Perley, 127

Brogan, C. L., Hunter, T. R., Cyganowski, C. J., Indebetouw, R., Beuther, H., Menten, K. M., & Thorwirth, S. 2009, ApJ, 707, 1

Butler, M. J., & Tan, J. C. 2009, ApJ, 696, 484

Carey, S. J., Clark, F. O., Egan, M. P., Price, S. D., Shipman, R. F., & Kuchar, T. A. 1998, ApJ, 508, 721

Carey, S. J., Feldman, P. A., Redman, R. O., Egan, M. P., MacLeod, J. M., & Price, S. D. 2000, ApJL, 543, L157

Carey, S. J., Noriega-Crespo, A., Mizuno, D. R., Shenoy, S., Paladini, R., Kraemer, K. E., Price, S. D., Flagey, N., Ryan, E., Ingalls, J. G., Kuchar, T. A., Pinheiro Gonçalves, D., Indebetouw, R., Billot, N., Marleau, F. R., Padgett, D. L., Rebull, L. M., Bressert, E., Ali, B., Molinari, S., Martin, P. G., Berriman, G. B., Boulanger, F., Latter, W. B., Miville-Deschenes, M. A., Shipman, R., & Testi, L. 2009, PASP, 121, 76

Carrasco-González, C., Rodríguez, L. F., Torrelles, J. M., Anglada, G., & González-Martín, O. 2010, AJ, 139, 2433

Chambers, E. T., Jackson, J. M., Rathborne, J. M., & Simon, R. 2009, ApJS, 181, 360

Chira, R.-A., Beuther, H., Linz, H., Schuller, F., Walmsley, C. M., Menten, K. M., & Bronfman, L. 2013, A&A, 552, A40

Compiègne, M., Flagey, N., Noriega-Crespo, A., Martin, P. G., Bernard, J., Paladini, R., & Molinari, S. 2010, ApJL, 724, L44

Cyganowski, C. J., Brogan, C. L., Hunter, T. R., & Churchwell, E. 2009, ApJ, 702, 1615

Cyganowski, C. J., Whitney, B. A., Holden, E., Braden, E., Brogan, C. L., Churchwell, E., Indebetouw, R., Watson, D. F., Babler, B. L., Benjamin, R., Gomez, M., Meade, M. R., Povich, M. S., Robitaille, T. P., & Watson, C. 2008, AJ, 136, 2391

de Wit, W. J., Testi, L., Palla, F., & Zinnecker, H. 2005, A&A, 437, 247

Desert, F., Boulanger, F., & Puget, J. L. 1990, A&A, 237, 215

Devine, K. E., Chandler, C. J., Brogan, C., Churchwell, E., Indebetouw, R., Shirley, Y., & Borg, K. J. 2011, ApJ, 733, 44

Dunham, M. K., Robitaille, T. P., Evans, II, N. J., Schlingman, W. M., Cyganowski, C. J., & Urquhart, J. 2011a, ApJ, 731, 90

Dunham, M. K., Rosolowsky, E., Evans, II, N. J., Cyganowski, C., & Urquhart, J. S. 2011b, ApJ, 741, 110

Egan, M. P., Shipman, R. F., Price, S. D., Carey, S. J., Clark, F. O., & Cohen, M. 1998, ApJL, 494, L199

Ellingsen, S. 1996, PhD thesis, Physics Department, University of Tasmania, GPO Box 252C, Hobart 7001, Australia

Elmegreen, B. G. 2000, ApJ, 530, 277

—. 2007, ApJ, 668, 1064

Enoch, M. L., Young, K. E., Glenn, J., Evans, II, N. J., Golwala, S., Sargent, A. I., Harvey, P., Aguirre, J., Goldin, A., Haig, D., Huard, T. L., Lange, A., Laurent, G., Maloney, P., Mauskopf, P., Rossinot, P., & Sayers, J. 2006, ApJ, 638, 293

Fontani, F., Caselli, P., Zhang, Q., Brand, J., Busquet, G., & Palau, A. 2012, A&A, 541, A32

Frieswijk, W. W. F., Spaans, M., Shipman, R. F., Teyssier, D., & Hily-Blant, P. 2007, A&A, 475, 263

Galván-Madrid, R., Zhang, Q., Keto, E., Ho, P. T. P., Zapata, L. A., Rodríguez, L. F., Pineda, J. E., & Vázquez-Semadeni, E. 2010, ApJ, 725, 17

Gautier, III, T. N., Boulanger, F., Perault, M., & Puget, J. L. 1992, AJ, 103, 1313

Gieles, M., & Portegies Zwart, S. F. 2011, MNRAS, 410, L6

Ginsburg, A., & Mirocha, J. 2011, in Astrophysics Source Code Library, record ascl:1109.001, 9001

Goldsmith, P. F. 2001, ApJ, 557, 736

Gouliermis, D. A., Schmeja, S., Dolphin, A. E., Gennaro, M., Tognelli, E., & Prada Moroni, P. G. 2012, ApJ, 748, 64

Green, J. A., Caswell, J. L., Fuller, G. A., Avison, A., Breen, S. L., Brooks, K., Burton, M. G., Chrysostomou, A., Cox, J., Diamond, P. J., Ellingsen, S. P., Gray, M. D., Hoare, M. G., Masheder, M. R. W., McClure-Griffiths, N. M., Pestalozzi, M., Phillips, C., Quinn, L., Thompson, M. A., Voronkov, M. A., Walsh, A., Ward-Thompson, D., Wong-McSweeney, D., Yates, J. A., & Cohen, R. J. 2009, MNRAS, 392, 783

Griffin, M. J., Abergel, A., Abreu, A., Ade, P. A. R., André, P., Augueres, J.-L., Babbedge, T., Bae, Y., Baillie, T., Baluteau, J.-P., Barlow, M. J., Bendo, G., Benielli, D., Bock, J. J., Bonhomme, P., Brisbin, D., Brockley-Blatt, C., Caldwell, M., Cara, C., Castro-Rodriguez, N., Cerulli, R., Chanial, P., Chen, S., Clark, E., Clements, D. L., Clerc, L., Coker, J., Communal, D., Conversi, L., Cox, P., Crumb, D., Cunningham, C., Daly, F., Davis, G. R., de Antoni, P., Delderfield, J., Devin, N., di Giorgio, A., Didschuns, I., Dohlen, K., Donati, M., Dowell, A., Dowell, C. D., Duband, L., Dumaye, L., Emery, R. J., Ferlet, M., Ferrand, D., Fontignie, J., Fox, M., Franceschini, A., Frerking, M., Fulton, T., Garcia, J., Gastaud, R., Gear, W. K., Glenn, J., Goizel, A., Griffin, D. K., Grundy, T., Guest, S., Guillemet, L., Hargrave, P. C., Harwit, M., Hastings, P., Hatziminaoglou, E., Herman, M., Hinde, B., Hristov, V., Huang, M., Imhof, P., Isaak, K. J., Israelsson, U., Ivison, R. J., Jennings, D., Kiernan, B., King, K. J., Lange, A. E., Latter, W., Laurent, G., Laurent, P., Leeks, S. J., Lellouch, E., Levenson, L., Li, B., Li, J., Lilienthal, J., Lim, T., Liu, S. J., Lu, N., Madden, S., Mainetti, G., Marliani, P., McKay, D., Mercier, K., Molinari, S., Morris, H., Moseley, H., Mulder, J., Mur, M., Naylor, D. A., Nguyen, H., O'Halloran, B., Oliver, S., Olofsson, G., Olofsson, H.-G., Orfei, R., Page, M. J., Pain, I., Panuzzo, P., Papageorgiou, A., Parks, G., Parr-Burman, P., Pearce, A., Pearson, C., Pérez-Fournon, I., Pinsard, F., Pisano, G., Podosek, J., Pohlen, M., Polehampton, E. T., Pouliquen, D., Rigopoulou, D., Rizzo, D., Roseboom, I. G., Roussel, H., Rowan-Robinson, M., Rownd, B., Saraceno, P., Sauvage, M., Savage, R., Savini, G., Sawyer, E., Scharmberg, C., Schmitt, D., Schneider, N., Schulz, B., Schwartz, A., Shafer, R., Shupe, D. L., Sibthorpe, B., Sidher, S., Smith, A., Smith, A. J., Smith, D., Spencer, L., Stobie, B., Sudiwala, R., Sukhatme, K., Surace, C., Stevens, J. A., Swinyard, B. M., Trichas, M., Tourette, T., Triou, H., Tseng, S., Tucker, C., Turner, A., Vaccari, M., Valtchanov, I., Vigroux, L., Virique, E., Voellmer, G., Walker, H., Ward, R., Waskett, T., Weilert, M., Wesson, R., White, G. J., Whitehouse, N., Wilson, C. D., Winter, B., Woodcraft, A. L., Wright, G. S., Xu, C. K., Zavagno, A., Zemcov, M., Zhang, L., & Zonca, E. 2010, A&A, 518, L3

Harju, J., Walmsley, C. M., & Wouterloot, J. G. A. 1993, A&AS, 98, 51

Hartmann, L., & Burkert, A. 2007, ApJ, 654, 988

Helfand, D. J., Becker, R. H., White, R. L., Fallon, A., & Tuttle, S. 2006, AJ, 131, 2525

Ho, P. T. P., & Townes, C. H. 1983, ARA&A, 21, 239

Jackson, J. M., Rathborne, J. M., Shah, R. Y., Simon, R., Bania, T. M., Clemens, D. P., Chambers, E. T., Johnson, A. M., Dormody, M., Lavoie, R., & Heyer, M. H. 2006, ApJS, 163, 145

Juvela, M., Harju, J., Ysard, N., & Lunttila, T. 2012, A&A, 538, A133

Kauffmann, J., Bertoldi, F., Bourke, T. L., Evans, II, N. J., & Lee, C. W. 2008, A&A, 487, 993

Kauffmann, J., & Pillai, T. 2010, ApJL, 723, L7

Krumholz, M. R., Klein, R. I., McKee, C. F., Offner, S. S. R., & Cunningham, A. J. 2009, Science, 323, 754

Krumholz, M. R., & McKee, C. F. 2008, Nature, 451, 1082

Lada, C. J., & Lada, E. A. 2003, ARA&A, 41, 57

Li, D., Kauffmann, J., Zhang, Q., & Chen, W. 2013, ApJL, 768, L5

Liu, H. B., Jiménez-Serra, I., Ho, P. T. P., Chen, H.-R., Zhang, Q., & Li, Z.-Y. 2012, ApJ, 756, 10

Longmore, S. N., Burton, M. G., Barnes, P. J., Wong, T., Purcell, C. R., & Ott, J. 2007, MNRAS, 379, 535

Longmore, S. N., Pillai, T., Keto, E., Zhang, Q., & Qiu, K. 2011, ApJ, 726, 97

Low, F. J., Young, E., Beintema, D. A., Gautier, T. N., Beichman, C. A., Aumann, H. H., Gillett, F. C., Neugebauer, G., Boggess, N., & Emerson, J. P. 1984, ApJL, 278, L19

Lucas, R., & Liszt, H. 1998, A&A, 337, 246

Mangum, J. G., Wootten, A., & Mundy, L. G. 1992, ApJ, 388, 467

Markwardt, C. B. 2009, in Astronomical Society of the Pacific Conference Series, Vol. 411, Astronomical Data Analysis Software and Systems XVIII, ed. D. A. Bohlender, D. Durand, & P. Dowler, 251

Martel, H., Urban, A., & Evans, II, N. J. 2012, ApJ, 757, 59

Martin, P. G., Miville-Deschênes, M., Roy, A., Bernard, J., Molinari, S., Billot, N., Brunt, C., Calzoletti, L., Digiorgio, A. M., Elia, D., Faustini, F., Joncas, G., Mottram, J. C., Natoli, P., Noriega-Crespo, A., Paladini, R., Robitaille, J. F., Strafella, F., Traficante, A., & Veneziani, M. 2010, A&A, 518, L105+

McKee, C. F., & Tan, J. C. 2003, ApJ, 585, 850

McLaughlin, D. E., & Pudritz, R. E. 1996, ApJ, 469, 194

Miettinen, O. 2012, A&A, 542, A101

Minier, V., Conway, J. E., & Booth, R. S. 2001, A&A, 369, 278

Minier, V., Ellingsen, S. P., Norris, R. P., & Booth, R. S. 2003, A&A, 403, 1095

Miville-Deschênes, M., & Lagache, G. 2005, ApJS, 157, 302

Miville-Deschênes, M.-A., Lagache, G., Boulanger, F., & Puget, J.-L. 2007, A&A, 469, 595

Molinari, S., Swinyard, B., Bally, J., Barlow, M., Bernard, J.-P., Martin, P., Moore, T., Noriega-Crespo, A., Plume, R., Testi, L., Zavagno, A., Abergel, A., Ali, B., Anderson, L., André, P., Baluteau, J.-P., Battersby, C., Beltrán, M. T., Benedettini, M., Billot, N., Blommaert, J., Bontemps, S., Boulanger, F., Brand, J., Brunt, C., Burton, M., Calzoletti, L., Carey, S., Caselli, P., Cesaroni, R., Cernicharo, J., Chakrabarti, S., Chrysostomou, A., Cohen, M., Compiegne, M., de Bernardis, P., de Gasperis, G., di Giorgio, A. M., Elia, D., Faustini, F., Flagey, N., Fukui,

Y., Fuller, G. A., Ganga, K., Garcia-Lario, P., Glenn, J., Goldsmith, P. F., Griffin, M., Hoare, M., Huang, M., Ikhenaode, D., Joblin, C., Joncas, G., Juvela, M., Kirk, J. M., Lagache, G., Li, J. Z., Lim, T. L., Lord, S. D., Marengo, M., Marshall, D. J., Masi, S., Massi, F., Matsuura, M., Minier, V., Miville-Deschênes, M.-A., Montier, L. A., Morgan, L., Motte, F., Mottram, J. C., Müller, T. G., Natoli, P., Neves, J., Olmi, L., Paladini, R., Paradis, D., Parsons, H., Peretto, N., Pestalozzi, M., Pezzuto, S., Piacentini, F., Piazzo, L., Polychroni, D., Pomarès, M., Popescu, C. C., Reach, W. T., Ristorcelli, I., Robitaille, J.-F., Robitaille, T., Rodón, J. A., Roy, A., Royer, P., Russeil, D., Saraceno, P., Sauvage, M., Schilke, P., Schisano, E., Schneider, N., Schuller, F., Schulz, B., Sibthorpe, B., Smith, H. A., Smith, M. D., Spinoglio, L., Stamatellos, D., Strafella, F., Stringfellow, G. S., Sturm, E., Taylor, R., Thompson, M. A., Traficante, A., Tuffs, R. J., Umana, G., Valenziano, L., Vavrek, R., Veneziani, M., Viti, S., Waelkens, C., Ward-Thompson, D., White, G., Wilcock, L. A., Wyrowski, F., Yorke, H. W., & Zhang, Q. 2010, A&A, 518, L100

Motte, F., Schilke, P., & Lis, D. C. 2003, ApJ, 582, 277

Mottram, J. C., Hoare, M. G., Lumsden, S. L., Oudmaijer, R. D., Urquhart, J. S., Meade, M. R., Moore, T. J. T., & Stead, J. J. 2010, A&A, 510, A89+

Mueller, K. E., Shirley, Y. L., Evans, II, N. J., & Jacobson, H. R. 2002, ApJS, 143, 469

Myers, P. C. 2009, ApJ, 700, 1609

Omont, A., Gilmore, G. F., Alard, C., Aracil, B., August, T., Baliyan, K., Beaulieu, S., Bégon, S., Bertou, X., Blommaert, J. A. D. L., Borsenberger, J., Burgdorf, M., Caillaud, B., Cesarsky, C., Chitre, A., Copet, E., de Batz, B., Egan, M. P., Egret, D., Epchtein, N., Felli, M., Fouqué, P., Ganesh, S., Genzel, R., Glass, I. S., Gredel, R., Groenewegen, M. A. T., Guglielmo, F., Habing, H. J., Hennebelle, P., Jiang, B., Joshi, U. C., Kimeswenger, S., Messineo, M., Miville-Deschênes, M. A., Moneti, A., Morris, M., Ojha, D. K., Ortiz, R., Ott, S., Parthasarathy, M., Pérault, M., Price, S. D., Robin, A. C., Schultheis, M., Schuller, F., Simon, G., Soive, A., Testi, L., Teyssier, D., Tiphène, D., Unavane, M., van Loon, J. T., & Wyse, R. 2003, A&A, 403, 975

Ossenkopf, V., & Henning, T. 1994, A&A, 291, 943

Ott, S. 2010, in Astronomical Society of the Pacific Conference Series, Vol. 434, Astronomical Data Analysis Software and Systems XIX, ed. Y. Mizumoto, K.-I. Morita, & M. Ohishi, 139

Palau, A., Fuente, A., Girart, J. M., Estalella, R., Ho, P. T. P., Sánchez-Monge, Á., Fontani, F., Busquet, G., Commerçon, B., Hennebelle, P., Boissier, J., Zhang, Q., Cesaroni, R., & Zapata, L. A. 2013, ApJ, 762, 120

Paradis, D., Veneziani, M., Noriega-Crespo, A., Paladini, R., Piacentini, F., Bernard, J. P., de Bernardis, P., Calzoletti, L., Faustini, F., Martin, P., Masi, S., Montier, L., Natoli, P., Ristorcelli, I., Thompson, M. A., Traficante, A., & Molinari, S. 2010, A&A, 520, L8+

Parsons, H., Thompson, M. A., & Chrysostomou, A. 2009, MNRAS, 399, 1506

Perault, M., Omont, A., Simon, G., Seguin, P., Ojha, D., Blommaert, J., Felli, M., Gilmore, G., Guglielmo, F., Habing, H., Price, S., Robin, A., de Batz, B., Cesarsky, C., Elbaz, D., Epchtein, N., Fouque, P., Guest, S., Levine, D., Pollock, A., Prusti, T., Siebenmorgen, R., Testi, L., & Tiphene, D. 1996, A&A, 315, L165

Peretto, N., & Fuller, G. A. 2009, A&A, 505, 405

—. 2010, ApJ, 723, 555

Peretto, N., Fuller, G. A., Plume, R., Anderson, L. D., Bally, J., Battersby, C., Beltran, M. T., Bernard, J., Calzoletti, L., Digiorgio, A. M., Faustini, F., Kirk, J. M., Lenfestey, C., Marshall, D., Martin, P., Molinari, S., Montier, L., Motte, F., Ristorcelli, I., Rodón, J. A., Smith, H. A., Traficante, A., Veneziani, M., Ward-Thompson, D., & Wilcock, L. 2010, A&A, 518, L98+

Pestalozzi, M. R., Minier, V., & Booth, R. S. 2005, A&A, 432, 737

Pilbratt, G. L., Riedinger, J. R., Passvogel, T., Crone, G., Doyle, D., Gageur, U., Heras, A. M., Jewell, C., Metcalfe, L., Ott, S., & Schmidt, M. 2010, A&A, 518, L1

Pillai, T., Kauffmann, J., Wyrowski, F., Hatchell, J., Gibb, A. G., & Thompson, M. A. 2011, A&A, 530, A118

Pillai, T., Wyrowski, F., Carey, S. J., & Menten, K. M. 2006, A&A, 450, 569

Poglitsch, A., Waelkens, C., Geis, N., Feuchtgruber, H., Vandenbussche, B., Rodriguez, L., Krause, O., Renotte, E., van Hoof, C., Saraceno, P., Cepa, J., Kerschbaum, F., Agnèse, P., Ali, B., Altieri, B., Andreani, P., Augueres, J.-L., Balog, Z., Barl, L., Bauer, O. H., Belbachir, N., Benedettini, M., Billot, N., Boulade, O., Bischof, H., Blommaert, J., Callut, E., Cara, C., Cerulli, R., Cesarsky, D., Contursi, A., Creten, Y., De Meester, W., Doublier, V., Doumayrou, E., Duband, L., Exter, K., Genzel, R., Gillis, J.-M., Grözinger, U., Henning, T., Herreros, J., Huygen, R., Inguscio, M., Jakob, G., Jamar, C., Jean, C., de Jong, J., Katterloher, R., Kiss, C., Klaas, U., Lemke, D., Lutz, D., Madden, S., Marquet, B., Martignac, J., Mazy, A., Merken, P., Montfort, F., Morbidelli, L., Müller, T., Nielbock, M., Okumura, K., Orfei, R., Ottensamer, R., Pezzuto, S., Popesso, P., Putzeys, J., Regibo, S., Reveret, V., Royer, P., Sauvage, M., Schreiber, J., Stegmaier, J., Schmitt, D., Schubert, J., Sturm, E., Thiel, M., Tofani, G., Vavrek, R., Wetzstein, M., Wieprecht, E., & Wiezorrek, E. 2010, A&A, 518, L2

Purcell, C. R., Longmore, S. N., Burton, M. G., Walsh, A. J., Minier, V., Cunningham, M. R., & Balasubramanyam, R. 2009, MNRAS, 394, 323

Ragan, S. E., Bergin, E. A., Plume, R., Gibson, D. L., Wilner, D. J., O'Brien, S., & Hails, E. 2006, ApJS, 166, 567

Ragan, S. E., Bergin, E. A., & Wilner, D. 2011, ApJ, 736, 163

Rathborne, J. M., Jackson, J. M., & Simon, R. 2006, ApJ, 641, 389

Rathborne, J. M., Jackson, J. M., Zhang, Q., & Simon, R. 2008, ApJ, 689, 1141

Reid, M. J., Menten, K. M., Zheng, X. W., Brunthaler, A., Moscadelli, L., Xu, Y., Zhang, B., Sato, M., Honma, M., Hirota, T., Hachisuka, K., Choi, Y. K., Moellenbrock, G. A., & Bartkiewicz, A. 2009, ApJ, 700, 137

Rosolowsky, E., Dunham, M. K., Ginsburg, A., Bradley, E. T., Aguirre, J., Bally, J., Battersby, C., Cyganowski, C., Dowell, D., Drosback, M., Evans, N. J., Glenn, J., Harvey, P., Stringfellow, G. S., Walawender, J., & Williams, J. P. 2010, ApJS, 188, 123

Rosolowsky, E. W., Pineda, J. E., Foster, J. B., Borkin, M. A., Kauffmann, J., Caselli, P., Myers, P. C., & Goodman, A. A. 2008, ApJS, 175, 509

Roy, A., Ade, P. A. R., Bock, J. J., Chapin, E. L., Devlin, M. J., Dicker, S. R., Griffin, M., Gundersen, J. O., Halpern, M., Hargrave, P. C., Hughes, D. H., Klein, J., Marsden, G., Martin, P. G., Mauskopf, P., Miville-Deschênes, M.-A., Netterfield, C. B., Olmi, L., Patanchon, G., Rex, M., Scott, D., Semisch, C., Truch, M. D. P., Tucker, C., Tucker, G. S., Viero, M. P., & Wiebe, D. V. 2010, ApJ, 708, 1611

Russeil, D., Pestalozzi, M., Mottram, J. C., Bontemps, S., Anderson, L. D., Zavagno, A., Beltrán, M. T., Bally, J., Brand, J., Brunt, C., Cesaroni, R., Joncas, G., Marshall, D., Martin, P., Massi, F., Molinari, S., Moore, T., Noriega-Crespo, A., Olmi, L., Thompson, M. A., Wienen, M., & Wyrowski, F. 2011, A&A, 526, A151+

Schuller, F., Menten, K. M., Contreras, Y., Wyrowski, F., Schilke, P., Bronfman, L., Henning, T., Walmsley, C. M., Beuther, H., Bontemps, S., Cesaroni, R., Deharveng, L., Garay, G., Herpin, F., Lefloch, B., Linz, H., Mardones, D., Minier, V., Molinari, S., Motte, F., Nyman, L.-Å., Reveret, V., Risacher, C., Russeil, D., Schneider, N., Testi, L., Troost, T., Vasyunina, T., Wienen, M., Zavagno, A., Kovacs, A., Kreysa, E., Siringo, G., & Weiß, A. 2009, A&A, 504, 415

Shu, F. H., Adams, F. C., & Lizano, S. 1987, ARA&A, 25, 23

Simon, R., Jackson, J. M., Rathborne, J. M., & Chambers, E. T. 2006, ApJ, 639, 227

Stil, J. M., Taylor, A. R., Dickey, J. M., Kavars, D. W., Martin, P. G., Rothwell, T. A., Boothroyd, A. I., Lockman, F. J., & McClure-Griffiths, N. M. 2006, AJ, 132, 1158

Szymczak, M., Kus, A. J., Hrynek, G., Kěpa, A., & Pazderski, E. 2002, A&A, 392, 277

Tackenberg, J., Beuther, H., Henning, T., Schuller, F., Wienen, M., Motte, F., Wyrowski, F., Bontemps, S., Bronfman, L., Menten, K., Testi, L., & Lefloch, B. 2012, A&A, 540, A113

Tan, J. C., Krumholz, M. R., & McKee, C. F. 2006, ApJL, 641, L121

Traficante, A., Calzoletti, L., Veneziani, M., Ali, B., de Gasperis, G., di Giorgio, A. M., Faustini, F., Ikhenaode, D., Molinari, S., Natoli, P., Pestalozzi, M., Pezzuto, S., Piacentini, F., Piazzo, L., Polenta, G., & Schisano, E. 2011, MNRAS, 416, 2932

Vacca, W. D., Garmany, C. D., & Shull, J. M. 1996, ApJ, 460, 914

van der Walt, J. 2005, MNRAS, 360, 153

Walsh, A. J., Burton, M. G., Hyland, A. R., & Robinson, G. 1998, MNRAS, 301, 640

Wang, P., Li, Z.-Y., Abel, T., & Nakamura, F. 2010, ApJ, 709, 27

Wang, Y., Wu, Y., Zhang, Q., Mao, R.-Q., & Miller, M. 2007, A&A, 461, 197

Wang, Y., Zhang, Q., Pillai, T., Wyrowski, F., & Wu, Y. 2008, ApJL, 672, L33

White, R. L., Becker, R. H., & Helfand, D. J. 2005, AJ, 130, 586

Wienen, M., Wyrowski, F., Schuller, F., Menten, K. M., Walmsley, C. M., Bronfman, L., & Motte, F. 2012, A&A, 544, A146

Wilcock, L. A., Kirk, J. M., Stamatellos, D., Ward-Thompson, D., Whitworth, A., Battersby, C., Brunt, C., Fuller, G. A., Griffin, M., Molinari, S., Martin, P., Mottram, J. C., Peretto, N., Plume, R., Smith, H. A., & Thompson, M. A. 2011, A&A, 526, A159

Wilcock, L. A., Ward-Thompson, D., Kirk, J. M., Stamatellos, D., Whitworth, A., Elia, D., Fuller, G. A., DiGiorgio, A., Griffin, M. J., Molinari, S., Martin, P., Mottram, J. C., Peretto, N., Pestalozzi, M., Schisano, E., Plume, R., Smith, H. A., & Thompson, M. A. 2012, MNRAS, 422, 1071

Wood, D. O. S., & Churchwell, E. 1989, ApJS, 69, 831

Zhang, Q., & Wang, K. 2011, ApJ, 733, 26

Zhang, Q., Wang, Y., Pillai, T., & Rathborne, J. 2009, ApJ, 696, 268

Zinnecker, H., & Yorke, H. W. 2007, ARA&A, 45, 481

.1 denouement

answers breed questions and

deeper resolution reveals deeper mysteries

so why bother?

some may invoke easy answers

but i find the mystery itself

compelling.

why settle for the super-natural

when the natural, once uncovered,

has always proved more

fantastic, awe-inspiring,

and beautiful

than anything our humble imagination

can devise?

the pursuit of truth without judgement

knowledge without profit

beauty without design answers without an end

simplicity without simplification

is science.

we will always keep searching

we will always keep asking

to ask why

is human

to keep asking

is science. [2]

[2] also young children, who, given the proper encouragement and tools can grow to be fine scientist themselves.